RICE UNIVERSITY

Photothermoelectric Effects in Gold Nanostructures

by

Xifan Wang

A Thesis Submitted
in Partial Fulfillment of the
Requirements for the Degree

Doctor of Philosophy

Approved, Thesis Committee:

Douglas Natelson, Chair
Professor of Physics & Astronomy,
Electrical & Computer Engineering, and
Materials Science & Nanoengineering

Jun Lou
Professor of Materials Science &
NanoEngineering, and Chemistry

Peter Nordlander
Wiess Chair Professor of Physics &
Astronomy, Electrical & Computer
Engineering, and Materials Science &
Nanoengineering

Houston, Texas

August, 2020

ABSTRACT

Photothermoelectric Effects in Gold Nanostructures

by

Xifan Wang

Nanostructures in noble metals(e.g Au,Ag) provide unique properties for emerging applications. One of the most important and interesting properties is the plasmonic response, where the electron gas in the metal can couple with electromagnetic radiation of wavelengths that are far larger than the nanostructure size. As a result, the local electric field can be significantly enhanced. Due to this property, the nanostructured metal device can be locally heated by an incident light, and cause electrons to travel through the device. By measuring the electronic transport and open circuit voltage, the characteristics of this photothermoelectric effects can be well studied. If one can raster-scan the laser and probe the response of the device as a function of the laser position, the variation of photothermoelectric response along the nanostructured device can be collected. In this dissertation, I mainly focused on the study of photothermoelectric effects in the gold nanowire. We observed that the photothermoelectric response varies when scanning across the gold nanowire with a focused laser beam. Such a phenomena can be possible caused by local Seebeck coefficient variation. After annealing the device with relatively low temperature (200 °C), the overall intensity of PTE response is significantly reduced. This result indicates that a major contribution to the local Seebeck coefficient is residual strain along the device. Moreover, we modified the surface of the gold nanowire with different methods and

successfully ruled out some other factors, which can potentially cause this phenomena.

Acknowledgement

First, I would like to express my deep gratitude to my advisor Prof. Douglas Natelson for the continuous support and encouragement of my Ph.D study and research, for his patience, motivation, enthusiasm, and immense knowledge. His guidance helped me in all the time of research and writing of this thesis. I could not imagine having a better advisor and mentor for my Ph.D study.

Besides my advisor, I would like to thank the rest of my thesis committee: Prof. Jun Lou, and Prof. Peter Nordlander for their encouragement, insightful comments, and questions.

Thank you to Prof. Jacob Ciszek for supplying us the high quality fluoride thiol molecules and Prof. Pulickel Ajayan for supplying us the high quality 2-D materials.

I would like to thank the following Natelson lab members for helping with research projects, especially for the optical group: Charlotte, Pavlo, Mahdiyeh,and Yunxuan. Thank you to Panpan for always being a great friend. Also I thank all my friends at Rice University, Especially, to Dr.Dobelman, who taught me a lot on statistics and modelling.

To my son Jacob and my daughter Michelle, thank you for made me stronger, better and more fulfilled than I could have ever imagined. Grace, you are the most important person in my life that I could not image live a world without you.

Finally and foremost, I would like to thank God Almighty for giving me the strength, knowledge, ability and opportunity to undertake this research study and to persevere and complete it satisfactorily. Without his blessings, this achievement would not have been possible.

Contents

Illustrations

Chapter 1

Introduction

Nanostructures in noble metals(e.g., Au, Ag) provide unique properties for emerging applications. One of the most important and interesting properties is the plasmonic response, where the electron gas in the metal can couple with electromagnetic radiation of wavelengths that are far larger than the nanostructure size. As a result, the local electric field can be significantly enhanced. Due to this property, the nanostructured metal device can be locally heated by an incident light, and causes a net flux of electrons to travel through the device. By measuring the electronic transport and open circuit voltage, the characteristics of this phenomenon can be well studied. If one can raster-scan the laser and probe the response of the device as a function of laser position, the variation of photothermoelectric response along the nanostructured device can be collected.

A key material property that defines thermoelectric response is the Seebeck coefficient. In principle, the Seebeck coefficient of different metals and the temperature gradient along them would causes the electric voltage to build up along from the temperature gradient. Recent publications suggest through nanostructuring the thermoelectric properties of thin metal film devices can be manipulated.[1, 2, 3] Observation that the substantially local Seebeck coefficient variation in polycrystalline gold nanowires with uniform thickness and width was surprising, where the Seebeck coefficient is generally considered as constant within a well defined a material.[3] Another study of the photothermoelectric response of single crystalline and bi-crystal

gold wires, where an individual grain boundary separates two single crystals gold wire, indicate that grain structure itself does not have a significant contribution to the local Seebeck coefficient. Instead, the photovoltages of these devices are well correlated with local variations in strain as detected by electron back scatter measurements and with variations in platinum impurity concentration as seed in nanoscale ion mass spectroscopy.[4] Therefore, the scanning photovoltage measurements are demonstrated to have sensitivity to intrinsic variations in nanoscale devices that are otherwise difficult to detect using traditional electronic transport and imaging techniques. Furthermore, annealing the multi-crystal gold nanowires at relatively low temperatures reveals that strain can be the dominant influence on the the local Seebeck coefficient. After introducing key physical concepts, the bulk of this thesis focuses on a variety of surface modification effects to examine these factors that can contribute to the PTE response.

1.1 Thesis structure

Chapter 1 will discuss the introductory background information needed to understand the experimental results include thermoelectric effect, Seebeck coefficient,single metal thermocouple, plasmons, and raman spectroscopy . Chapter 2 will provide details about the nanoscale device that is discussed in this work: the gold "bowtie" consisting of a plasmonically resonant nanowire constriction between two fan out electrodes. Previous research work relates to this work on this gold bowtie structure from Natelson's group are briefly summarized. Chapter 3 will introduce the experimental methods, and the experimental instruments used throughout this work. The results discussed in this work can be broken down into two parts: Chapter 4,5 and Chapter 6. Chapter 4 and 5 will mainly focused on the photothermoelectric effects in the gold

bowtie structure, includes photothermoelectric detection of gold oxide nonthermal decomposition, and the dominant mechanism causes Seebeck coefficient changing in the gold bowtie structure. Chapter 6 will, discuss a sub band gap surface-enhanced Raman spectroscopy on the monolayer MoS_2. Finally, Appendix will provide the code for data analysis, measurement, and motor control.

1.2 Thermoelectric effect

By definition, the thermoelectric effect converts temperature differences to electric voltage and vice versa. In a metal strip with a temperature gradient along the strip, the free electrons will diffuse from the hot side to the cold side until a steady state is reached. If a constant temperature gradient (∇T) existing along this metal strip, the electrons will still diffuse from the hot side to the cold side until a voltage difference build up between both ends to counteract the thermal diffusion of electrons, which results in no net flow of charge. This so-called open circuit voltage (OCV) is proportional to the temperature difference between the ends. The proportionality constant is called the Seebeck coefficient (S), and is a material dependent property .Thermoelectric effects actually comprise of three different, independently found effects: the Seebeck effect, Peltier effect, and Thomson effect.[5]

1.2.1 Seebeck effect

First of all, we start with the two major concepts: the Seebeck coefficient and thermocouples. The Seebeck coefficient is considered as a material intrinsic property which describes the propensity of the material to build up potential to counteract a temperature gradient. This means the larger S is, the larger the potential build up with the same temperature gradient. A thermocouple is an electrical device consisting of two

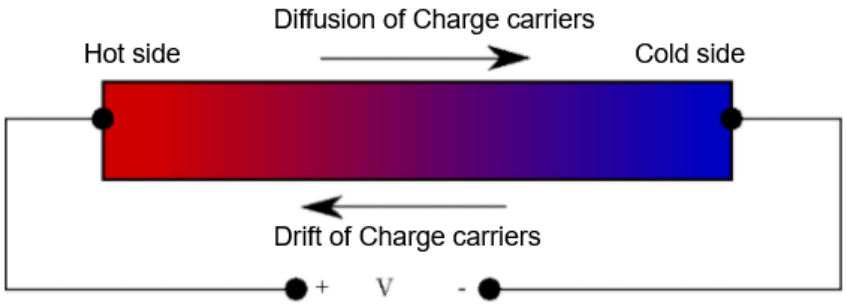

Figure 1.1 : Illustration of the thermoelectric effect, when a temperature gradient applied to a conductor, the electrons will thermally diffuse from the hot side to the cold side. To counteract the thermal diffusion, a voltage will be built up. So that the drift balances the diffusion, leading to no net current.

materials with different Seebeck coefficients in contact with each other. Rather than heating one end vs. the other, heating the junction of the two materials and keeping the two ends at same temperature will result a difference in voltage (ΔV) that is proportional to the temperature difference(ΔT) but the multiplicative factor is the difference of the Seebeck coefficient S between the materials as shown in Fig.1.2. The generalized form of the Seebeck effect is defined as:

$$J = \sigma(-\nabla V + E) = \sigma(-\nabla V - S\nabla T)$$

this formula links the local current density (J) to the local electrical conductivity(σ), the local voltage gradient(∇V) and the local electric field (E) which is equal to $-S\nabla T$. The equation for steady state Seebeck effect is:

$$\nabla V = -S\nabla T$$

Equation 1.2 is given when the system has reached the steady state, that is the net local current density (J) is 0.

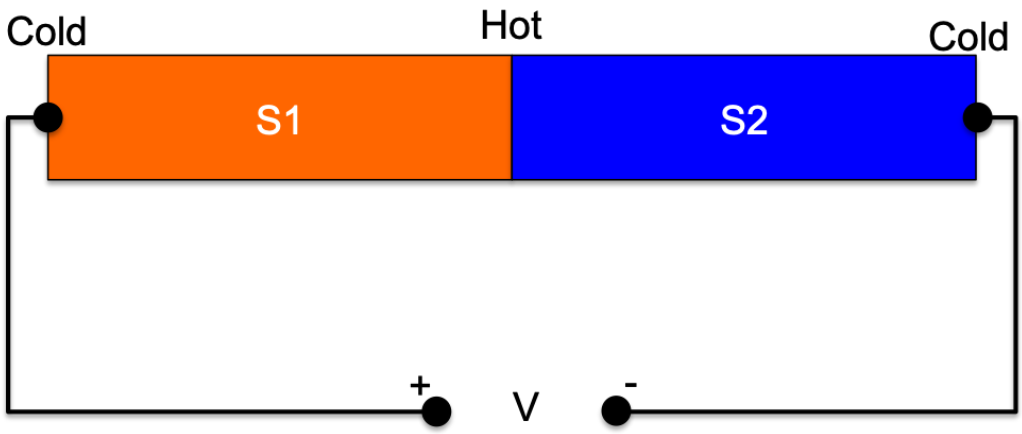

Figure 1.2 : Schematic of a typical thermocouple: two strip of different materials with identical Seebeck coefficients (S1 and S2) in contact with each other. The junction of the two different materials is heated to temperature T_h with two ends kept at constant, cold temperature, T_c. A voltage proportional to the applied temperature gradient and the difference in Seebeck coefficients can be measured between two ends.

1.2.2 Peltier effect

Basically, the Seebeck and Peltier effects are different manifestations of the same physical process.In the Peltier effect, instead of a temperature gradient resulting in a OCV, applying an electrical current across a thermocouple, heat is evolved at one junction and absorbed at the other junction. Depending on the direction of the current flow, the junction can either heat up or cool down. The Peltier heat generated at the junction per unit time is:

$$\dot{Q} = (\Pi_A - \Pi_B)I$$

where $\dot{Q}$ is the he heat generated at the junction per unit time, Π_A and Π_B are the Peltier coefficients of conductors A and B, and I is the current.[5] The Peltier

coefficients indicates how much heat is carried per unit charge. As seen in Fig 1.3, an schematic of Peltier effect, the hot junction depicted can be isolated outside of an insulated area, and the other side can be used for cooling. The Peltier effect is used a lot in electronics, particularly to cool computer CPUs.[6, 7] The power of heat generation depends on the product of the total resistance and the square of applied current.

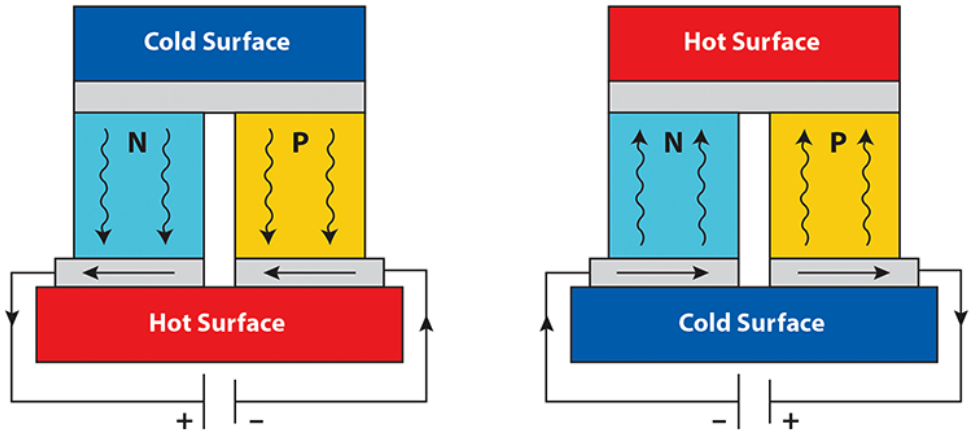

Figure 1.3 : Schematic of Peltier effect, a temperature difference created by applying a voltage between two electrodes connected to a sample of semiconductor. As a result, the heat can be transferred from one side to another. From ref.[6]

1.2.3 Thomson effect

From above sections, the Peltier effect and Seebeck effect are highly related, the material Π is determined by the S and the absolute temperature. When the S of material is temperature dependent, $S(T)$, the temperature gradient cross the material will cause a spatial ∇S variation. If a current applied to the material, it will result in a continuous Peltier effect is so called Thomson effect. which the heat production rate per unit volume can be described as:[5]

$$\dot{q} = -KJ\nabla T$$

1.3 Seebeck coefficient and thermocouple

In this section, the Seebeck effect and it's role in the real world application will be discuss in detail, which is highly relevant to the research done in this thesis.

1.3.1 Seebeck coeffient

The Seebeck coefficient, is material property that describes the propensity of the material to build up charge to counteract a temperature gradient with SI units V/K. When the system reaches a steady state(Fig. 1.1) ,the S is defined:

$$S = -\frac{\Delta V}{\Delta T}$$

From previous section, the Seebeck effect results in a open circuit voltage due to the free electrons tending to diffuse from the hot side to the cold side. S, therefore depend on the material conductive properties, which also depend on the temperature. To measure S, a two material system is typically used(Fig.1.2). In a standard thermocouple structure, two different type of metal will join at a reference point, so probe ends will be the same temperature and the relative S between the two different metals will be read. By using a standard metal with known S, the Seebeck coefficient for the other metal can be measured.[8]

The Seebeck coefficient consists of two components: the charge carrier piece and the phonon drag.[9, 10] When the system is at high temperature, the electric component dominates and given the deviation of the electronic system from equilibrium

due to an applied ΔT. The heat and charge carried by the phonons due to an applied ΔT is described by the phonon drag component as well as the electron-phonon interaction.It can be negligible at high temperatures, but it plays a critical role at low temperatures lower than the Debye temperature of the system. Since most of the research in this thesis is done at room temperature, which is a good approximation of "high temperature". Therefore, we considered only the electronic component of S.

The density of states of the charge carriers near the Fermi surface determine the sign and the value of S for a specific material. The sign of the charge carriers plays a role in determining the value of S, where materials dominated with holes typically have positive S whereas materials dominated with electrons have negative S. For only consider the electronic component of S, the the Seebeck coefficient for a metal can be defined via Mott formula:[11]

$$S = \frac{\pi^2 k_B^2 T}{-3e} \frac{\sigma'}{\sigma}$$

Where T is temperature, k_B is Boltzmann constant, e is electron charge, σ' is the derivative of the energy dependent electrical conductivity, and σ is electrical conductivity at Fermi energy. The electrical conductivity in a free electron model is defined as:[12]

$$\sigma = \frac{e^2 \lambda A}{6\pi^2 \hbar}$$

where A is the Fermi surface area and λ is the electron mean free path, and $\hbar$ is the Plank constant.

From Fig.1.4, metals have a relatively low S value compared with semiconductors. Due to their high carrier densities, the derivative of the energy dependent electrical

Metals	Seebeck Coefficient
	μV/K
Antimony	47
Nichrome	25
Molybdenum	10
Cadmium	7.5
Tungsten	7.5
Gold	6.5
Silver	6.5
Copper	6.5
Rhodium	6.0
Tantalum	4.5
Lead	4.0
Aluminum	3.5
Carbon	3.0
Mercury	0.6
Platinum	0
Sodium	-2.0
Potassium	-9.0
Nickel	-15
Constantan	-35
Bismuth	-72

Semiconductors	Seebeck Coefficient
	μV/K
Se	900
Te	500
Si	440
Ge	300
n-type Bi_2Te_3	-230
p-type $Bi_{2-x}Sb_xTe_3$	300
p-type Sb_2Te_3	185
PbTe	-180
$Pb_{03}Ge_{39}Se_{58}$	1670
$Pb_{06}Ge_{36}Se_{58}$	1410
$Pb_{09}Ge_{33}Se_{58}$	-1360
$Pb_{13}Ge_{29}Se_{58}$	-1710
$Pb_{15}Ge_{37}Se_{58}$	-1990
$SnSb_4Te_7$	25
$SnBi_4Te_7$	120
$SnBi_3Sb_1Te_7$	151
$SnBi_{2.5}Sb_{1.5}Te_7$	110
$SnBi_2Sb_2Te_7$	90
$PbBi_4Te_7$	-53

Figure 1.4 : Seebeck coefficient list of different material at room temperature. In most cases, metals have a relatively small Seebeck coefficient and semiconductors have a relatively large Seebeck Coefficient at room temperature. From ref.[13]

conductivity, σ', is weaker in metals than in semiconductors, leading to low S values, which make metals less popular candidates for most thermoelectric effect applications. While, Semiconductors are more common in thermoelectric effect devices due to higher S values.

As shown in the Mott formula, S is proprietorial to the energy dependent electrical conductivity which depends on the temperature. Fig.1.5 shows common metal's

Seebeck coefficient temperature dependence. At high temperatures, where the dominant scattering mechanism is electron-phonon scattering.[14] However, metals can have complex electronic structures, scattering mechanisms, and magnetic properties which can lead to a nonlinear relationship between the temperature and S, when the temperture is below the Debye temperature.[3, 15] the temperature relationship of S deviates significantly because the scattering mechanisms change as phonon modes begin to freeze out.[16] Therefore, we can no longer only consider the electronic portion of the Seebeck coefficient and instead must consider the contributions of phonons, and specifically phonon drag, to thermopower.

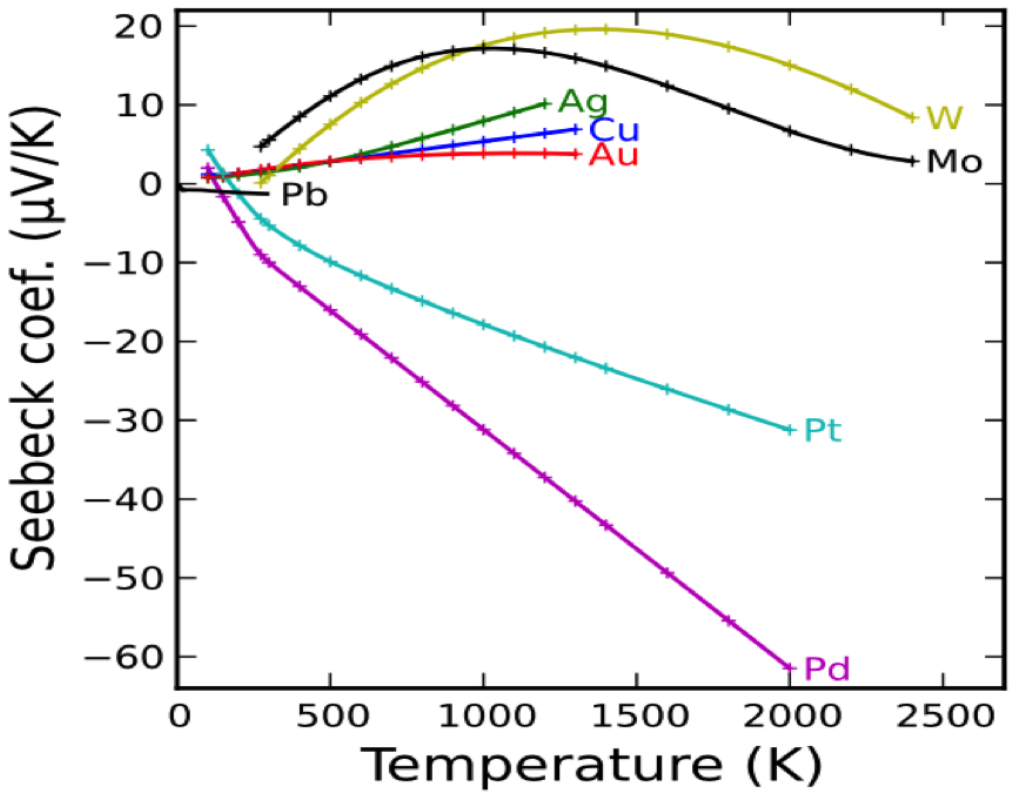

Figure 1.5 : Temperature dependence of Seebeck coefficient for some metals, some metals(e.g Au,Ag,Cu) have a relatively invariant Seebeck coefficient and some metals(e.g Pt,Pd,W) have a relatively large varied Seebeck coefficient with temperature. From ref.[17]

When a temperature gradient is built up on to a material, the phonons tend to travel away from the hot end toward the cold end of the material rather than proposities isotropically. The directionality of the charge carriers scattering of the phonons is not random, instead the scattering events push the carriers toward the cold end, result as an increase in S (Fig.1.6.). To reach the equilibrium, an OCV that must build up to counteract not only the thermal diffusion of the charge carriers but also the effect of the phonon drag. At very low temperatures, there are not enough phonon modes to contribute to the phonon drag effect, leads to a decrease in S.[18] While more phonon modes turn on as the temperature rises, the phonon drag effect will cause an increase in S,[19] until phonon-phonon scattering processes tend to reduce the effect, resulting in a phonon drag peak.

Now as we shrink the size of the material down to a thin film, the surface scattering also decreases electric conductivity, and therefore the electronic mean free path, lowering the electronic contribution to S, as well as the phonon drag component important at low temperatures. Therefore, changing the thickness of thin metal films can then tune the electronic component of the Seebeck coefficient.

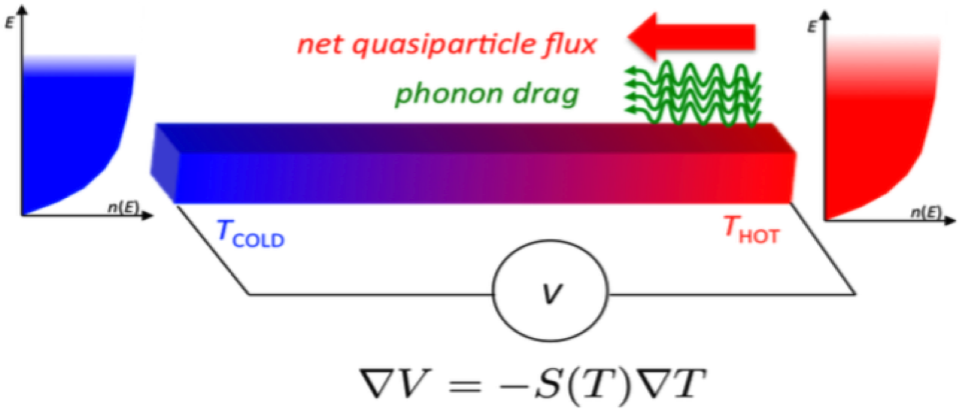

Figure 1.6 : Phonon drag and charge carrier contribute to the Seebeck coefficient.[20]

1.3.2 Thermocouple

In this thesis, the study is mainly focused on nanoscale. In the nanoscale, the the Seebeck coefficient can be tuned by geometry that allow for the creation of single metal thermocouples.[21, 22] With such a small scale, spatial resolution can be much higher than in buck materials.(Fig.1.7.)

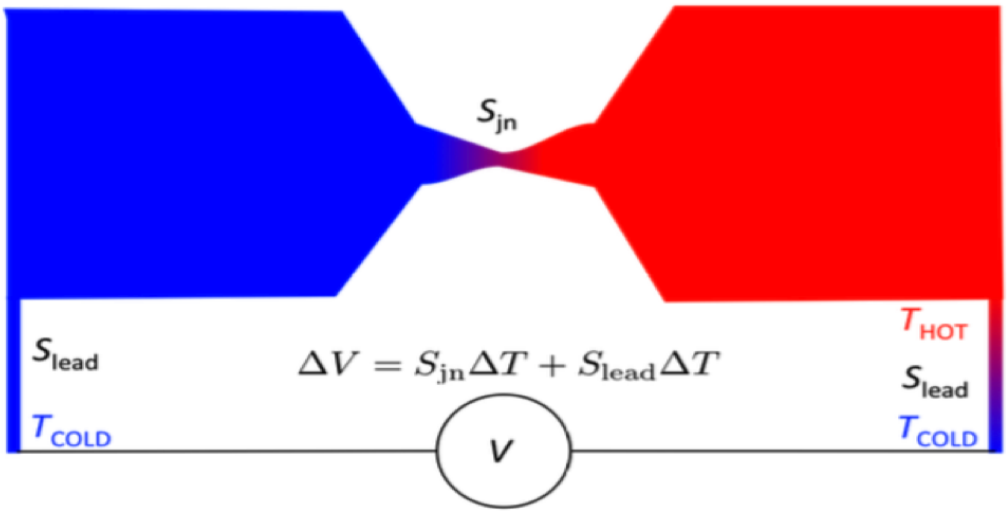

Figure 1.7 : Seebeck coefficient variation caused by geometry change at nanoscale. [20]

1.3.3 Single metal thermocouple and nanostructure

From above discussion, the Seebeck coefficient can be tuned by changing the electron mean free path. In such a way, we may down size the device to nanoscale by changing the width or thickness. If there is a abrupt change in geometry in a nanoscale device, a single metal thermocouple can be created from single metal.[21, 22] As an example, Fig.1.8, the left panel shows a thermocoulpe made from single metal. A resistive heater is running current through Joule heating with power proportional to the square

of the current and heated up the near sited device.

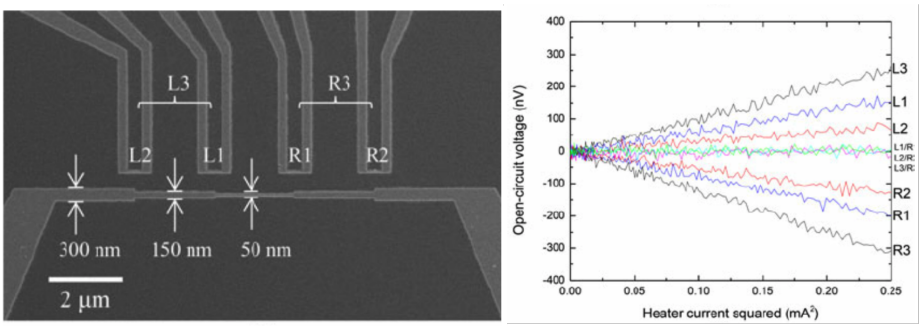

Figure 1.8 : Single metal thermocouple. From ref.[21]

At the different point on the device and the open circuit voltage measurement is on the right.) The result indicate a successful single metal thermocouple can be made in such a way. If only one side is heated, the magnitude of the open circuit voltage increases linearly with the heater power(Fig.1.8.right). Heating the opposite junction results in the opposite sign of thermovoltage; the sign of the thermovoltage is determined by the difference in Seebeck coeffcients, and the order is reversed on the opposite side. Evenly heating the junctions at the same time causes these voltages to cancel out. In our study, we used a moveable focused laser as a heat source instead of using a fixed resistive heater. In this a way, we can study the local variation of Seebeck coefficient.

1.4 Photothermoelectric effect

Compared with the ordinary thermoelectric effect, the Photothermoelectric effect (PTE) uses a laser as the heating source to probe the temperature difference driven photovoltages but other concepts are the same. The major benefit of using a laser as the heating source is that the photovoltage can be measured as a function of heating

position, which can detect the local Seebeck response. when a temperature gradient ∇T is caused by this laser heating at somewhere in the middle of the device with both ends kept at a constant temperature, the open circuit voltage between the ends depends on the local seebeck effect from the heated area. The equation is showns as below:

$$\Delta V = \int_0^l S(x, T(x)) \frac{dT(x)dx}{dx}$$

where T is the local temperature and $S(x; T(x))$ is the local Seebeck coefficient that is a function of position and the temperature distribution. The photothermoelectric effect has been used to characterize nanostructures under focused illumination.[23] Because of the nanostructures can also be geometrically structured to be plasmonically resonant at certain wavelengths, the photothermoelectric effect is also used as a mechanism for photodetection,and energy conversion.[24, 25, 26]

1.5 Plasmons and surface enhanced Raman spectroscopy

A major part of this thesis is to study about how light interacts with matter, and in particular how light can interact with the free electron gas in gold, which results in collective oscillation. These collective oscillation are called plasmons. In physics, a plasmon is a quantum of plasma oscillation. Since plasmon arises from the quantization of plasma oscillations, which can be considered as a quasiparticle,[27] just like phonon is a quantization of mechanical vibrations.[28] Thus, plasmons are collective (with a discrete number) oscillations of the free electron gas density. Hence, plasmons can couple with a photon to create another quasiparticle ,at optical frequencies, called a plasmon polariton.[29]

In this section, we will discuss the plasmon excitation based on the dielectrical

properties of gold (and other metals, in particular, noble metals) in the first. we will introduce Raman spectroscopy and the role plasmons play in surface enhanced Raman spectroscopy in the later.

1.5.1 Dielectric properties of metals

A metal conductor such as gold may be modeled as a gas of conducting electrons, moving freely around and interacting with the static lattice of positively charged ions.[30] Macroscopically, in equilibrium there is a net zero electric field, the positive ions in the lattice is neutralized by the surrounding electron gas, which to balance the charge in the system. When a constant electric field is applied to a slab of the material, the electrons will be displaced from the positive ionic lattice and rearrange themselves to counteract the field, as seen in the Fig.1.9.[31]

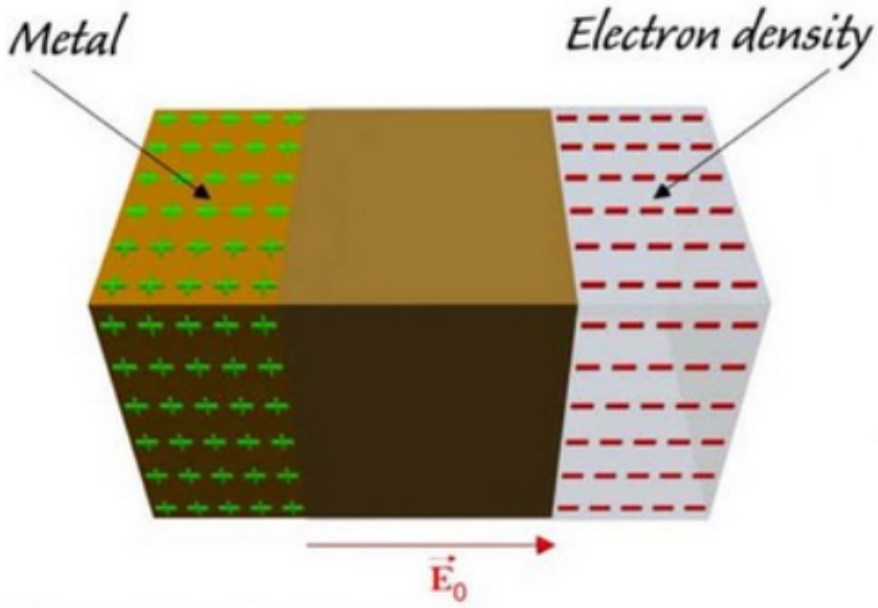

Figure 1.9 : Schematics of bulk plasmons: the electron density in metal oscillates under an external electric field E_0. From ref.[31]

When the electric field is instantly turned off, an electric field , which is caused by the separation of the electron gas and the positively charged lattice will pull the electrons back toward the lattice. Typical carrier densities for good metals are around 10^{22} to 10^{23} carriers per cm^{-1}.[20] As the electrons move back to the lattice, they gain momentum from the field and will overshoot their original position. This, in turn, results in an electric field in the opposite direction which causes the electrons to collectively oscillate akin to simple harmonic motion like a spring which can be described by the followed equation:

$$m_e \frac{\mathrm{d}^2 x}{\mathrm{d}t^2} = -eE = -kx$$

where m_e is the effective mass, spring constant $k = m_e {\omega_p}^2$ and electron charge e. By substituting for k and rearranging, the ω_p of the collective oscillation of the free electron gas is defined by:[32]

$$\omega_p = \sqrt{\frac{e^2 n_e}{\epsilon_o m_e}}$$

where ϵ_o is the the permittivity of free space, ω_p is the plasma frequency and depends only up on n_e, since the other parameters are fixed. The n_e for gold is about 5.9×10^{22} cm^{-3}.[32] The plasma frequency sets the timescale of these bulk plasmons with energy($\hbar\omega_p$).[33] This is classical picture is so called Drude model of electrical conduction.

Dielectric function of a homogeneous medium $\epsilon_x(\omega_p) = \epsilon_1(\omega_p) + \mathrm{i}\epsilon_2(\omega_p)$ relates the electric field E(x,ω_p) at position x.[34] with angular frequency ω to the displacement field $\mathbf{D}(\mathrm{x},\omega) = \epsilon_r(\omega)\epsilon_0\mathbf{E}(\mathrm{x},\omega)$. When incident light interacts with metal, if the frequency of the light is lower than the plasma frequency of the metal, the dielectric function is negative.That is due the free electron gas in the metal, since the plasma

frequency of those electron gas is higher, they can catch up with the external oscillations to neutralize the field, resulting in total reflection of the light. If the external light frequency is higher than the plasma frequency, then the free electrons can not be able to cancel the oscillating electric field. As the result, the dielectric function becomes positive and the metal begins to absorb the incident light. For most of the metals, the plasma frequency is in the UV range.[35] As an example, gold has the plasma frequency at 2164 THz which corresponds to 138.5 nm wavelength.[36] However, the Drude model does not capture everything involving the dielectric function of gold, particularly in the visible range. Gold presents as yellow color under the natural light, indicating that the blue frequencies are not reflected as well as the other wavelengths in the visible range. This result is due to the limitation of Drude model, which only considers the free electron gas but not those bound electrons in the metal. Those bound electrons play a large role in optical properties of gold and inter-band transitions must be considered, which means the electrons can transition between bound states and conduction band when high energy photons interact with gold. For gold, the 5d-band electrons to the conduction band is 2.4eV, which is within the blue range of visible light.[37] Due the chemically stability under ambient environment, gold has became a popular selection for plasmonics.

1.5.2 Surface plasmons and Raman spectroscopy

As mentioned earlier, the sign of the real part of the dielectric function flips when across a metal-dielectric interface. Surface plasmons are the surface charge density oscillations spatially confined to this metal-dielectric interface.[38] The energy of surface plasmons is lower than bulk plasmons, which quantize the longitudinal electron oscillations around positive ion cores within the electron gas and generate

electromagnetic fields around the metal.[39] Therefore the charge motion together with associated electromagnetic field is called surface plasmon polariton, as shown in Fig.1.10.[40]

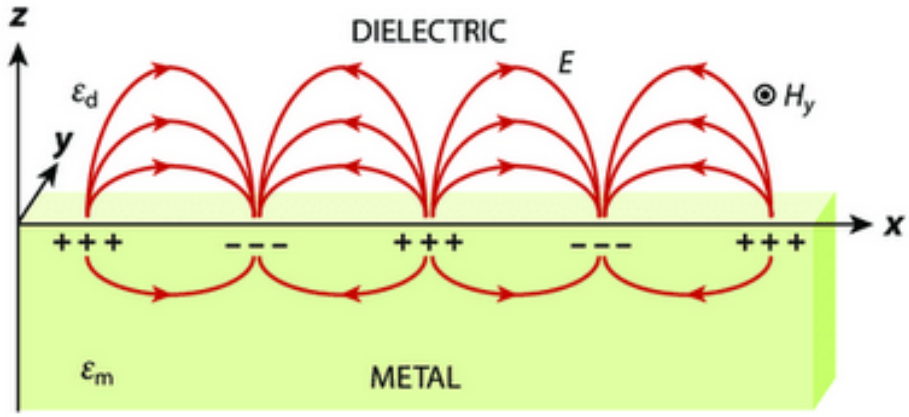

Figure 1.10 : Schematics of a surface plasmon polariton ("propagating plasmon") propagating along a planar metal-dielectric interface due to the periodic oscillation of the charge density. From ref.[40]

When we scale down further from bulk to nanoscale, plasmonic properties become even more interesting as the effects of bulk plasmons and surface plasmons become less distinct. Given an example, a metal nanoparticle which is much smaller than the wavelength of incident light, the incident oscillating electric field is confined to the nanoparticle and will create resonant local surface plasmons as "standing wave" oscillations.[38] For nanoparticles, the plasma frequency is a portion of the bulk plasmons:

$$\omega_p = \sqrt{\frac{1e^2 n_e}{3\epsilon_o m_e}}$$

Most gold nanoparticles used for plasmonics typically have the diameter around 10 to 100nm.[41, 42, 43, 44, 45] The plasmon energy is affected by the size, geometry of the nanoparticles and the surrounding dielectric environment.[46] By changing the

dielectric environment, the extinction cross section is also changed which leads to a shift of the plasmon energy. The size and the geometry also affect the plasmon energy.

The local field enhanced by surface plasmons can be further enhanced via putting two nanoparticles togther with those pairs known as dimers.[47] Moreover, The local enhancements can be tuned via the polarization of the incident light.[48] When the laser is at the optimal polarization, the charge distribution from plasmonic oscillation can great enhance the local field.[49] The field enhancements from the nanoparticles increases as the nanoparticles get closer together with a increasing factor by the distance of the particles (d^{-8}).[32, 50], However, when the distance is getting in to the tunnelling range, this effect is suppressed. Hence, the best distance for this effect is about 2-5 nm.[32, 51] This enhanced local field can significantly enhance the Raman signal allowing us to do single molecule Raman spectroscopy. According the literature, an example of the relationship between enhancement factor and the size of the nanoparticles, the distance of two nanoparticles and the incident laser wavelength has been shown in Fig.1.11.[50]

Raman spectroscopy

Raman spectroscopy is a spectroscopic technique used to detect vibrational, rotational, and other states in a molecular system, capable of probing the chemical composition of materials using the frequency of scattered light. When the light interacts with the molecule, the oscillating electromagnetic field of a photon induces a polarisation of the molecular electron cloud which leaves the molecule in a higher energy state with the energy transferred from the photon to the molecule. This can be considered as the formation of a very short-lived complex between the photon and molecule which is commonly called the virtual state of the molecule.[52] The virtual state is

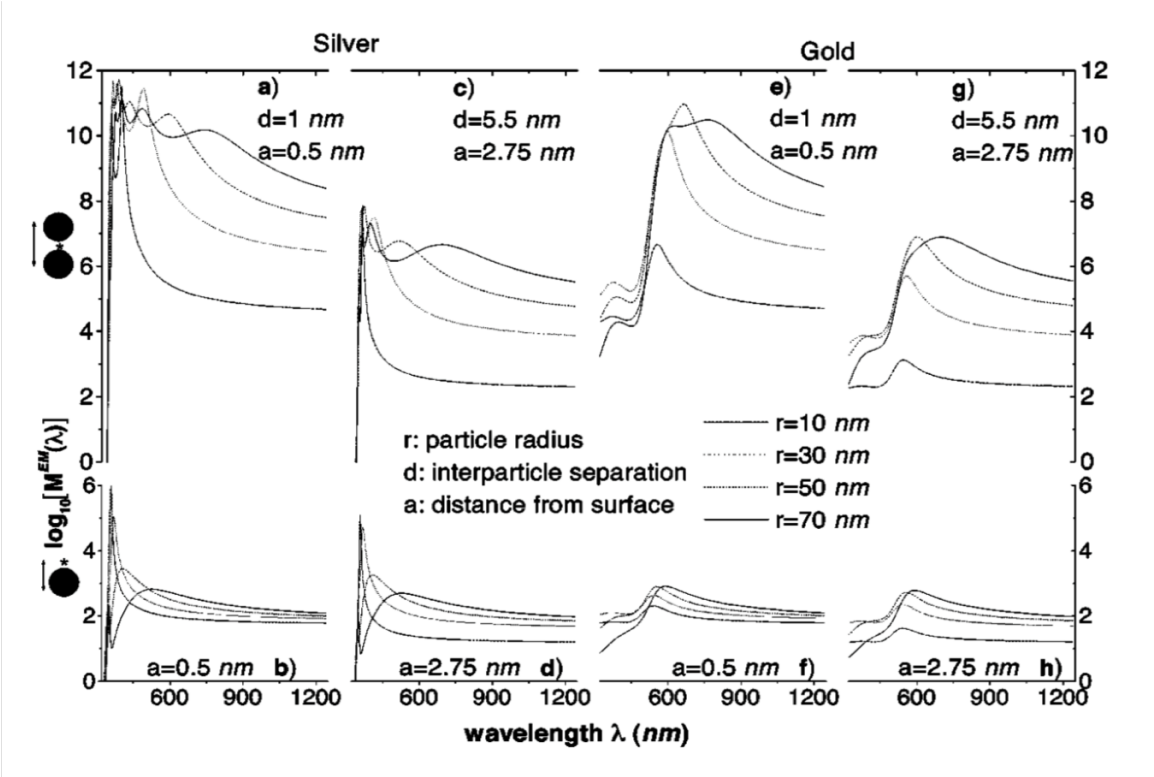

Figure 1.11 : The enhancement factor of silver and gold nanoparticles as a function of size, the distance of two disk(top) and the incident laser wavelength.[50]

not stable and the photon is re-emitted almost immediately, as scattered light. During this process, the most scattering events occurs as Rayleigh Scattering or elastic scattering, in which the photon energy is unchanged after the photon-molecule interaction, and therefore the wavelength of the scattered photon is equal to that of the incident photon.

In a much rarer event (roughly 1 in 10 million photons),[54] Raman scattering occurs, which is an inelastic scattering process with a transfer of energy between the molecule and scattered photon. These are two types of inelastic scattering: Stokes Raman scattering and Anti-Stokes Raman scattering. If the molecule gains energy from the photon during the scattering (molecule is excited to a higher vibrational

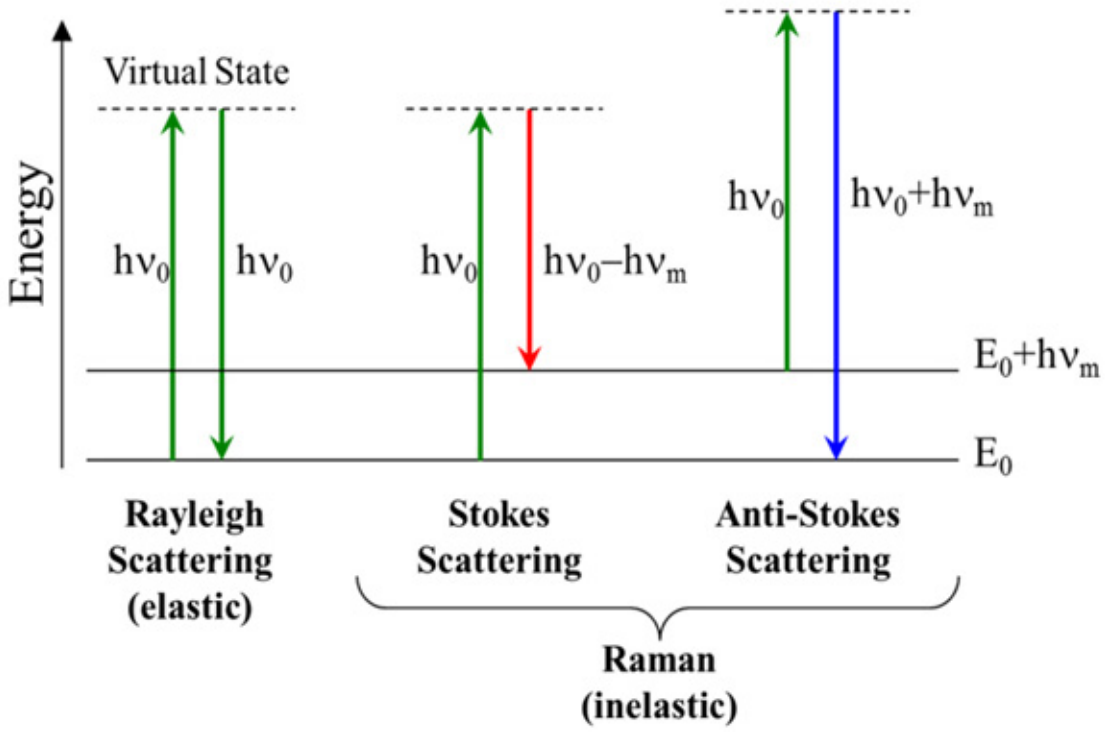

Figure 1.12 : Schematic of Rayleigh and Raman scattering. A molecule absorbs an incident photon of energy hv_0, gets excited to a virtual state, before re-emitting the photon which is either elastically or inelastically scattered. Left: Rayleigh scattering, the elastic scattering event where both the molecule and photon energies remain unchanged. Middle: Stokes scattering, where the photon loses energy to the molecule, exciting it to an excited vibrational state. Right: Anti-Stokes scattering, where the photon gains energy from the molecule, relaxing it to a ground state.[53]

level) then the scattered photon loses energy and its wavelength increases which is called Stokes Raman scattering. Conversely, if the molecule loses energy by relaxing to a lower vibrational level and the scattered photon gains the corresponding energy and its wavelength decreases. This is called Anti-Stokes Raman scattering. Quantum mechanically Stokes and Anti-Stokes are equally likely processes. However, with an ensemble of molecules, the majority of molecules will be in the ground vibrational level (Boltzmann distribution) and Stokes scattering is the statistically more probable

process. As a result, the Stokes Raman scattering is always more intense than the anti-Stokes and for this reason, it is nearly always the Stokes Raman scattering that is measured in Raman spectroscopy since the overall signal is much higher.[54]

The Raman spectroscopy looks at energy shifts, it is often easier to consider the energy in terms of wavenumber (cm^{-1}), defined as $cm^{-1} = \frac{1}{\lambda}$ .The wavelength of the Raman scattered light will depend on the wavelength of the excitation light. This makes the Raman scatter wavelength an impractical number for comparison between spectra measured using different lasers. The Raman scatter position is therefore converted to a Raman shift away from excitation wavelength:[55]

$$\Delta(cm^{-1}) = (\frac{1}{\lambda_{incident}} - \frac{1}{\lambda_{scattered}}) \times \frac{10^7 nm}{cm}$$

For reference, 1 eV = 8086 cm^{-1}.[56] Since the inelastic light scattering events are

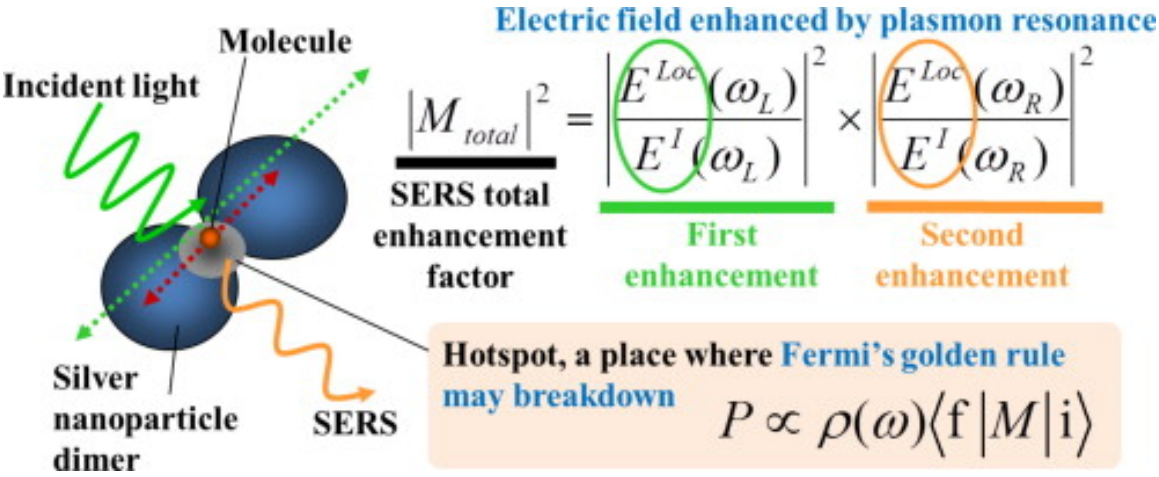

Figure 1.13 : Schematic of SERS process and the SERS total enhancement factor. From ref.[57]

very rare, it is very challenging to detect the Raman signal from trace number of molecules without any enhancement.

The electric field enhancement from plasmonic nanostructures can significantly increase the Raman scattering intensity in a process called surface-enhanced Raman spectroscopy (SERS). There are two different mechanisms that are attributed to these enhancements: electromagnetic and the chemical theory.The general concept of SERS from electromagnetic enhancement from plasmons is depicted in Fig1.13,[57] and can be described as follows: a molecule is placed on a roughened metal surface with a incident laser given an electric field $E = E_o$ with frequency ω and the intensity I_o. as discussed in previous sections, the local field is enhanced via the local plasmon mode in the metal surface by a factor of $g(\omega)$. After the interaction, the molecule scatters the light, re-emitting a photon at frequency $\omega^{'}$ The local field is then enhanced again by the local plasmons with $g(\omega^{'})$ therefore the total enhanced local field is then $E = g(\omega^{'})g(\omega)E_o$. .[58]For low shift wavenumbers, g(ω) $\approx$ g($\omega^{'}$). Therefore, the total intensity of SERS signal is $I \propto \mathrm{g}^4\ I_o$, which scales to the fourth power with g but also linearly with the intensity of incident laserI_o. From literature, a total enhancement factor could be up to 10^{11}[58, 50] which allow Raman spectroscopy for single molecule detection.

Chapter 2

Previous Work

Science is a story of development, and the current research work is based on the knowledge from previous research projects. In this chapter, the original motivation of the gold "bowtie" structure and previous results of lithographically defined plasmonically active single molecule junctions with single molecule SERS enhancement with the ability for simultaneous electronic transport measurements will be discussed, along with some of the challenges of achieving true low temperature measurements due to local temperature rises from plasmonically active modes in the wire.

2.1 Gold bowtie devices with a resonant transverse plasmon mode

A large amount of work discussed in this thesis, and in numerous publications from the Natelson lab has been conducted using gold "bowtie" devices;[59, 60, 61, 62, 63, 64, 65, 66, 3, 23] This devices consisting of a thin film, polycrystalline gold nanowire between two fanout electrodes. The fan-out electrodes will be extended and connected to large gold pads, which allow for electronic transport measurements. The detail fabrication process for this device will present in Chapter 3. The geometry of nanowire is optimized to have a resonant transverse plasmon mode (perpendicular to the length of the wire) under 785 nm free space CW laser illumination.[67] Fig.2.1 is a SEM image of typical gold "bowtie" structure. The temperature of the nanowire raise

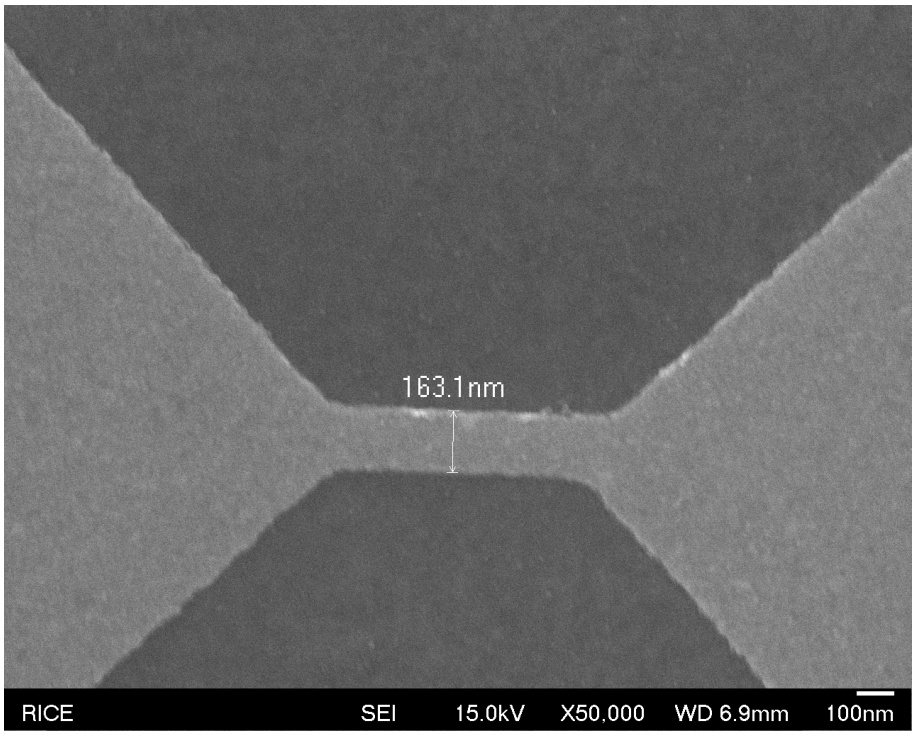

Figure 2.1 : Gold Nano Bowtie with 14nm gold thinkness and 1nm titanium as adhesion layer

when a 785nm laser illuminated on it due to both direct absorption and the plasmonic resonance. This phenomenal can be detected via electronic transport measurements. Compared with the total area of the device, the nanowire section is much narrower, and therefore the overall conductance is constrained by the nanowire. Hence, the variation of conductance is attributed to the change associated with nanowire itself. The specific geometry design of the nanowire gives a polarization dependence of the incident laser (785nm) on the differential conductance of gold nanowire due to the local transverse plasmon mode as shown in Fig.2.2.[68]

Where the maximum and the minimum of the differential conductance occurs at when the laser is at the transverse polarization and longitudinal polarization respectively. Since gold has a positive conductance coefficient($\frac{dR}{dT}$), this gives a trivial

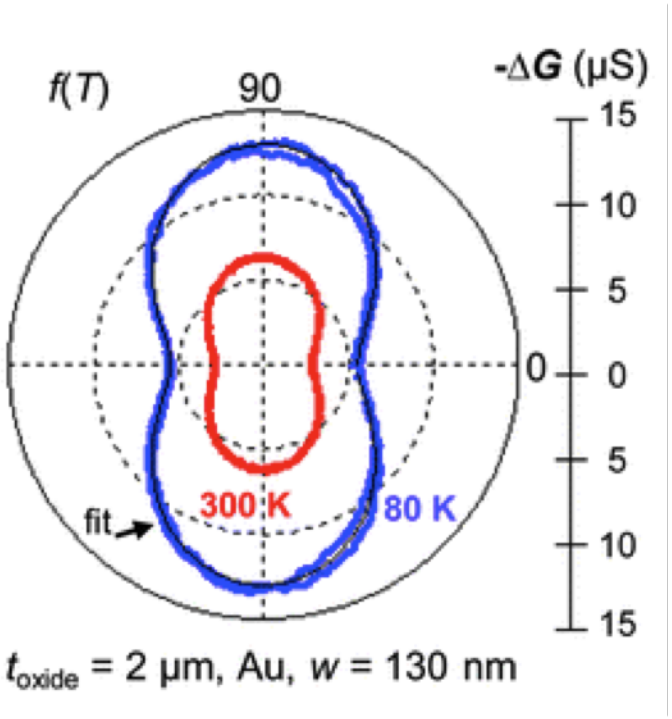

Figure 2.2 : Polarization dependence of the differential conductance when the laser is incident on the gold nanowire. Blue line displays the conductance measured at 80K, and redline displays the conductance measured at 300K.[68]

method to measure the temperature variation of the gold nanowire under the illumination of incident laser. The resistivity of the gold increases as the temperature increases under a linear relation. Therefore, we can simply estimate temperature by using the differential conductance, Δ G $= \frac{dI}{dV}$ by:[68]

$$\Delta T = \frac{-R^2 \Delta G}{\frac{dR}{dT}}$$

where $\frac{dR}{dT}$ is the slope of the substrate temperature dependence of the total device resistance and R is the total device resistance at the measurement substrate temperature. As been known[3], the $\frac{dR}{dT}$ is linear above 30K.

2.2 Large local heating in gold nanowires

A study[3] of high local heating in gold nanowires indicated a big temperature rise under laser illumination when the substrate temperature is low (e.g. 10K). The measurements were taken on various substrates by using a lock-in amplifier, the differential conductance of the device under chopped optical illumination was measured. As we discussed previously, the change if the conductance is dominated by the gold nanowire area. This paper studied the polarization and incident laser intensity dependence of the inferred temperature rise of the bowtie constriction on various substrates and at various substrate temperature.

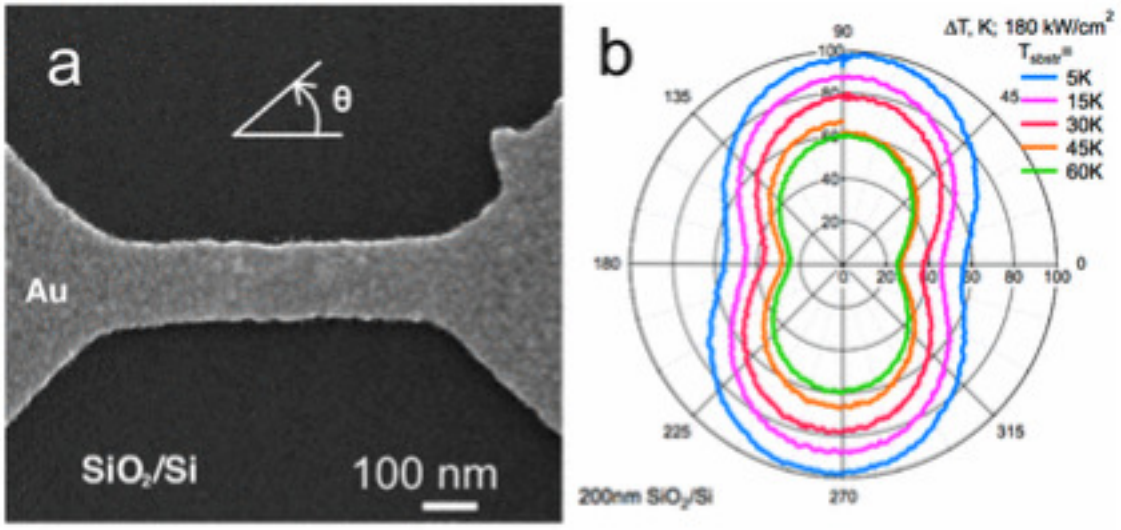

Figure 2.3 : SEM image of a typical gold bowtie device. Right: polarization dependence of the temperature rise of the constriction under direct illumination at various substrate temperatures. The maximum heating occurs when the laser is in the transverse polarization, exciting the local surface plasmon resonance in the nanowire. The heating of the wire increases as the substrate temperature decreases. From ref.[3]

As shown in Fig2.3[3], the temperature rise has a strong polarization dependence, with the transverse polarization having the largest response. This is indicative of the

excitation of the transverse local surface plasmon resonance. With the substrate temperature decrease, the temperature rise increases. At a low temperature of 5K, the temperature rise of device with 200nm Silicon oxide is 100K. To solve this problem, one approach is to reduce this large temperature rise is by using a substrate with better thermal conductivity than silicon oxide. At 5K, the thermal conductivity of quartz and sapphire is on the order of 10^3 times better than that of silicon oxide. As the result, the temperature rise is dropped significantly by substituting the substrate. The result indicate that the temperature of the nanowire is highly determined by the thermal boundary resistance, which determined the heat transfer rate from nanowire to substrate. Another method to reduce the local heating is to use the remote excitation surface plasmon propagation to excite the local plasmon mode at nanowire while illuminating laser far away instead of directly at the nanowire itself.

2.3 Broken nanowires with high local enhancements of the electric field

Some other previous studies in the group, discussed strong local enhancements of the electric field within the broken nanowire, as shown in Fig.2.4, within such a nanogap in the junction, we can create a molecular tunnel junctions. This nanogap can be made in two methods: electromigration or a two-step lithography process so called "self-aligned". The major advantage of the electromigration method is the good control of migration process. Since this method uses the electron current to move around the gold atoms, we can control the current to slowly form the nanogap, which allow us to create a truly tiny gap. However, the nanogap created by this method is unstable, most lasting for few hours at room temperature before atomic

rearrangement increases the electrode spacing. In the other hand, the nanogap created from the "self-aligned" process would be much more stable and allows for arrays of devices to be fabricated with nanogaps, but the gap size is typical larger than the gap created from the electromigration method. The two step lithography process could also give more contamination to the device. The "self-aligned" fabrication

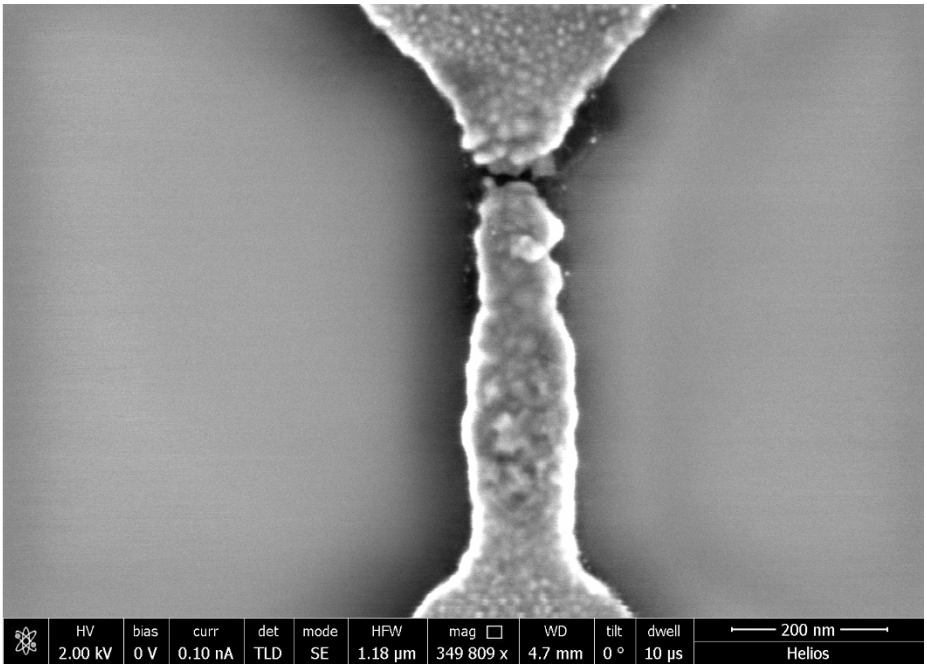

Figure 2.4 : SEM image of an electromigrated gold bowtie device. Clear see a nanogap located on the top section of the nanowire, which is near the fan-out structure.A dark contour with some leftover white dots indicate the structure prior to migration.

process, detailed in Fig.2.5[69], consists of a two-step lithography technique. An initial lithography step patterns half of the device and has an initial deposition of the Au layer, with an additional Cr layer over the Au film. The Cr oxidizes and expands beyond the Au layered pattern. An additional lithography step patterns the second half of the device, which overlaps with the previously-deposited pattern, and an additional Au layer is deposited. After lift-off and Cr etching , the Cr layer

is etched away with those Au overlapped on top of the Cr, resulting in a nanogap within the wire where the Cr expanded.

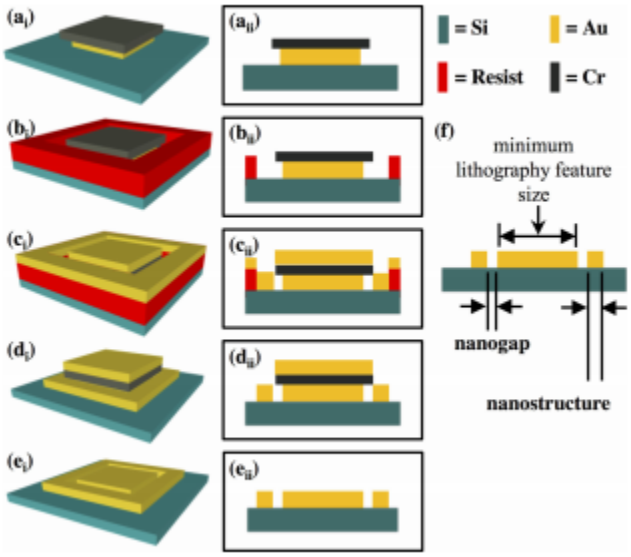

Figure 2.5 : Schematic illustration of the "self-aligned" fabrication process.From ref.[69]

Although electromigration considered as a failure in traditional circuit design, the process can be used to create nanoscale gaps in nanowires.[70] As shown in Fig.2.6, the principal of electromigration is simple: when a current is pushed through a conducting wire by an applied bias, charge carriers travel through the wire. In this case, a high current density is required to move the atoms/ions in the conducting wire. When the the charge carriers pass through the wire, they move past and interact with the stationary ions in the conductor. Momentum exchanges between the charge carriers and the ions can cause the charge carriers to physically push the ions away from the original position, resulting in a nanogap. This pushing is called the electron wind force.[71] Additionally, due to the high electric fields during the electromigration

process, charged defects can be pushed along wire causing further separation. These momentum exchanges most commonly occur when the charge carriers scatter off defects, such as grain boundaries or structural defects like dislocations. When an ion begins to diffuse, the local current density at that location increases, resulting in more scattering and therefore more momentum transfer at that specific location. Using electromigration in a controlled way can allow for consistent nanoscale gap formations in nanowires.

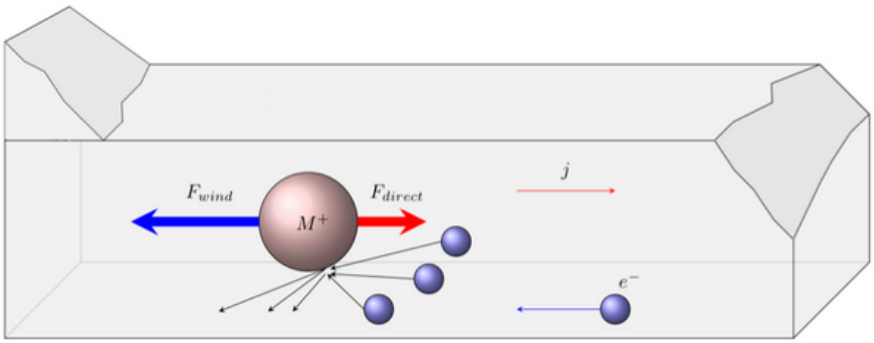

Figure 2.6 : Schematic illustration of the electromigration process.charge carriers hit the ions in the strip;These ions gained momentum and move around.[72]

The specific details of the nanogap can allow for large enhancements of the local electric field, as in Fig.2.7.[66] COMSOL Multiphysics software was used to simulate the electric field enhancement of the nanogap. As expected, when the laser is in the longitudinal polarization, the electric field enhancement and charge distribution are relatively weak, while the largest response occurs when the laser is in the transverse polarization, exciting that local plasmon mode within the nanowire; within the gap, there is large, local enhancements of the electric field specific to the device geometry which is a result of the hybridization of the local transverse plasmon mode with the multipolar modes within the gap.

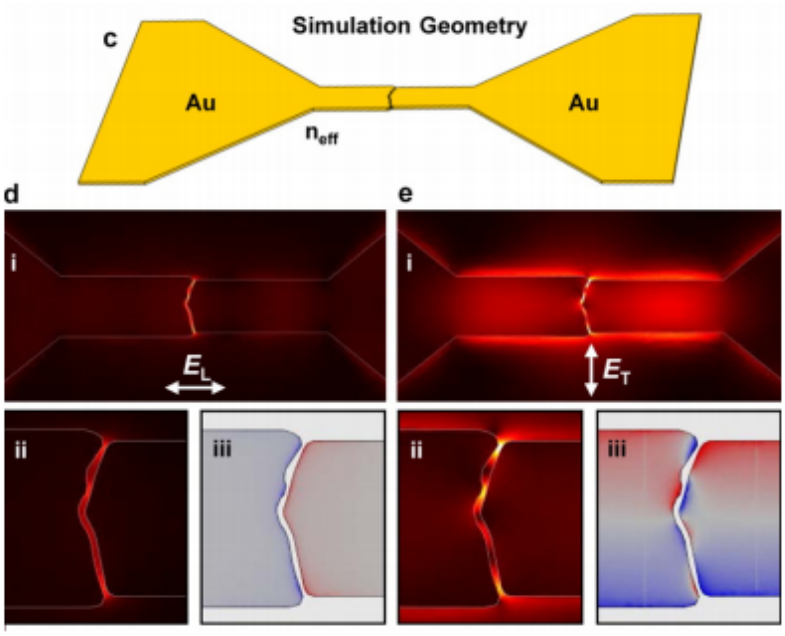

Figure 2.7 : Simulation of electric field enhancement and charge distribution in nanogaps. c: Example of simulation geometry used in finite-element modeling using COMSOL. d, e: results of the simulation of the gap under illumination in the longitudinal(E_L), and transverse(E_T) , polarization, respectively. The local field enhancement within the wire is largest when the laser is in the transverse polarization because of the resonant local transverse plasmon mode in the nanowire. From ref.[66]

2.4 Single molecule SERS and electronic transport measurements

Single molecular SERS can be performed via the large field enhancements from the hybridization of the local, multipolar modes within the gap and the local surface plasmon resonance from the nanowire. From Fig.2.8c,d[66], the 2D maps of the integrated Raman signal near the characteristic Si peak (515 cm^{-1}) as a function of laser position were conducted with the laser in the transverse and longitudinal polarization, respectively. The maps are nearly identical regardless of polarization;

Because the field enhancement is highly localized, the Si peak is not enhanced. When the laser is incident on the gold bowtie, the Si signal is smallest, while when the laser is incident on the substrate and the Si signal is largest . The maps of the characteristic peaks around 1550 cm^{-1} from the applied self-assembled monolayer of BPE(trans-1,2-bis(4-pyridyl)-ethlyene) look much different compare with the Si signal. When the laser is in the transverse polarization, Fig.2.8e[66], there is a "hotspot" of signal within the nanogap, with no detectable signal anywhere else. This hotspot is completely absent when the laser is in the longitudinal polarization, Fig.2.8f[66], indicating that the signal is detected due to SERS.

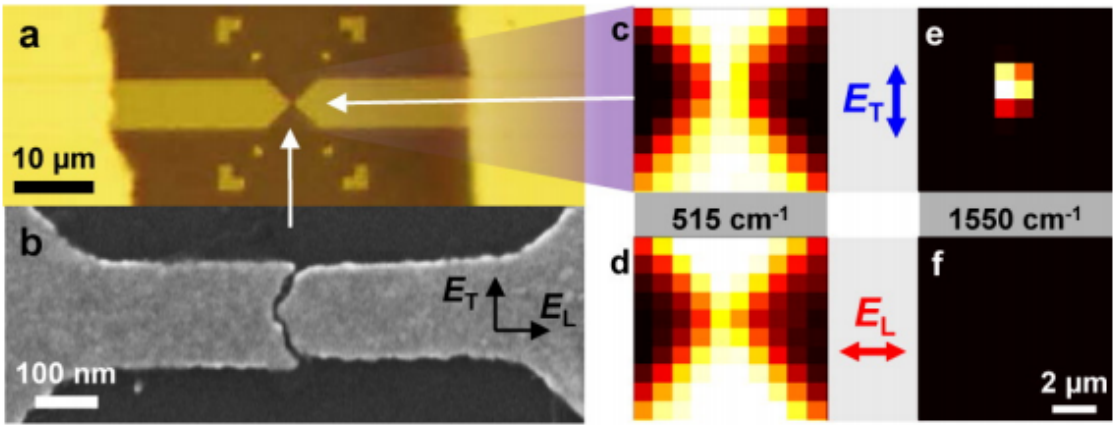

Figure 2.8 : a,b detail SEM image of the device. c,d Map plot of Si Raman peak with laser illumination in the longitudinal(E_L), and transverse(E_T) , polarization, respectively. e,f. Map plot of BEF Raman peak with laser illumination in the longitudinal(E_L), and transverse(E_T) , polarization, respectively. From ref.[66]

The Raman intensity within the hotspot under the transverse and longitudinal polarization are compared in Fig.2.9[66]. As the result, the BPE Raman signals are clearly visible when the laser is in the transverse polarization and are not detected at all in the longitudinal polarization. This indicates that the high local field enhance-

ment due to the plasmonic modes within the gap is responsible for the SERS signal. This experiment result matches the simulation result from COMSOL.

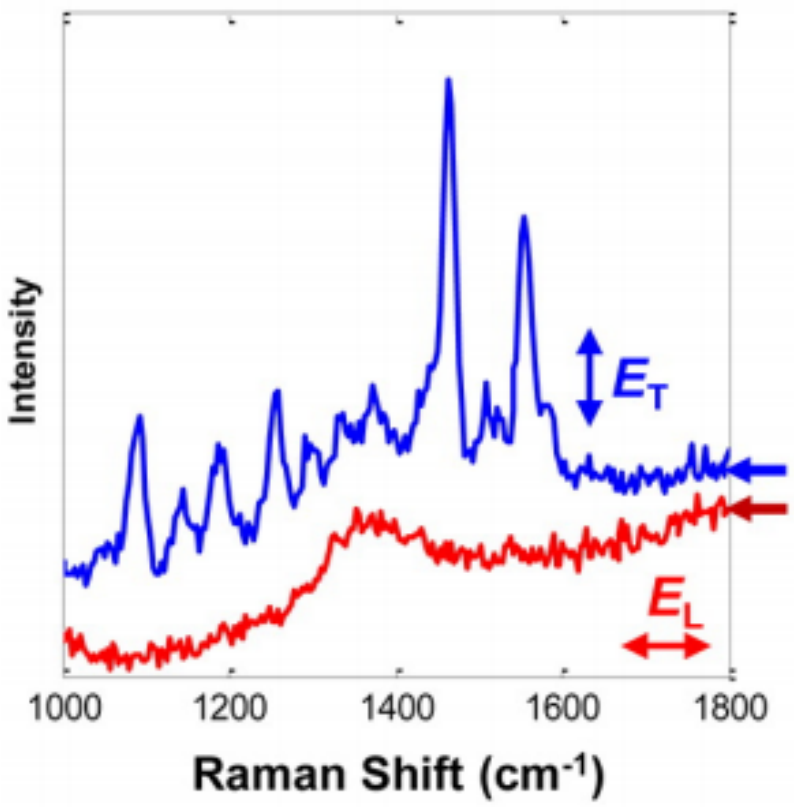

Figure 2.9 : Raman spectrum of BEP with laser illumination in the longitudinal(E_L), and transverse(E_T) , polarization, respectively. The local field enhancement within the wire is largest when the laser is in the transverse polarization because of the resonant local transverse plasmon mode in the nanowire. From ref.[66]

The previous research work shows the capability of this gold bowtie devices can allow for single molecule Raman measurements. One major advantage of this device is that it we can combine the Raman spectroscopy and conductance measurement together. The conductance as a function of applied bias can provide insight about when a tunneling electron exchanges energy with a molecule, exciting a vibrational mode in the molecule. Later in Chapter 6, attempts are discussed in trying to perform

SERS measurements on monolayer transition metal dichalcogenides(e.g.,MoS_2). For motivating context, in one example[64] of using the highly local Raman enhancement combined with transport, prior group members investigated the response of molecular Raman modes to electrical bias.

Additional research[64] presents voltage-driven shifts of vibrational mode energies of C_{60} molecules in gold junctions. C_{60} mode energies are found to vary approximately quadratically with bias, but in a manner inconsistent with a simple vibrational Stark effect. Theoretical model instead suggests that the mode shifts are a signature of bias-driven addition of electronic charge to the molecule. These results imply that voltage-controlled tuning of vibrational modes is a general phenomenon at metal–molecule interfaces and is a means of achieving significant shifts in vibrational energies relative to a pure Stark effect.

Fig.2.10 shows Stokes spectra of C_{60} as a function of applied bias. The main experimental observation is that many of the vibrational modes with energies greater than 1000 cm^{-1} shift toward low energies as the applied bias increases. These systematic shifts are observed routinely in C_{60} based junctions.

To understand the mechanism, DFT is used to compute the vibrational frequencies of C_{60} as a function of external field and charge state. One may infer the effect of partial molecular charging in the junction from calculations of a single partially charged C_{60} molecule. A fractional occupation of the C_{60} lowest unoccupied molecular orbital(LUMO) upon adsorption into a junction is consistent with the established large electronegativity of C_{60}. As the molecule is (partially) charged, several C_{60} vibrational modes shift systematically to lower energies, by tens of cm^{-1}. We compute that these are Raman active H_g modes that couple strongly to the t_1u LUMO and are present throughout the 1000 to 1600 cm^{-1} range (Fig.2.11[64]). This trend is

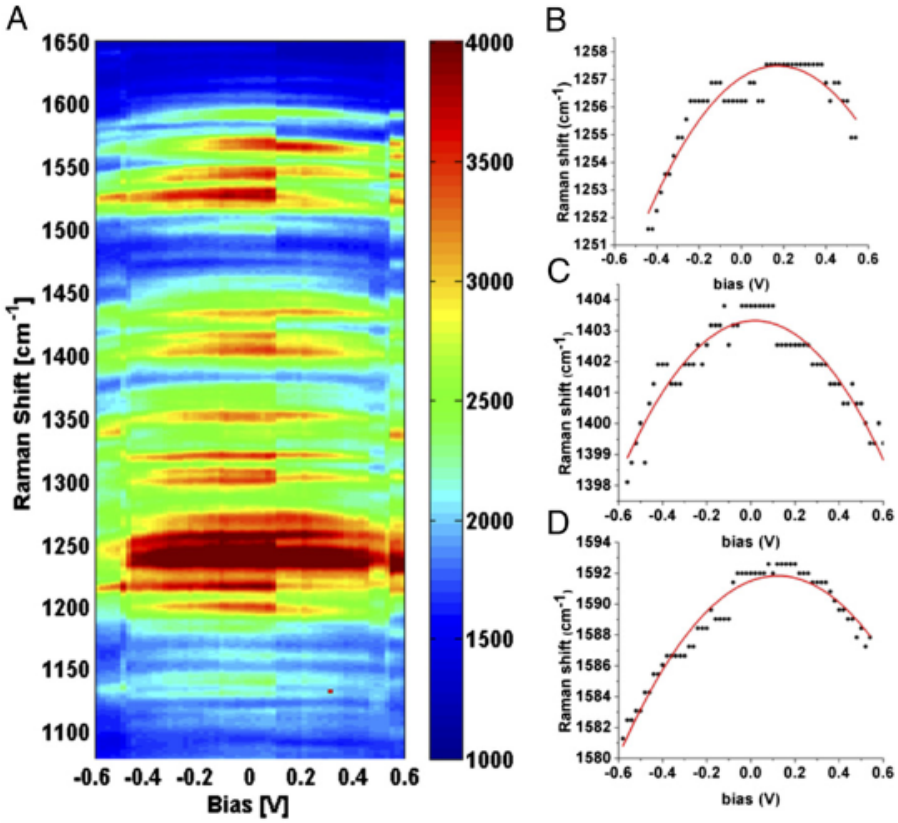

Figure 2.10 : Bias-driven vibrational energy shifts. (A) Raman response as a function of bias and Raman shift. The sudden change in the intensity at around 0.1 V is the result of blinking. (B,C,D) Vibrational energy shift as a function of bias for three particular modes: 1258 cm^{-1}, 1404 cm^{-1} and 1592 cm^{-1}. From ref.[64]

reasonable on general chemistry grounds: Adding an electron to the neutral C_{60} occupies an antibonding LUMO that is delocalized over the entire molecule, thereby softening many intramolecular bonds.Thus, a red shift of vibrational modes coupled to an antibonding LUMO upon electronic charging would be expected quite generally.

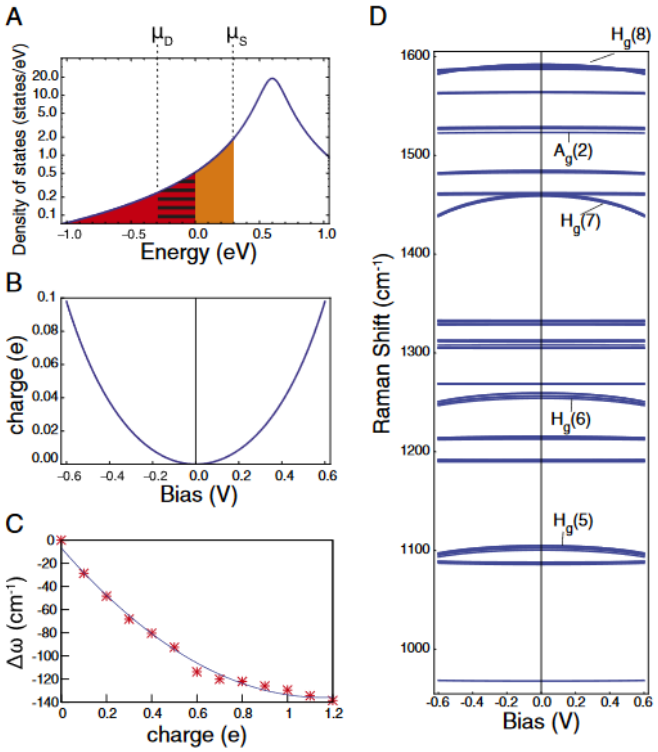

Figure 2.11 : Model of bias driven changes in molecular charging. (A) At zero bias, the triply degenerate LUMO resonance, is occupied proportionally by the red shading. As the bias applied, the molecular level gains additional occupation proportional to the area shown by the orange shading and loses occupation proportional to the hatched portion of the Lorentzian. (B) The expression for charging with bias at 80 K is visually identical to the charging at 0 K. The change in partial charge is approximately quadratic in bias. (C)A representative mode's [$H_g(7)$ at 1467 cm^{-1}] change in vibrational energy with charging. This dependence, combined with the variation incharge with bias, strongly suggests that bias driven charging is the origin of the systematic mode softening observed in the experiments. (D) Mode energies as a function of bias from such a calculation.From ref.[64]

2.5 Substantial local variation of the local Seebeck coefficient in polycrystalline gold nanowires

From Chapter 1, how nanostructuring can allow for single metal thermocouples was discussed. Changing the geometry of a nanoscale device can change the lo-

cal boundary scattering, therefore changing the local Seebeck coefficient. The standard "bowtie" devices with a nanowire with a length around 600 nm were measured, Fig. 2.12a.[73] The steady-state, integrated open circuit photovoltage of the device was measured as a function of laser position, which was raster scanned around the nanowire and fan-out electrodes. The map of this measurement is seen in Fig. 2.12c. As expected, shining the laser at the interface of the fan-out electrode and the nanowire resulted in a change of photovoltage, because at that location, the electronic mean free path changes due to the change in nanostructuring. Shining the laser on the opposite end of the the nanowire shows a similar magnitude of photovoltage, but of the opposite polarity, indicating that this is due to the change in local Seebeck coefficient.

Because of the length of the nanowire is shorter than the laser spot, detail of the local Seeback effect can not observed. If we extended the length of the nanowire to 10 μm , more detail information on the local Seebeck coefficient can be obtained as Fig2.13a shows. The traditional theory of nanostructured single metal thermocouples would predict devices of uniform width and thickness to have a constant Seebeck coefficient. Hence, there should be completely featureless that the PTE signal along the length of the extended nanowire. Instead, the PTE map showed surprising local variations along the length of the wire. The PTE signal not only varied in magnitude but also in polarity. As seen in Fig.2.13b, these changes were observed within the spot size of the laser. In some cases, the variation in signal could be explained by a defect in the wire, as seen in Fig.2.13e, but for the most part, there was no obvious explanation to the inhomogeneity of the photovoltage response due to SEM images alone, Figs.2.13c,d. We will discuss the dominant mechanism that causes this effect in Chapter 5.

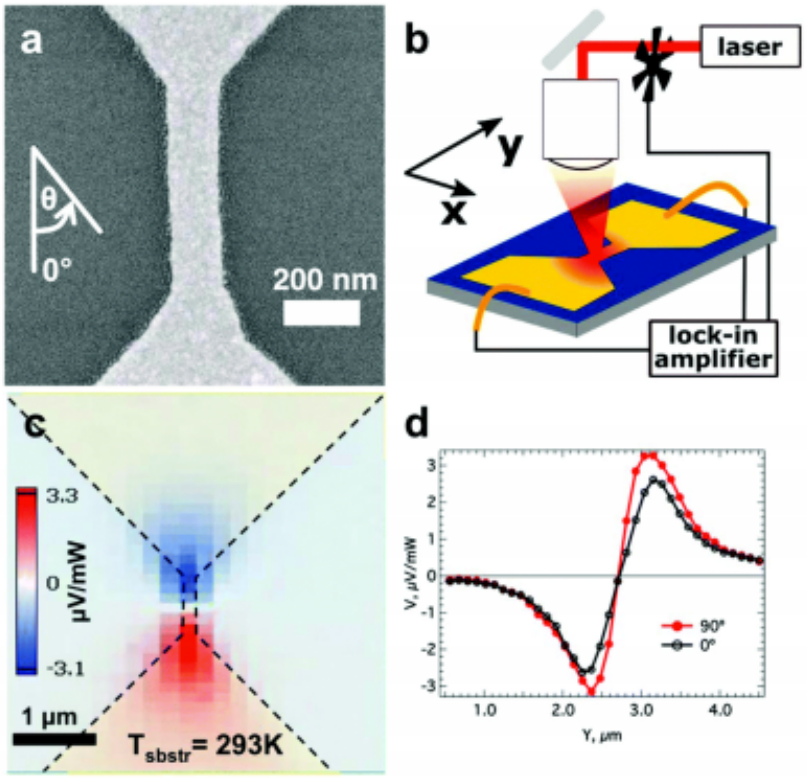

Figure 2.12 : Photothermoelectric measurements of a standard gold bowtie device. a: SEM image of a standard device, b: schematic of the measurement setup. c: 2D PTE map of the standard gold bowtie device. d: Scatter plot of c, showing the PTE signal along the length of the device. The black line shows PTE signal when the laser is in the longitudinal polarization (along the length of the nanowire), whereas the red line indicates the transverse polarization (perpendicular to the nanowire).From ref.[73]

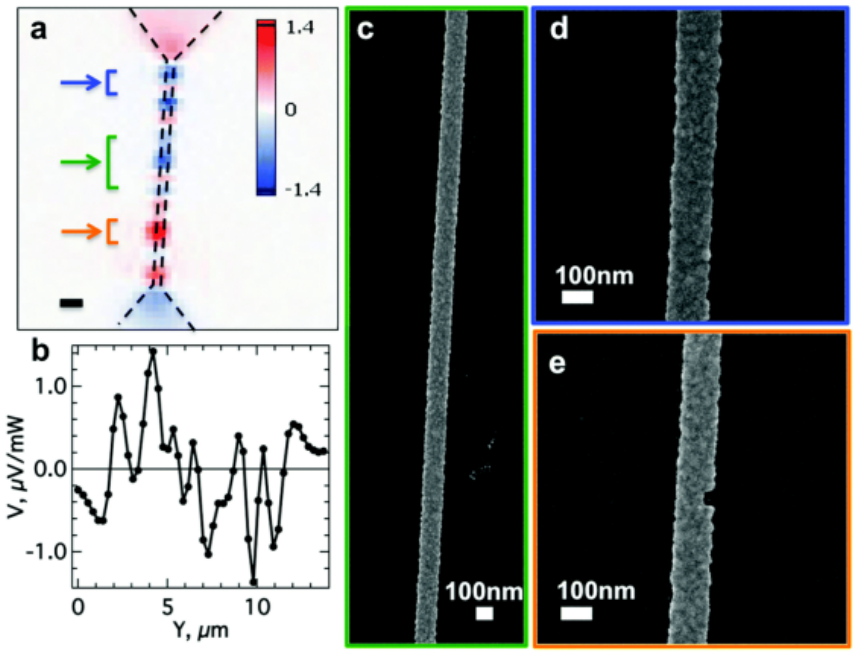

Figure 2.13 : Photothermoelectric measurements of an extended gold bowtie device. a: 2D PTE map of a bowtie device with a 10 μm long nanowire. The scale bar is 1 μm. The units is μV/mW. b: Scatter plot of the PTE signal along the length of the device. c,d,e: SEM images along the length of the device. The displayed area is highlighted by brackets in a that are the same color as the boxed outline.From ref.[73]

Chapter 3

Experimental Methodology

Measurement instruments are essential in experimental physics. Good and reliable experimental setups and scientific experimental designs are necessary to reach any solid conclusion. This chapter will mainly introduce the experimental instruments used in this research as well as the process and measurement methodology.

3.1 Fabrication system

3.1.1 Scanning electron microscope and lithography techniques

The scanning electron microscope is one of the major piece of equipment necessary for our experiment. The gold "bowtie" is fabricated via e beam lithography and the majority of the devices are patterned on the JEOL 6500F SEM. The JEOL 6500F is a Field Emission Scanning Electron Microscope (FESEM) with Electron Beam Lithography attachment,and Nanometer Pattern Generation Systems (NPGS). It offers high resolution images of very small inorganic and organic surface structures and the NPGS attachment enables lithography applications for semiconductor processing. This system is routinely used to create structures with features down to 50 nm. The NPGS system controls a high speed electrostatic beam blanker installed in the SEM to perform lithograph to achieve the designed patterned. The SEM itself is also a powerful characterization tool for analysing the structure via using a accelerated electron beam to hit the surface of the specimen and detecting the secondary electrons

by the scattering, as Fig.3.1[74] shows.

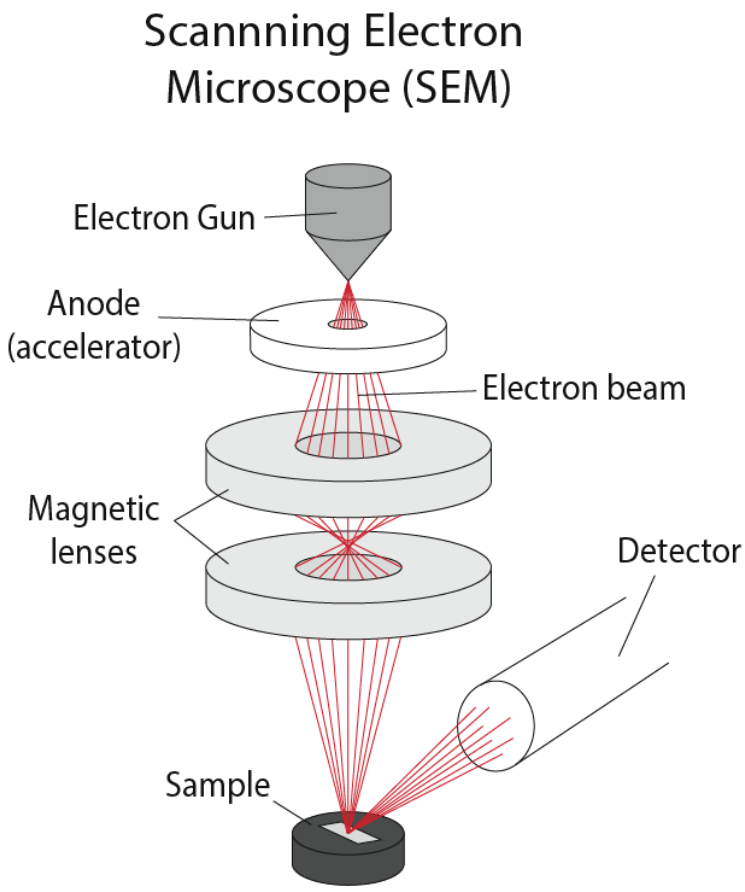

Figure 3.1 : Schematic illustration of SEM. Electron is emitted from a filament and accelerated via a anode and focused through set of magnetic lens. The focused electron beam then raster scan on the surface of the sample, and a detector close to sample to detect the secondary electrons kick out from the sample and based on the intensity of the detected electrons to construct the map as function of scan position. From ref.[74]

Lithography is the process of transferring some geometric shapes onto a mask to a smooth surface. It is one of the most intensively used techniques for making integrated circuits both in laboratory and industrial scale. The general idea of lithography is

using some sensitive chemical resist and by degrading certain areas of the resist to create some uncovered regions on substrate. Through the degrade process used to the chemical resist, lithography can be categorized as photo lithography, e-beam lithography or focused-ion-beam lithography, etc.[75] The basic photo lithography and e-beam lithography process are shown in Fig.3.2.[76]

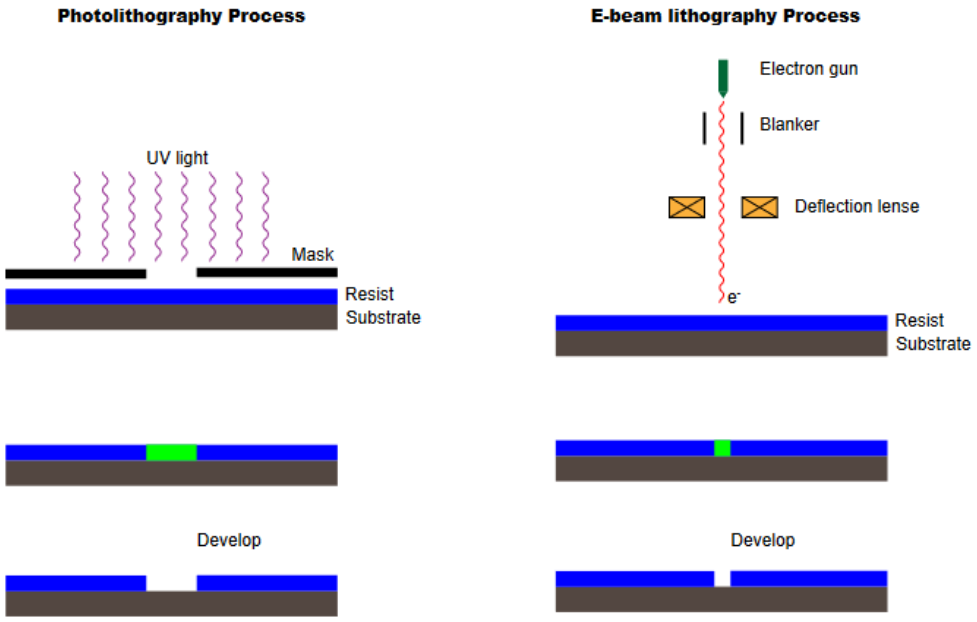

Figure 3.2 : Schematic illustration of positive tone photo lithography and e-beam lithography processes. From ref.[76]

For photo lithography, a photo mask created first, which is usually made from glass and with one side coated with opaque metal such as chromium. The coating leaves out some designated space where UV light can transmit through. Then, we spin-coat the target substrate with photo resist. Usually, we use a positive-tone Shipley S1813 as the resist in our lab. The coated substrate is covered and tightly contacted by the photo mask,and UV light is radiated onto the resist through the mask. The

development process removes the photo resist in radiated areas, and the pattern is transferred from the mask to the substrate.

E-beam lithography shares similar processes. In e-beam lithography, we use e-beam resist polymethyl methacrylate (PMMA) instead of photo resist. PMMA 450(number stands for the typical length of the polymer chain) is thin and good for fabricating fine structures; PMMA 450/PMMA 950 bilayer resist is good for smooth lift-off. E-beam lithography is mask free. We can define arbitrary patterns and use a focused electron beam to sweep across the pattern. The area radiated by the e-beam will degrade and be washed away in developer. As the resolution is limited by the wavelength, the e-beam lithography has much higher ($\sim$ 1 nm) compared to photo lithography ($\sim$ 1000 nm)

3.1.2 Material evaporation/deposition

Evaporation is a common method for thin film deposition. In the evaporation process,the target material is heated up by a high energy electron beam (e-beam evaporator) or heat source (thermal evaporator). For any material, there exists a finite vapor pressure, thus after heating, the material either sublimes or evaporates.[77] As the chamber pressure is extremely low, the material vapor can travel to the substrate without too much scattering. A quartz resonator is installed closed to the target to monitor the thickness of evaporated material. With material deposited onto the quartz resonator,the oscillation frequency of the resonator will shift, and the deposition rate can be calculated from this shift. By controlling the evaporation rate, we can well control the thickness of the thin film and with a very small tolerance. Since all the devices in this thesis are deposited via e-beam evaporator, a schematic illustration of e-beam evaporation processes shows in Fig. 3.3[78] to give a clear view

of how the system works. Electrons emitted from a heated up tungsten filament and travel under a magnetic field to hit the crucible filled with the target material. With the high current density the target material will melt and finally evaporate. The material vapor will land on the lithographic designed substrate that is placed on the top of the chamber.

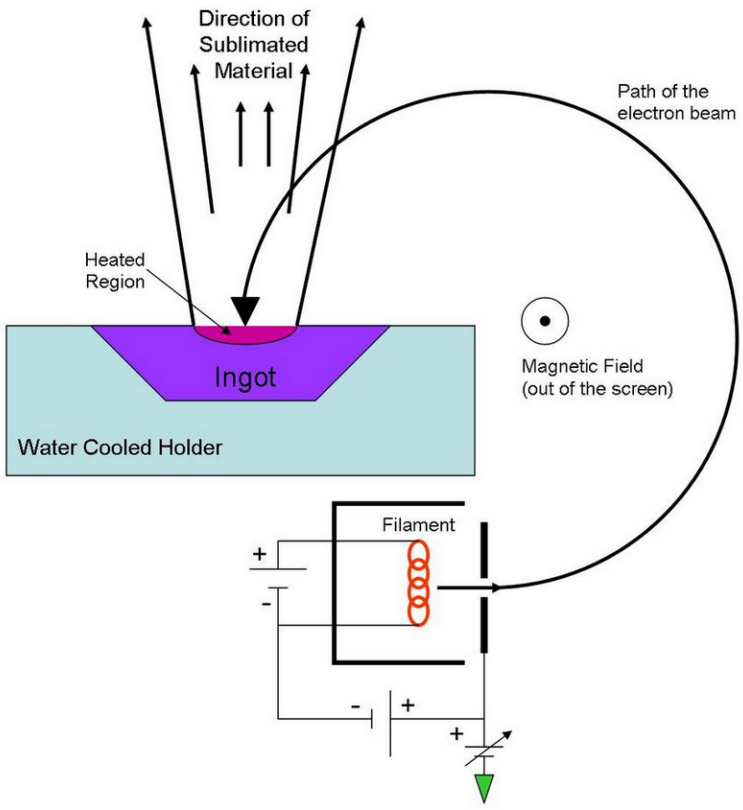

Figure 3.3 : Schematic illustration of e-beam evaporation processes. A tungsten filament is heated up enough that can emit electrons. The electrons then travel under a magnetic field to hit the crucible with the target material. With the high current density the target material will melt and finally evaporate. The lithographic designed substrate will place on the top of the chamber, wait for the material vapor to land. From ref.[78]

The evaporation method has the advantage of high purity due to ultra-high vacuum. Also, if we can precisely control each crucible's temperature, we can realize

more complex applications include the co-deposition of several layers. However, the evaporation method has poor step coverage, and it is difficult to form alloys. Also, the process is relatively slow compared to other deposition techniques like sputtering or electroplating.

3.1.3 Plasma cleaning

Plasma cleaning is the technique that uses gas plasma to remove organic contaminants from wire bonding or substrate surfaces. By removing surface contamination, plasma cleaning increases the bonding or adhesive properties of the surface.

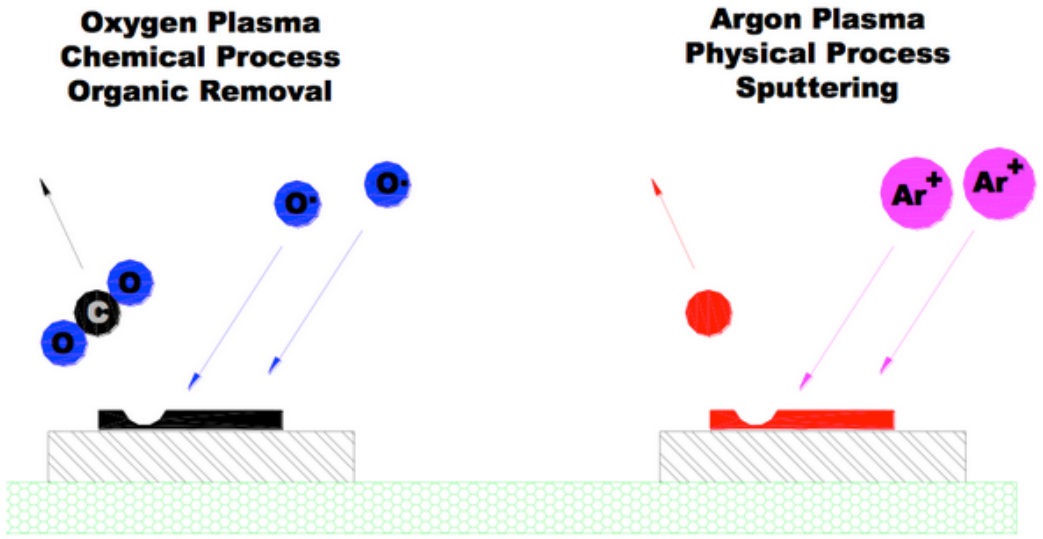

Figure 3.4 : Schematic illustration of plasma cleaning processes. Left: Highly reactive oxygen ions react with organic residue on the surface and form CO_2. Right: Argon ions physically kick out the atom on the surface. From ref.[79]

When a neutral gas molecule is struck via an energetic electron, it can be dissociated and generate free radicals and ions. The contaminants can be removed by

these free radicals via chemical reactions. Given an example, oxygen, a typical gas for plasma cleaning, the free radical atomic oxygen (O) can be generated from the dissociation process produces. This reactive species has enough energy to break a carbon-carbon bond.(see Fig.3.4[79] left). For inert gas like Ar, instead of forming chemical compounds, Ar ions physically kick out atoms on the surface.

In our experiments, we mainly use oxygen plasma to clean the organic residue prior to deposition and a surprising result on the gold oxide via oxygen plasma will be discussed in Chapter 4.

3.1.4 Wire bonding

Wire bonding techniques are vital to the semiconductor industry. Wirebonding makes interconnections between the electronic devices. In our experiments, wire bonder often used to connect the device to our measurement setups. A general process for wedge bonding is illustrated in Fig.3.5.[80] A metal wire(e.g., Au) guided by the wedge tool approach to the bonding pads on the device. When the tool contacted the pads, an ultrasound wave applied to the wedge to melt the head of the wire and form the first bond. Then, the tool moves to the second pads and repeats the same procedure to create the second bond, but this time the clamp will cut the wire after the second bond formed.

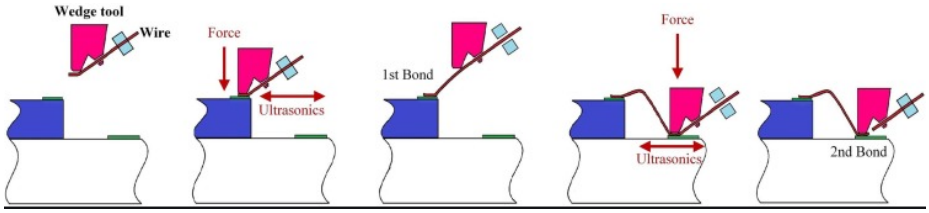

Figure 3.5 : Schematic illustration of wedge bonding processes. A metal wire(e.g Au) guided by the wedge tool approach to the bonding pads on the device. When the tool contacted the pads, a ultrasound wave applied to the wedge to melt the head of the wire and form the first bond. Then the tool moves to the second pads and repeats the same procedure to create the second bond, but this time the clamp will cut the wire after the second bond formed. From ref.[80]

3.2 Measurement system

3.2.1 Conductance and differential conductance measurement

Transport measurement is one of the basic tools in the study of materials. Ohm's law defines the resistance of a conductor as:

$$R = \frac{V}{I}$$

where V is the voltage across the sample and I is the current. Conductance (G) is defined as the reciprocal of the resistance by G = 1/R. In linear response, this is a complete description. For a more general $I(V)$, at any given bias condition one can define the differential conductance $G = dI/dV$ or the differential resistance $R = dV/dI$.

The most direct and simple way to measure the resistance/conductance is the two terminal measurement method, where current I is applied to two leads of the sample, and the voltage V is also measured at the same leads, see Figure 3.6. The differential conductance dI/dV is a measure of how much change in I takes place when the bias V

is changed by a small amount. The differential conductance is maximized at voltages where the transmission of electrons through the sample is most strongly altered with a change in bias. This can be due to a large density of states for the charge carriers, and/or a maximum in the electronic transmission as a function of energy. dI/dV can be directly measured by superimposing a low amplitude AC excitation on a stepped DC bias; then using a lock-in amplifier to measure the resulting AC voltage across the device and the DC current through the device.

3.2.2 Optical and electronic measurements measurement

For our optoelectronic measurement, we have a home built Raman system which is combined with a cryostation(a closed cycle optical cryostat manufactured by Montana Instruments) and interfaced with measurement electronics, including biasing circuitry, current and voltage preamplifiers, and lock-in amplifiers. The entire system allows us to combine optics and electrical, and has the additional ability to cool the sample to near the temperature of liquid helium..

Home built Raman microscope

Since we want to combine the electric and optical measurement together, we built a custom designed Raman system in our lab. The system diagram is shown in Fig. 3.6.[4] The choice of the laser is a CW 785 nm red light laser purchased from Toptica iBeam. The reasons for using a 785 nm laser are: 1. Based on the resonance geometry of the gold nanowire, the resonance width for this typical "bowtie" is around 120 nm for 785 nm incident laser, while for a 532 nm laser, the resonance width is reduced down to 40nm, which increases the difficulty of fabrication significantly. 2. For organic molecules, 785 nm laser gives a very strong Raman peak and some carbon

bonds have resonant vibration mode near 785 nm(e.g., graphene[81]). The laser itself also connects to the measurement PC via USB port. With the control software, the output power of the laser can be tuned from 0.1 mW to 100 mW. All optics are mounting on an optical table to minimize the vibration during experiments.

When the light is emitted from the laser pump, it is reflected twice by two silver mirrors and passes through an optical isolator, which force the laser to only transmit forward. Then, the laser is reflected by few mirrors and two OptiGrate BragGrate^{TM} Spatial Filter (BSF). The major benefit by using a BSF is that it only allows the light with 785 nm can be reflected at a specific angle and filtered out light with the other wavelengths. Since the BSF only can reflect the laser at a fixed specific angle with a high sensitivity, that means a tiny change for the laser path can fail the alignment. Hence, the position of laser needed to be tuned for every power cycle. An neutral density filter wheel is placed right after the set of BSF and mirrors, which provides more flexibility on the laser intensity. This wheel is controlled by a step motor that is connected to PC. A 95/5 beam spiltter is placed after the neutral density filter, which splits roughly 5 percent of the total light into a power detector to measure the laser power. An optical chopper stands behind this beam spiltter to chop the light with half time on and half time off. It also provides the reference signal for lock-in amplifier. Then, the laser is reflected via a mirror and pass through a 100 or 50 μm pinhole in a beam expander configuration to clean the beam mode. A polarizer with a controllable angle $\lambda/2$ waveplate is placed right after the pinhole, which can change the polarization of the laser. Two mirrors then reflect the laser to a notch filter that allow for the incident and exiting beam from the sample to travel the same path. A set of OptiGrate's BragGrate^{TM} Notch Filters used to reduce the Rayleigh peak for Raman measurements. Similar to the BSF, these notch filters are aligned in the same

way as the BSF but only the light that is not 785 nm is allowed to pass through the notch filter without affecting its path. A feedback close loop piezo nanopositioner controller (Newport's NPC3SG) control used to control the first lens of a final beam expander before the laser reflect through a set of mirrors. A motor controlled beam splitter is placed between the mirror, and the final beam expander to allow for white light illumination and imaging via a CCD camera. The laser is finally focused by a 50x (NA=0.7) objective lens down through the low working distance optical window of the cryostation. Since the focus spot of the laser is fixed after the objective, a piezo controlled stage used to move the chip in 3 dimension to match the device with the laser spot(around 1.6 μm). The laser travels back through the same path reflects back from the silicon chip. Before the laser reach the Raman Spectroscopy(Horiba Jobin Yvon iHR 320 spectrometer), it passes through an additional two notch filters and a slit(0.1mm) to reduce the scattered light from the environment.

Photothermoelectric effect measurement

Light intensity is modulated via an optical chopper the a fixed frequency, which is much slower than the thermalization time scale of the devices. The chopper also provides the reference frequency to SR7270 lock-in amplifier for the Photothermoelectric voltage measurement. The integrated steady state voltage at each end of the device was measured using the SR560 voltage amplifier (100 MΩ input impedance) with the potential difference between the two ends being measured as the input of a SR7270 lock-in amplifier. Unless otherwise specified, the measurements were conducted at room temperature. The schematic of the measurement setup is seen in Fig.3.7.

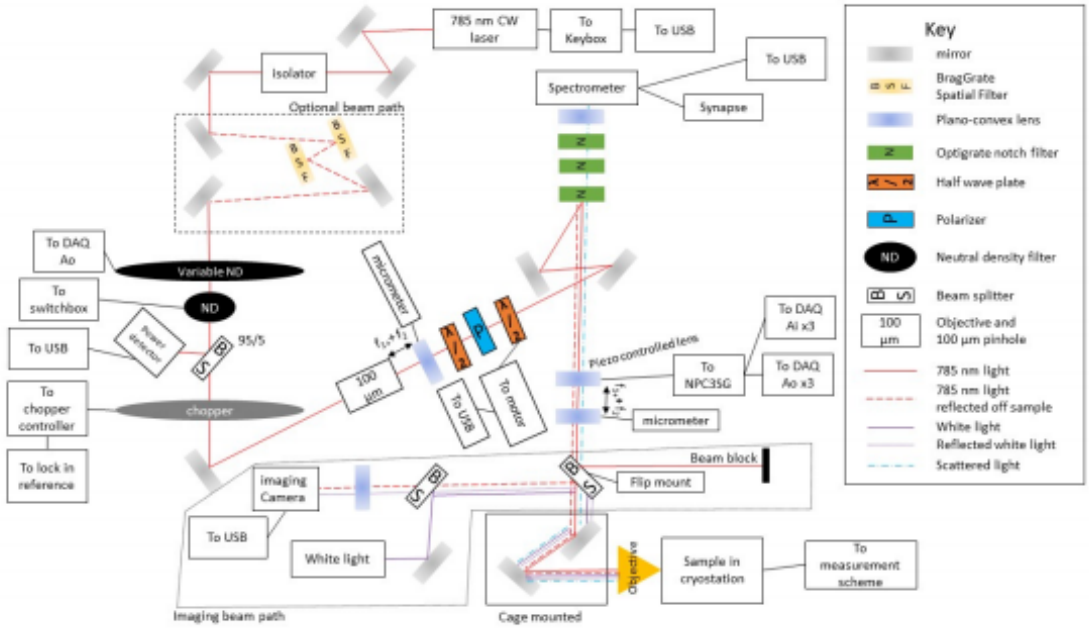

Figure 3.6 : Schematic illustration of the homemade Raman microscope setup. From ref.[4]

3.2.3 Surface potential/work function measurement

In Chapter 5, we investigated the mechanisms that affect the local Seebeck coefficient. One method that we attempted is to alter the surface potential via a self-assembled monolayer(SAM) on the surface of the device. Work function (or surface potential for nonmetal) is one of the important properties of solid surfaces. Valence electrons are confined to the surface of metals by a surface potential barrier. The work function of a metal is the energy required to take an electron at the Fermi level and remove it to infinity.[82]

While photoemission is the historically traditional way to measure metal work functions[83], scanned probe methods have recently become widely available[84].The surface potential/work function measurement is performed with a Park system NX20

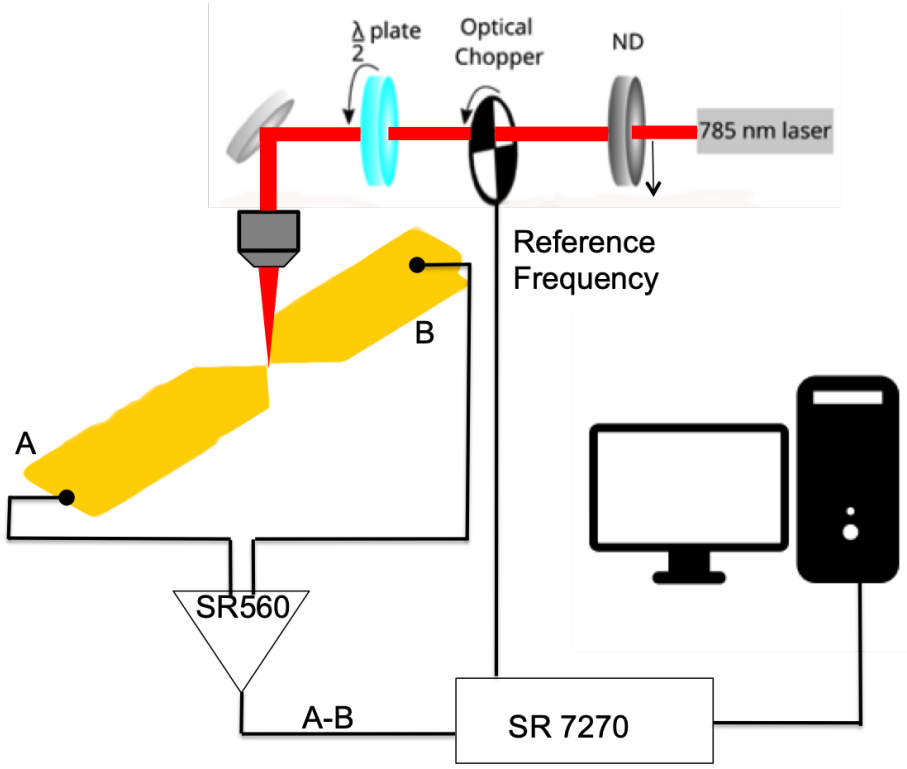

Figure 3.7 : Schematic of the photothermoelectric effect measurement.

atomic force microscope(AFM). This AFM has the capability for Kelvin probe force microscopy (KPFM), also known as surface potential microscopy. As shown in Fig.3.8[85], an external lock-in amplifier is connected to the AFM for two purposes. One is to apply an AC bias of frequency (ω) to the tip in addition to the DC bias being applied by the AFM controller. The other purpose is to separate the frequency (ω) component from the output signal. In principle, KPFM is similar to electrostatic force microscopy (EFM) with DC bias feedback (Fig.3.8[85]). DC bias is controlled by a feedback loop to zero the ω term. The DC bias applied to the tip that zeros the force between the tip and the sample is a measure of the difference in surface potential between the tip and the sample. The difference between EFM and KPFM

is in the way the signal obtained from the lock-in amplifier is processed. For the KPFM measurement a voltage is applied between tip and sample, consisting of a DC bias V_{DC} and an AC voltage V_{AC} with $\sin \omega t$ of frequency ω from lock-in amplifier can be expressed as following equation:[86]

$$V = (V_{DC} - V_S) + V_{AC} \sin \omega t$$

The amplitude of the ω signal is zero when $V_{DC} = V_S$ or when the DC offset bias matches the surface potential of the sample. A feedback loop can be added to the system and vary the DC offset bias such that the output of the lock-in amplifier that measures the ω signal is zero. This value of the DC offset bias that zeroes the ω signal is then a measure of the relative surface potential.

3.3 Gold "bowtie" fabrication process

Gold "bowtie" is the signature structure, which used extensively in our research. In the beginning, a silicon wafer with 300 nm thermally grown oxide is cleaned via acetone and piranha etch prior to deposition. Then, a shadow mask with designed Bonding pads and a common ground is placed on the wafer. The wafer is transferred to the electron beam (E-Beam) evaporator(Edwards FL 400) and 5 nm Ti/50 nm Au deposited on the wafer. The whole wafer is then cut by a dicing saw to 5mm by 5mm square chip size. Chips are sonicated in acetone and rinsed in isopropyl alcohol (IPA) and blown dry. Prior to coating the e beam resistor, the chips are additional cleaned with oxygen plasma via in house plasma cleaner(Harrick PDC-32 G) for 2 mins under high power. A two layer method is using here to coat the e beam resistor that can ease the difficulty in the later development process. First layer of PMMA

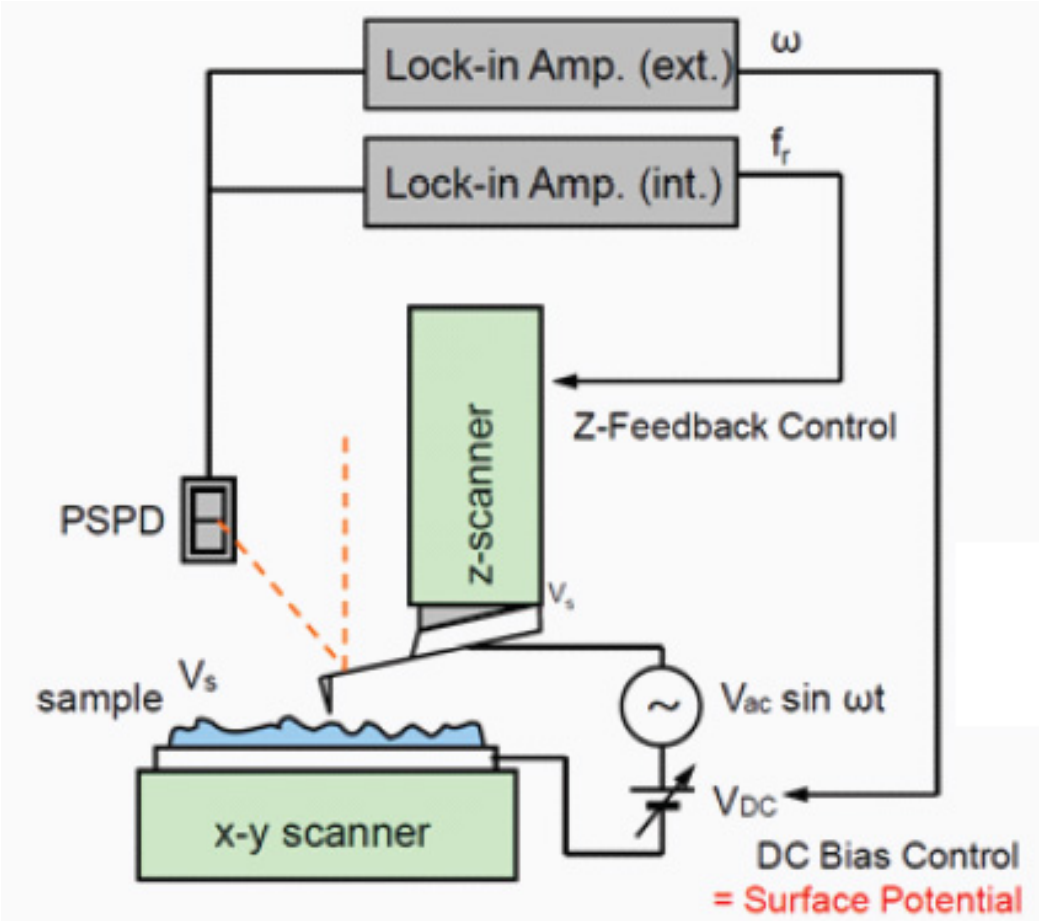

Figure 3.8 : Schematic diagram of the KPFM of the Park AFM series. From ref.[85]

495 A4 in Anisole (Microchem) is spin coated at 3000 RPM for 40 seconds.The chip is then cooked at 180 °C for 90 seconds. The second layer of PMMA 950 A4 is spin coated at 4000 RPM for 60 seconds and cooked at 180 °C for another 90 seconds. The gold "bowtie" devices are lithographically defined using the JEOL 6500 and Nabity software. A typical bowtie consist of nanowire, approximately 120 nm wide and 600 nm long, and reaches out by two fan-out electrodes. The electrodes extend out at 45 angles until reaching the width of 10 μm. The electrodes eventually reaching the bonding pad with same width (10 μm) For the longer version of bowties, instead of

600 nm, a nanowire that is still approximately 120 nm wide but has an extended length, typically 10 μm long. After lithography, the devices are developed in 3:1 IPA: methyl isobutyl ketone (MIBK) for 1 minute. Followed by rinsing with IPA and blown dry with N2. The chip is then processed with Oxygen plasma cleaning on low power for 10 seconds prior to evaporation. 1 nm of Ti (Cr if specially noted) is deposited as an adhesion layer and around 15 nm of Au is deposited afterward, at an average rate of 7 Å/s. Finally, the sample is immersed in acetone for "lift off", followed with sonication, IPA rinsing, and blown dry.

Chapter 4

Photothermoelectric Detection of Gold Oxide Nonthermal Decomposition

A thin coating of gold oxide, metastable at room temperature,can be formed by placing gold in a strongly oxidizing environment such as an oxygen plasma. We report scanning photovoltage measurements of litho-graphically defined gold nanowires subsequent to oxygen plasma exposure.Photovoltages are detected during the first optical scan of the devices that are several times larger than those mapped on subsequent scans. The first-scan enhanced photovoltage correlates with a reduction of the electrical resistance of the nanostructure back to preoxygen-exposure levels. Repeating oxygen plasma exposure"reinitializes"the devices. These combined photovoltage and transport measurements imply that the enhanced photovoltage results from the photothermoelectric response of a junction between Au and oxidized Au,with an optically driven decomposition of the oxide. Comparisons with the known temperature-dependent kinetics of AuO_x decomposition suggest that the light-driven decomposition is not a purely thermal effect. These experiments demonstrate that combined optical and electronic measurements can provide a window on surface-sensitive photochemical processes.

4.1 Motivation and background

As we discussed in previous chapters, gold is a metal of choice for many electronics, plasmonics,and surface functionalization applications, thanks in part to its high

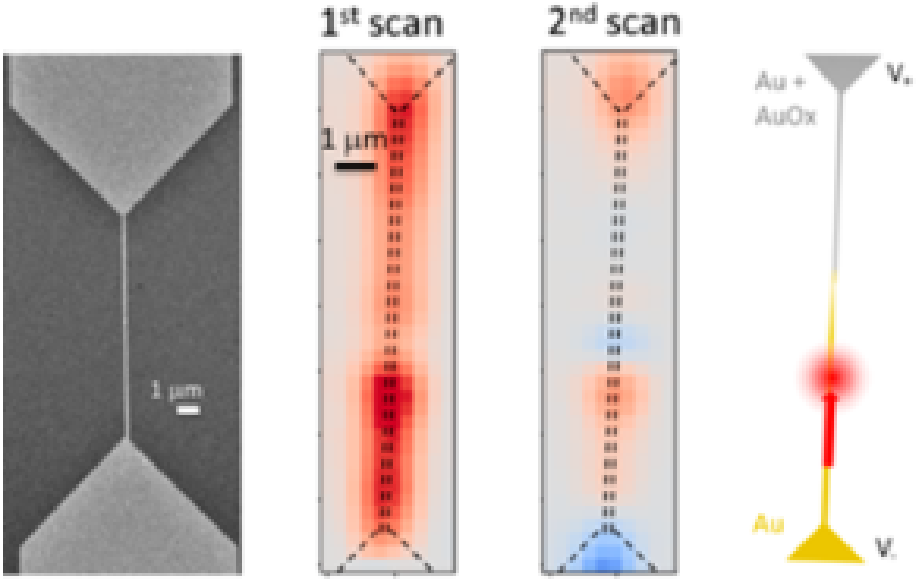

Figure 4.1 : Laser scanning on AuO_x.From left to right, the SEM image of the device with 120nm width 10μm length; the first scan after the device treated in oxygen plasma; the second scan after the device treated in oxygen plasma; schematic of the process: gold oxide decomposes with laser scan over the nanowire.

electrical conductivity and comparative lack of reactivity with atmospheric oxygen. When exposed to an extremely oxidizing environment, however, it is possible to form metastable gold oxide. The presence of such an oxide can be determined directly via X-ray photo emission spectroscopy[87, 88, 89], and indirectly through changes in work function[90],electrical resistivity[91],and electrochemical response[92]. This oxide is known to decompose on the time scale of minutes at temperatures above 150°C, with a characteristic energy scale for the kinetics of around 0.6 eV[88].

Combining electronic measurements with optical excitation has enabled scanning photothermoelectric characterization of electronic nanostructures.[93, 23, 73, 94] A focused laser may be raster-scanned over the sample as a scannable heat source, with the measured open-circuit photovoltage providing a means of assessing the integrated thermoelectric response. Recent experiments on Au nanowires have revealed a surpris-

ing spatial dependence of the photothermoelectric response even in metal nanowires with low sheet resistances compared to the resistance quantum[73],ascribed to local variations of the Seebeck coefficient due to the granular structure of the material.

4.2 Thermoelectric response and gold oxide decomposition

The thermoelectric response of nanostructures can be sensitive to surface conditions, as interfacial scattering affects both the energy dependent electronic conductivity (a key ingredient of the Mott-Jones component of the Seebeck response[95]) and phonon scattering. The formation of a surface oxide can change the electronic structure and work function of the Au interface, modify the surface scattering of electrons, and alter the local strain due to surface deformation.

Here we report scanning photovoltage measurements in lithographically defined Au nanowires that are consistent with the optically induced decomposition of a surface layer of AuO_x. Nanowires 10-20 μm in length are exposed to an oxygen plasma, resulting in an increase of their electrical resistance by several percent. A single room temperature scanning steady state photovoltage measurement of a nanowire using a 785 nm diode laser (continuous wave) causes the nanowire to revert to its lower resistance, while yielding a comparatively large "first-scan" photovoltage during the scan. Subsequent scans show as partially varying photothermoelectric response as in previous experiments[73]. Re-exposure to oxygen plasma restores the nanowire to a higher resistance state with an associated largephotovoltage upon initial scanning. On the basis of the systematics, we propose that laser exposure is modifying the nanowire surface by driving decomposition of AuO_x, and thephotovoltage results from the photothermoelectric response of the boundary between Au and Au + AuO_x. Within this picture, the temperature dependence and comparison with known ther-

mal decomposition of AuO_x and the laser-driven temperature increase of the metal show that the optically driven decomposition process is not purely thermal. These experiments demonstrate nanostructure based optoelectronic detection of an optically driven surface chemistry process.

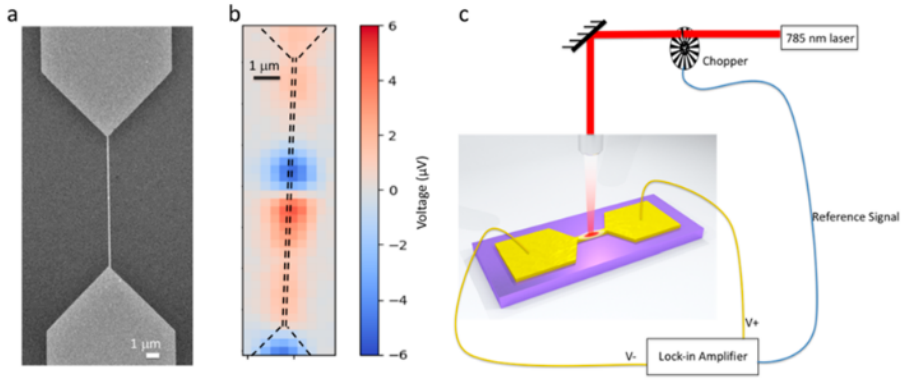

Figure 4.2 : PTE voltage maps in Au nanowires. (a) Scanning electron microscopy (SEM) image of a typical device. Scale bar is 1μm. The width ofthe nanowire is about 130 nm, supporting a transverse local surface plasmon resonance that may be excited by the 785 nm laser polarizedperpendicular to the nanowire. The length of the nanowire is around 10μm. (b) Spatial map of PTE voltage in a typical device. (Black dashed lineindicates the actual device area.) (c) Schematic of the experimental approach for measuring open-circuit photovoltage.

The devices studied in this work were modified gold"bowtie" thin film devices measured in previous works,[3, 67] which consisted of an extended nanowire (10 μm long/120 nm wide,1 nm Ti/14 nm Au thick) between two"fan-out"electrodes on 300 nm SiO2/Si substrates, as shown in Fig4.2 (see detailed fabrication process in Chapter 3.3). Using a home built scanning microscope (See Chapter 3.2.2), a focused 785nm CW laser beam was raster-scanned along the nanowire to serve as a local heating source. Measurements were taken at room temperature and in a high vacuum unless otherwise specified. Similar to previous works,[23, 73] using an optical chopper to modulate the intensity and lock-in detection of the resulting open-circuit photovolt-

age, the open-circuit photovoltage of the entire device was measured as a function of laser position. The photovoltage results from the photothermoelectric (PTE) response of the device as it is locally heated by the beam,enabling spatial PTE voltage mapping. Previous bolometric measurements based on the temperature dependent resistivity of the wires have shown that the maximum nanowire temperature increase under the focused laser spot, when the substrate is at room temperature, is several Kelvin(see Chapter 2.2).[3, 67]

At the nanoscale, the electronic contribution to local Seebeck coefficient can be locally modified by changes in the electron mean free path. When boundary scattering of carriers is significant, changes in sample dimensions can thus act as effective thermocouples. The junction between each end of the nanowire and the fan-out electrodes acts as a single-metal thermocouple due to the differences of Seebeck coefficients at each location[21, 96]; when the laser is incident on those locations, a measurable voltage can be detected.[23, 73] When the laser is positioned in the middle of the nanowire, the temperature distribution and the device geometry are symmetric. Considering only these two factors, no PTE voltage would be expected. However, due to intrinsic material variation within the nanowire, including grain boundaries, local strain variation, etc., variation in the local Seebeck coefficient produces effective thermocouples across the nanowire, resulting in a strong spatial dependence of the PTE magnitude and sign. The spatial pattern of the PTE voltage magnitude and sign as a function of laser position is unique to each device. Previous work[73] discusses the possible mechanisms behind the local Seebeck coefficient variation in more detail. The Mott-Jones equation(see Chapter 1.3.1) shows that the Seebeck coefficient is dependent on the electrical conductivity of the material and, therefore, the electronic mean free path. At the nanoscale, the specific value of the Seebeck coefficient is determined by the

details of the charge carrier transport through the material.[32] Because the metal films are polycrystalline, deposited using evaporation, Scan vary due to dispersity of grain sizes, defects, impurities, crystallographic orientations, and surface scattering. This opens the possibility of modifying the PTE response via surface treatment. Devices were first treated with oxygen plasma to clean the surface to minimize any residual surface contamination from fabrication and immediately placed in the high vacuum cryostation for measurement. An interesting phenomenon was observed from the first scan after O_2 plasma exposure: the first scan's spatial map shows a relatively large PTE voltage along the nanowire of only one sign. Subsequent scans reverted to the previously observed PTE voltage distributions with marked spatial variation and changing sign as shown in Fig4.3a. This procedure could be repeated many times, with a fresh oxygen plasma exposure "reinitializing" the device, the first post plasma scan showing a comparatively uniform, large photovoltage, and subsequent scans showing the sample-specific spatially varying PTE voltage pattern (Fig.4.3b).Below we refer to these as "later-scan" conditions.

The fact that the plasma treatment involves oxygen appears to be crucial. Devices treated with nitrogen plasma in the same plasma cleaner with the same pressure and power conditions did not show the post-O_2-plasma photovoltage effect. Instead,N2-exposed devices had the same PTE spatial pattern as then on-O_2-exposed or later-scan O_2-exposed devices(Fig.4.4). Further, since both plasma treatments kinetically remove surface contamination, the fact that the N_2-and O_2-exposed devices respond differently makes it unlikely that the post-O_2plasma photovoltage results from post cleaning contamination of the surface due to contaminants within the measurement chamber. The measurements are conducted at relatively high vacuum ($10^5 \sim 10^6$Torr). We also note that measurements performed at atmospheric

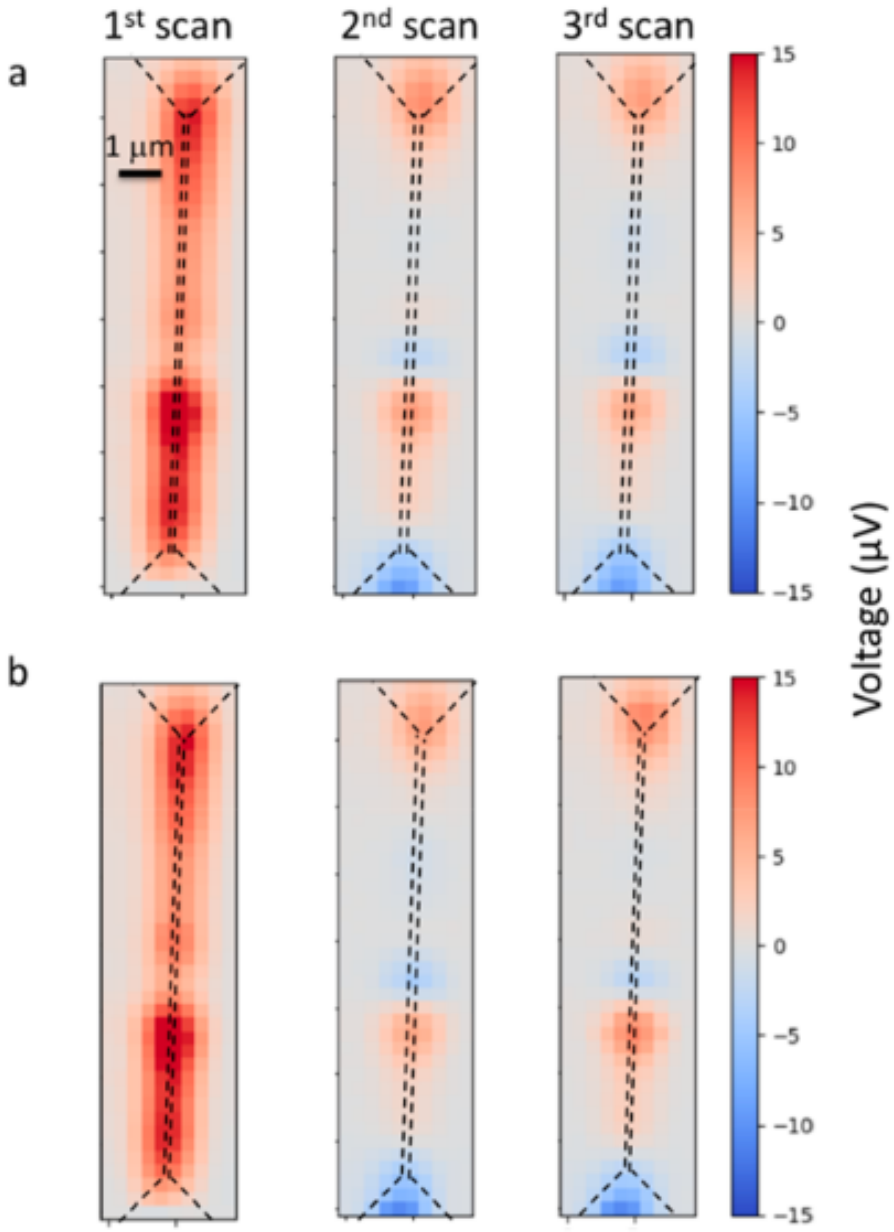

Figure 4.3 : PTE voltage map for the AuO_x device. (a) PTE voltage mapping for the oxygen plasma-treated device (from left to right indicates the scan sequence). (b) Same device showing the reproducibility of the phenomena upon repeated oxygen plasma exposure and subsequent remeasurement.

pressure, when adventitious surface adsorbates should be present, show the same sample-specific PTE spatial pattern as the untreated and later-scan devices.

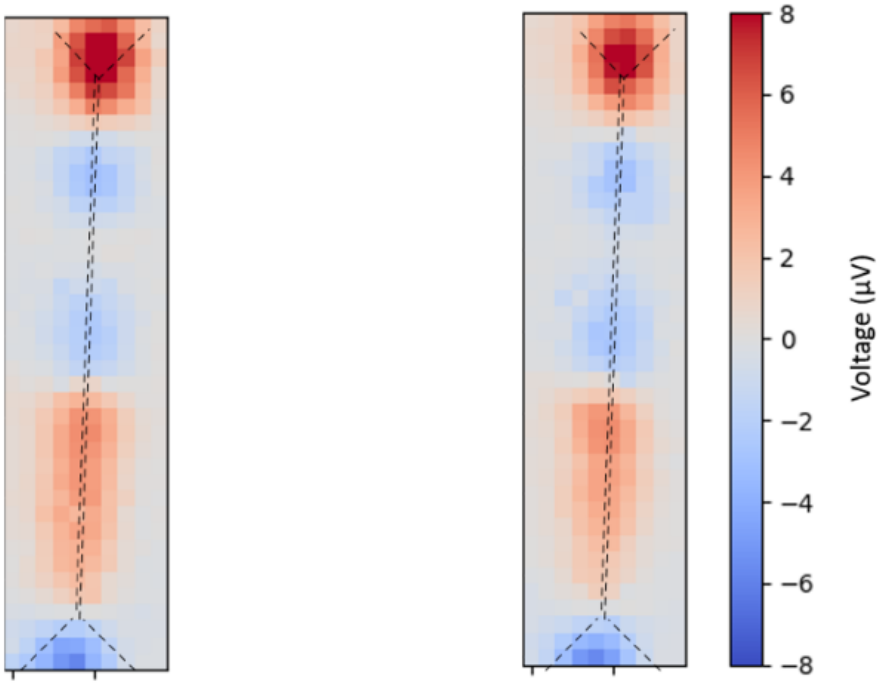

Figure 4.4 : Room temperature PTE voltage map for N_2 plasma cleaned device. Left panel is the result from "non-treated" device. Right panel is the same device immediately after exposure to N_2 plasma.

Metastable gold oxide species can form in a strong oxidation environment such as ozone.[87] Therefore, cleaning the device with oxygen plasma may result in a thin layer of gold oxide (AuO_x) on the surface. Two-terminal resistance measurements were taken before and after plasma cleaning. As reported previously, the room-temperature sheet resistance of the gold nanowire film is around 6Ω. Immediately after oxygen plasma cleaning, the resistance of the nanowire noticeably increases by ∼5%. In contrast, no resistance changeis detected after cleaning with N_2 plasma. After the first scan after O_2 plasma cleaning, the device resistance returns to the original, lower value. These resistance changes suggest the gold surface may have been

oxidized via O_2 plasma. The few-percent resistance change is compatible with the high resistivity of gold oxide[91] and a corresponding reduction in an effective conducting cross section by a few percent and,therefore, an effective reduction in film thickness of $\sim$0.7 nm, comparable to a couple of Au atomic diameters. This is comparable[97] to the thickness of AuO_x previously produced under UV/Ozone.[87] Gold oxide is meta stable and can be completely decomposed at 100°C in 1 h and at room temperature after a few days, respectively[88]. X-ray photo-emission spectroscopy (XPS) shows indications of surface oxidation in a large-area Au film prepared identically to the nanowire devices (Fig.4.5)

To summarize, O_2 plasma exposure increases nanowire resistance, and 785 nm laser exposure restores the nanowire to its initial low-resistance state. Photovoltage measurements during that initial optical scan show a relatively uniform voltage, while subsequent scans show the spatial variation in PTE voltage previously reported. This procedure may be repeated many times. These results suggest a possible mechanism: oxygen treatment creates a thin surface AuO_x layer, and focused laser exposure during the first photovoltage scan decomposes the AuO_x. The measured photovoltage in that first scan in this picture would result from the thermoelectric response of the boundary between the unoxidized Au nanowire and the remaining AuO_x-coated nanowire.

If this hypothesis is correct, then the polarity of the measured first-scan photovoltage should depend on the direction of the laser scan during the photovoltage measurement. The laser heating should always be on the unoxidized Au side of the Au/Au+AuO_x junction, and the orientation of that junction relative to the measurement electrodes depends on the scan direction. Fig. 4.6 shows exactly this result: the first scan's photovoltage polarity changes with scanning direction, whereas subsequent scans remain unaffected.

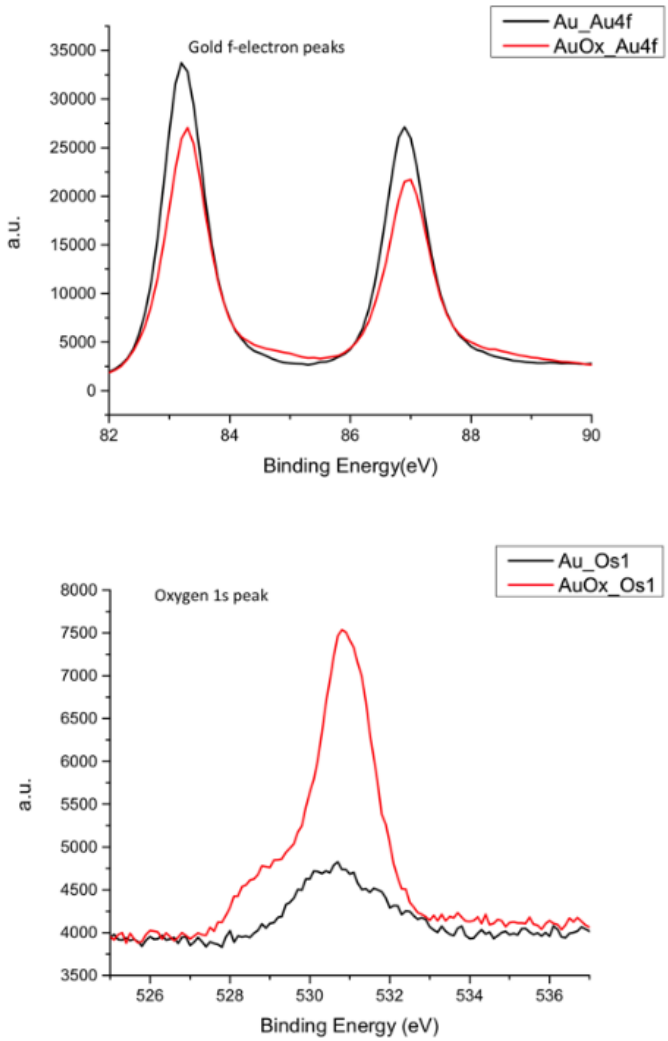

Figure 4.5 : X-ray photo emission spectroscopy of a gold film on an oxidized silicon substrate, before and after oxygen plasma exposure identical to the procedure employed for the nanowire samples. Comparing pre- and post-plasma exposure films, post-plasma we find a clear increase in the oxygen signal, and systematic shifts to higher binding energies for the Au f-electron peaks, as well as the development of a shoulder or weak peak between the large peaks. These signatures are similar to those present in other Au films exposed to oxygen plasma.

Similarly, if the first-scan photovoltage is a PTE voltage generated at the Au/Au $+AuO_x$ boundary, then first-scan illumination in the center of one of the large pads

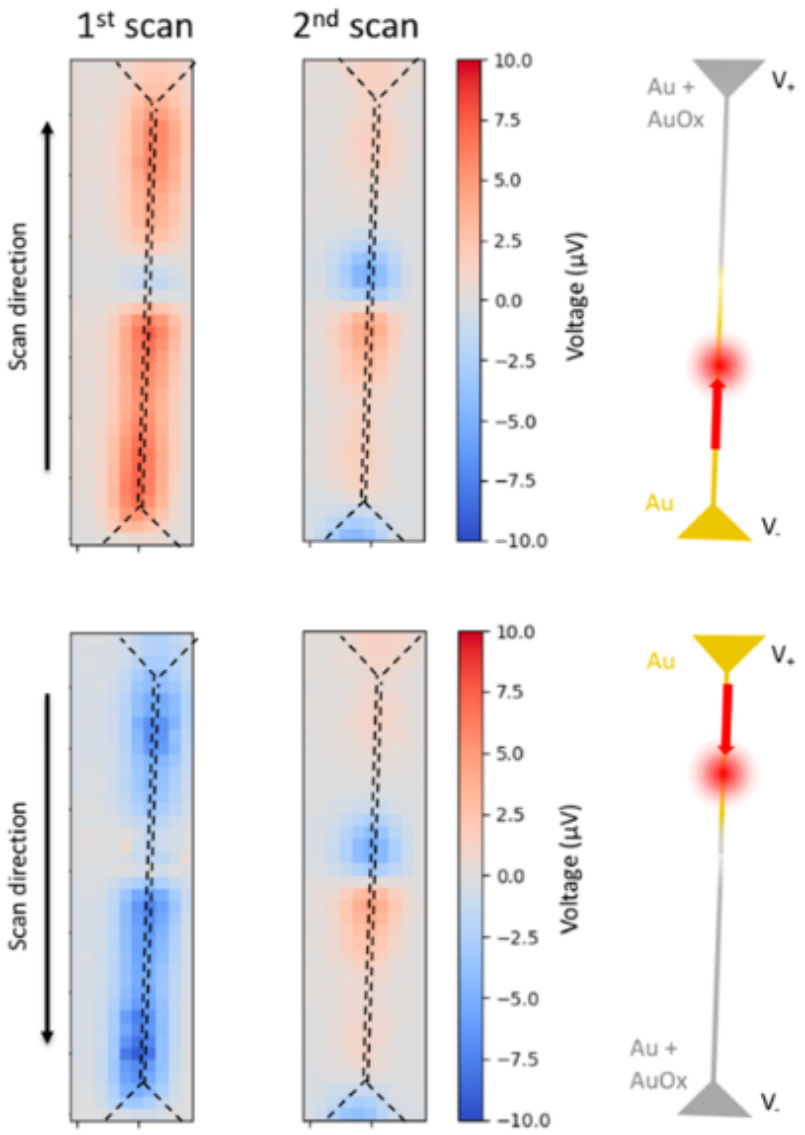

Figure 4.6 : PTE voltage maps for different scan directions. Top row:first- and second-scan mapping for an oxygen plasma treated device while laser scanned from the bottom to top with the bottom electrode defined as ground. Bottom row: PTE voltage mapping for the same device (after retreatment with oxygen plasma) with laser scanning from top to bottom and the bottom electrode defined as ground.Diagrams on the right illustrate how the opposite polarities of first-scan photovoltages can be explained in terms of the reversed symmetry (relative to the voltage leads) of the heating of the Au/Au+AuO_x boundary.

should produce no measurable response because that boundary would be entirely surrounded by metal to short out such a voltage. This, too, is consistent with the measurements, which show no photovoltage response on the big pads away from the nanowire, on the first or subsequent scans.

We also examined the temperature dependence and rate of the light-driven process taking place during the first scan. Each pixel in the photovoltage scans is acquired in 0.3 s. The thermal decomposition kinetics of AuO_x have been studied in detail[88], and temperatures well in excess of 150°C would be needed for purely thermally activated AuO_x decomposition on that time scale. Since local optically driven temperature increases of the metal in this configuration are known at room temperature to be 10 K at the most extreme[3, 67], some nonthermal mechanism must be at work in the optically driven surface modification, or the kinetics of AuO_x decomposition would have to be considerably more rapid for very thin oxide layers. The persistence of the first-scan effects in samples that have spent hours at room temperature argues against that latter possibility.

One possibility to consider is a process driven by photo-produced hot electrons.[98, 99] Due to the device geometry,the gold nanowire has a strong local surface plasmon resonance under illumination of the 785nm wavelength laser in the transverse polarization (along the short axis of the nanowire[3, 66]), and plasmon excitation is one means of hot carrier generation, in addition to ordinary optical absorption. If hot carrier generation is the sole mechanism for the optically driven surface chemistry at work here, the first-scan photo-voltage and resistivity reduction should also be observed at low substrate temperatures. We find that at temperatures below 270 K, there is neither a first-scan photovoltage effect nor an optically driven change in device resistance. After warming the devices previously scanned at lower temperatures,

both effects are seen in the first optical scan taken above 270 K. These results from low temperatures indicate that the dominant mechanism for the surface modification is not purely based on photo excited hot carriers and that another mechanism must come into play. Fig.4.7 shows the results of additional experiments performed at room temperature to understand the process at work here. After oxygen plasma exposure, the laser is focused on the middle of the nano wire while measuring the PTE voltage. As shown in Fig.4.7, the magnitude of the PTE voltage dropped dramatically in the first few seconds and slowly dropped to a stable value after about 300s. Subsequent scans show a PTE voltage pattern typical of a later-scan normal device, and the device resistance has returned to its lower value. These results indicate that the likely AuO_x has decomposed across the whole nanowire after a certain time even though the laser is only focused on the middle of the nanowire. Considering that the spot size (1.8μm) of the laser is much smaller than the nanowire (10μm), the rapid decrease in PTE voltage magnitude could be due to gold oxide decomposition within the laser spot area. The subsequent slow decrease of PTE voltage magnitude may then be due to the gold oxide decomposition on the rest of nanowire not directly heated by the laser.

4.3 Conclusion

From the above results, the apparent AuO_x decompositionon the nanowire is strongly and abruptly inhibited at lower temperatures and can be triggered by focusing the laser on only a fraction of the nanowire. While it is speculative at this point,it is important to consider that residual gases could play some role, despite the relatively high chamber vacuum. When the system temperature is decreased, residual gases condense on the coldest portions of the chamber. This may explain the compar-

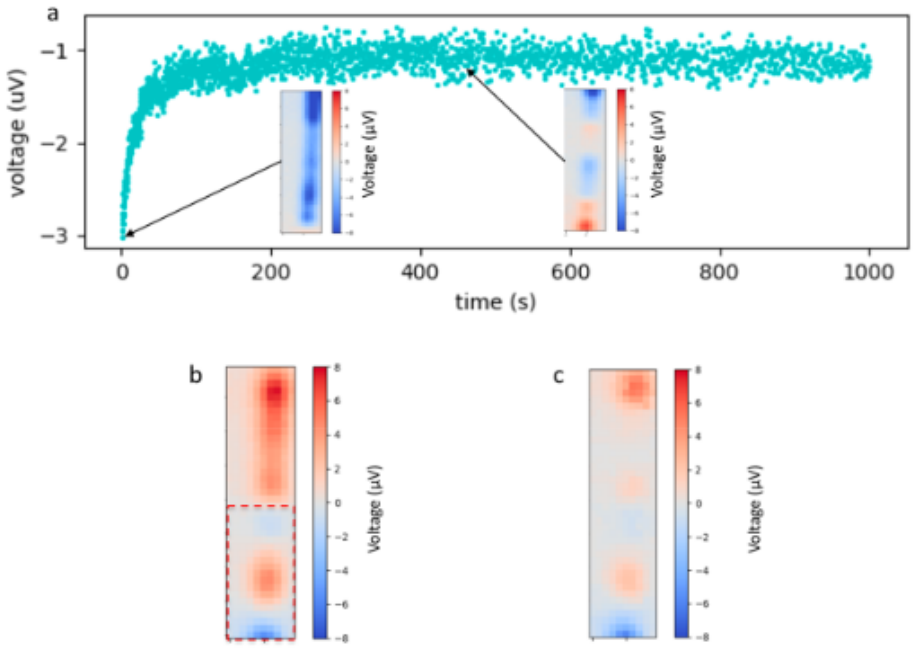

Figure 4.7 : Top panel shows PTE voltage vs time by the focusing laser at a fixed position. Insets indicate the PTE mapping of a freshly oxygen plasma-treated device (left) and a scan after focusing the laser on the device center for several minutes. (b) PTE voltage map of an AuO_x device with the bottom half previously scanned by the laser. (Red dashes line indicates the scanned area.) (c) PTE voltage map of the device after acquiring the scan in panel b.

atively sudden suppression of the light-driven decom-position with decreasing temperatures. The present chamber configuration makes in situ monitoring of residual gas composition impractical, so experiments testing for this issue will require further developments. Next steps to better understand the mechanism at work here include examining the spectroscopic dependence of the photovoltage/resistance changes on the incident wavelength and in situ monitoring of residual gas composition within the chamber, both of which are quite technically challenging.

Photovoltage mapping of gold nanostructures has revealed alight-driven photovoltage response and reduction in electrical resistance in nanowires previously im-

mediately exposed to an oxygen plasma environment. These effects can be observed repeatedly if the devices are again subjected to oxygen plasma,strongly suggesting that metastable AuO_x and its light-driven decomposition are responsible. The systematic imply that the photovoltage originates from PTE response of the boundary between Au and Au+AuO_x. The observed temperature dependence and time scale for a light-driven surface modification, combined with the known kinetics for AuO_x decomposition, show that the decomposition here is not purely photothermal and may result from catalytic processes involving residual gases within the measurement system. While raising questions about detailed mechanisms beyond the scope of the present study, these experiments demonstrate the optoelectronic detection of a light-driven surface chemical process in individual nanostructures.

Chapter 5

Tuning photothermoelectric response in gold nanostructures: strain and surface modification

The surprising local variation in the Seebeck coefficient in polycrystalline nanowires of uniform width and thickness was discussed in Chapter 2 and Chapter 4. In this chapter, we will discuss the possible candidates for this local variation: local grain boundary condition; surface work function and the strain distributed along the nanowire. After a extensively research effort, we found out that strain is the dominate mechanism to cause this effect. The first mapping scan of the photothermoelectric voltage shows a relative high value compare with the second scan on the same device after 14 hours annealing. We also conduct a control experiment to shift the work function of the gold nanowire via self-assembled monolayer. Combining the Kelvin probe measurement with the photothermoelectric voltage shows the work function variation of the nanowire doesn't play a key role on the photothermoelectric voltage response. A separate research project[4] also rules out that the grain boundary is not the dominate mechanism to cause this phenomenon. These experiments argue that the strain distribution within the gold nanowire is likely the dominant effect causing the variation of the photothermoelectric voltage. Photothermoelectric voltage measurement provides a sensitive new method to strain distributions within a nanostructured metal.

5.1 Grain boundaries and Seebeck coeffient

As previous chapters discussed, from PTE measurements we found that the local variation in the Seebeck coefficient along the nominally uniform nanowire. The first thought is that the grain boundaries could be the mechanism cause this local variation. Since the device is fabricated via evaporation, a polycrystalline nanowire will obtained after the evaporation. One simple method to re-orientated the grain boundary condition is through annealing.[100] Comparing the PTE voltage pattern before and after annealing could probe the dependence of the pattern to the local grain structure.[73] Fig.5.1a shows a 5μm long device prior to annealing. The device was annealed by running a current through the nanowire while monitoring the resistance to avoid electromigration. Fig. 5.1b shows the PTE mapping after the current annealing, the magnitude of the PTE signal was reduced by roughly a factor of 5. To further confirm this result, another device was measured by annealing on a hotplate. Fig. 5.1c and Fig. 5.1d shows a 10 μm long device before annealing, and after annealing on a hotplate at 200 °C for 3 hours under an Ar atmosphere. Once again, the variation in the photovoltage response changed. The magnitude of the signal along the nanowire decreases and overall pattern of the spatial variation changes. The change of pattern and magnitude and the chemically inert properties of Au indicate that the variation in photovoltage is very likely sensitive to the crystalline structure of the device.

However, a later study[4] shows the grain structure have does not have a significant effect on the local Seebeck coefficient. To study the effect of the grain boundary. A bicrystal gold stripes can elucidate the importance of grain structure of the Seebeck coefficient. We obtained the bicrystal gold stripes sample[101] from Prof. Fan's group at Stanford University.

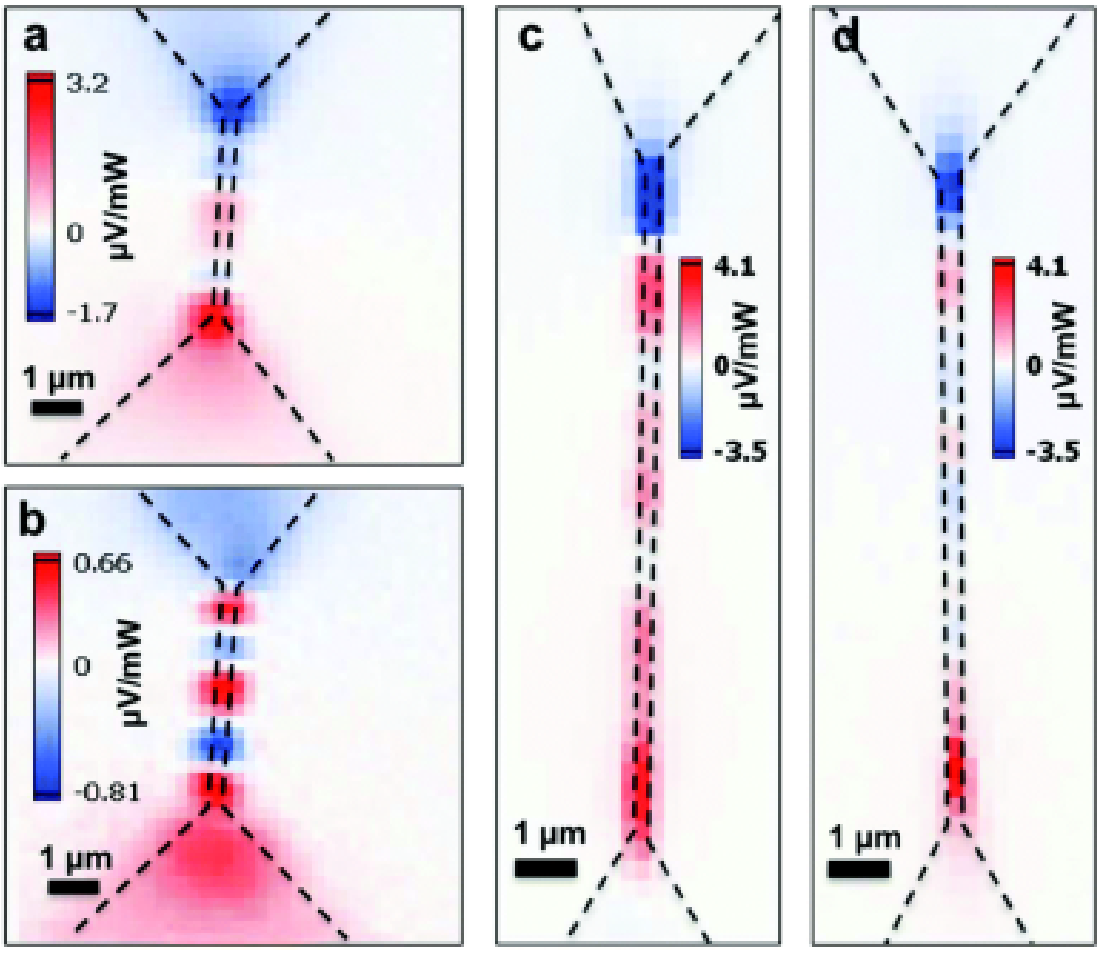

Figure 5.1 : Photothermoelectric measurements of extended gold bowtie devices before and after annealing a: 2D PTE map of a bowtie device with a 5μm long nanowire before annealing. b: PTE map of the same device in a after current annealing. c: PTE map of a bowtie device with a 10μm long nanowire before annealing. d: PTE map of the same device in d after annealing at 200 °C for 3 hours in Ar. From ref.[73]

A bicrystal device is shown in Fig.5.2a, the SEM image is relatively featureless and uniform along the device with a change of contrast indicates the grain boundary where two single grains contact. Fig.5.2b shows the electron backscatter diffraction(EBSD) and reference orientation deviation(ROD) measurements around the grain boundary marked by the red box in Fig.5.2a. The z-axis is in the $< 111 >$ crystallographic

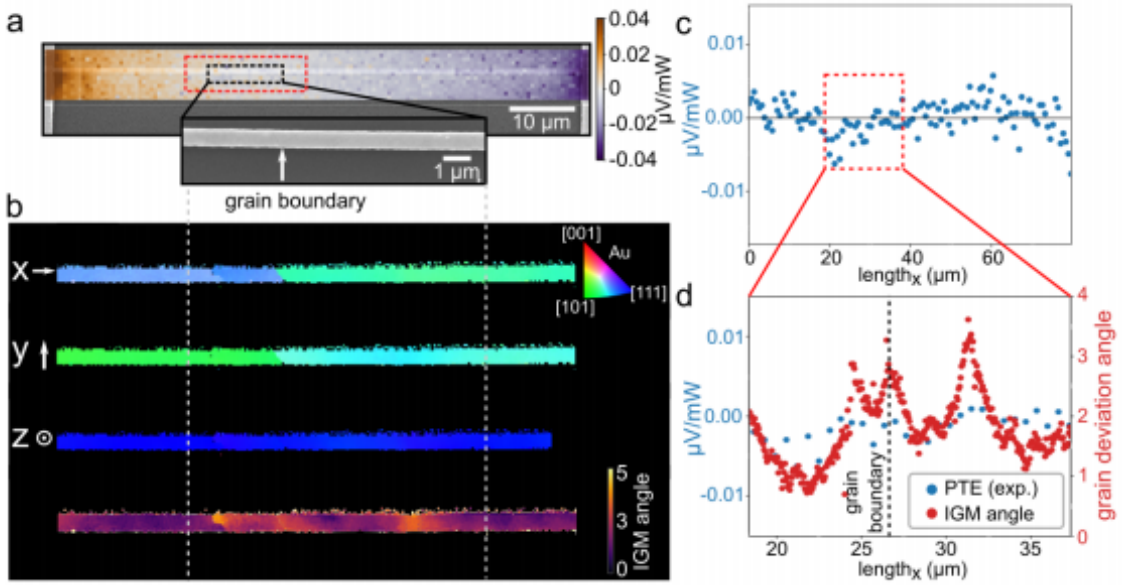

Figure 5.2 : PTE map of a bicystal gold stripe device. inset: Zoomed-in image of the black dashed box highlighting the individual grain boundary. b: EBSD and ROD map of the device in the red box in a. The scale bar is shared with the inset of a. c: Scatter plot of the local maximum PTE Voltage along the length of the device. d: Comparison of the PTE Voltage and misorientation angles within the red dashed box in c. From ref.[4]

orientation. However, the x and y axes have their own orientation for each grain demonstrating a well-behaved grain boundary. The bicrystal device was annealed at 300 °C prior to measurement to reduce the local variation in strain along the length of the device. The PTE map and scatter plots, Fig.5.2a,c, are fluctuating near zero value along the length of the device. There is no significant PTE signal when the grain boundary is heated. The comparison of the PTE and ROD measurements around the grain boundary is seen in Fig.5.2d. Although there is considerable misorientation across the grain boundary, the PTE signal does not change at the grain boundary.

5.2 Strain and Seebeck coefficient

Now we can discuss the results from the previous sections. The bicrystal gold stripe PTE map combined with the EBSD shows the grain boundary is not playing a key role in the local Seebeck coefficient, it is almost featureless along the bicrystal gold stripe even at the grain boundary. If we also consider the result from section 5.1, the overall PTE signal reduced along the nanowire after the annealing. An obvious possible candidate pops up for this variation: that is the strain within the nanowire. When we fabricate the device, it is lithographically designed and evaporated. Because of the constrains on the design, it will introduce strain when we evaporate the gold onto the substrate. Annealing is the most common method to reduce the strain in the metal. However, the only concern in the earlier study is that we may slightly changed the local grain structure during the annealing since we are using relatively high temperature for gold nanowire. This time, we are using a low temperature(100°C) for 14 hours under an Ar atmosphere in a tube furnace to avoid this potential issue. The result shows in the Fig.5.3, the overall PTE signal significantly reduced after annealing. Which agree with the previous result and match with the result from ref.[102, 103] for a bulk metal Seebeck coefficient under changing with strain. A statistical analysis of 20 devices is presented in the Fig.5.4.

A statistical analysis of 20 devices is presented in the Fig.5.4. On the left panel, the average OCV across the nanowire with the same devices measured before annealing(blue) and after annealing(orange). The result indicates the overall magnitude of the OCV is dropped by one order. the right panel shows the coefficient variation distribution if the devices, which is a normalized standard derivation by the mean value, which could indicates the OCV fluctuation along the nanowires.

Moreover, we further studied the strain effect on the PTE response. This time,

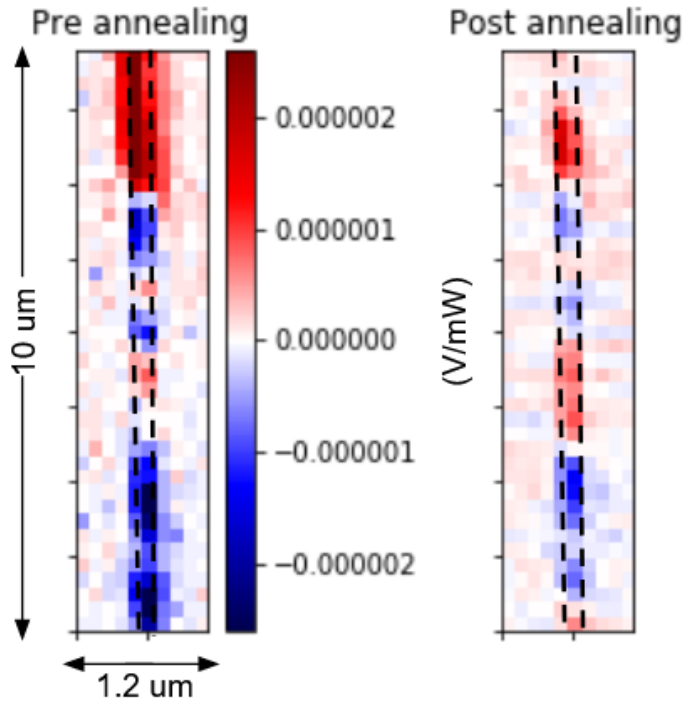

Figure 5.3 : PTE map of a 10μm long polycrystal gold nanowire before annealing(left) and after annealing at 100 °C for 14 hours in Ar.

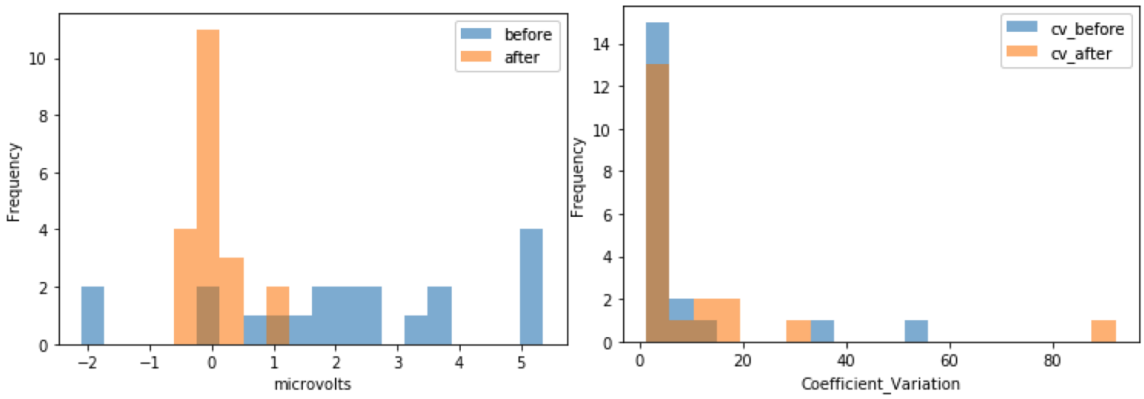

Figure 5.4 : Statistic analysis on as fabricated(blue) and after annealing(orange): left panel is the average measured OCV along the same device before and after annealing. Right panel shows the coefficient variation of each device, which can indicates the outliners in the count.

we deposited 2 nm Cr on half of the device to induce strain to the device. When Cr is exposed to oxygen, it will be oxidized and expended with the oxide form which could add extra strain to the device.[104] As shows in the Fig.5.5., the PTE signal is much higher after the deposition and not only the half with Cr but the overall PTE response along the nanowire is increased dramatically by over 10 times. The green box indicates the Cr covered side and the red dot in the middle possible caused by the Cr/Au interface.

5.3 Work function and photothermoelectric effect

Before we draw the conclusion that strain is completely at work here, we would like to study if other possible mechanisms could possibly contribute to altering the photothermoelectric effect. One natural candidate is the work function. In thin films, the bulk electron mean free path can be comparable to the film thickness, resulting in surface scattering and therefore reducing the electron mean free path on the order of the film thickness. The electronic component of the Seebeck coefficient described is determined by the energy dependence of the electrical conductance, which is a function of the electron mean free path and the Fermi surface (band dispersion). As such, surface conditions can have an effect of the thermoelectric properties of the material.

It has been shown that the work function of metals can be altered by the self-assembly of polar molecular monolayers.[105, 106, 107] To study the effect on modification of the surface work function, we designed the following experiment: First, we took an annealed 10μm long polycrystal gold nanowire with PTE measurement already completed. Then, we spin coated the PMMA(950) on the device and opened a window on the half of the nanowire. Then the device was immersed in a 1-

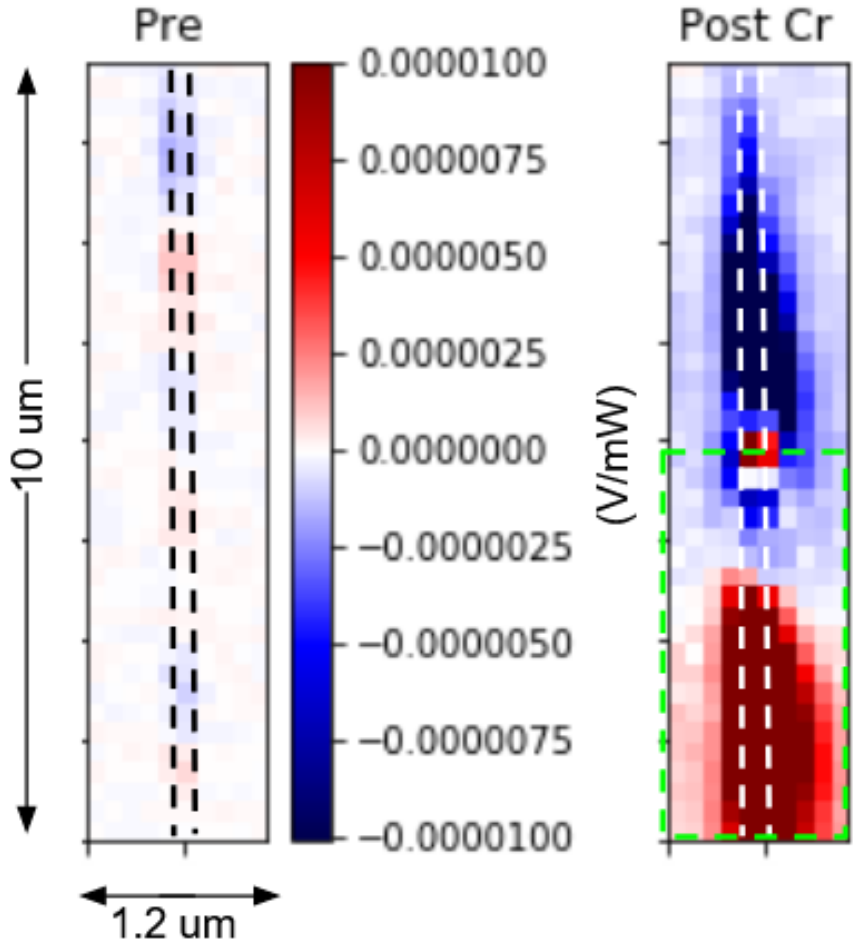

Figure 5.5 : PTE map of a 10μm long polycrystal gold nanowire before Cr deposition (left) and after Cr deposition(right). the green box indicates the Cr covered area.

octanethiol/ethanol solution to allow the octanethiol to form SAM. Then the device is measured with PTE and KPFM to study the effect of work function on the PTE response. It has been demonstrated that SAM from thiol on gold surface can effectively shift the effective work function of gold by (-0.6 $\sim$ -1 eV)[108, 109]. In Fig.5.6, on the left is the work function map of the device via Kelvin probe, It clear shows

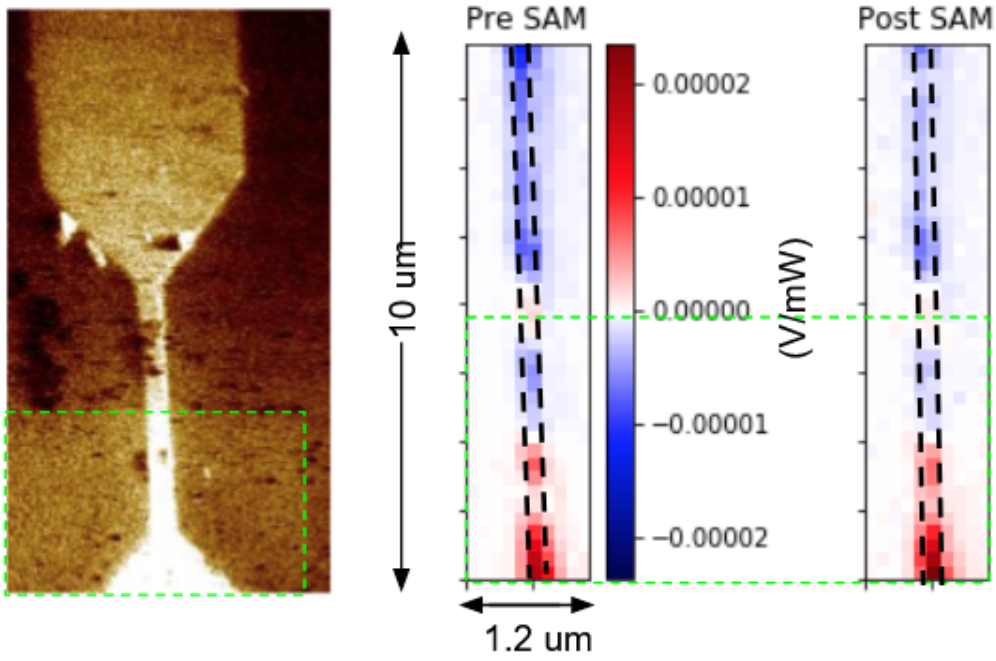

Figure 5.6 : Left: work function map of the device via Kelvin probe.(a -0.6eV drop from the top to bottom area) The green box region is the area covered with SAM which has a lower work function. Right: PTE map of the device before and after put down SAM, there is no obvious changes in the PTE response.

the work function of gold shifted by the SAM which has a light color on the red box region(with SAM covered) which has a low effective work function. The difference on the pristine gold and the area covered with SAM is ~ 0.6 eV, which is a significant change. However, on the right PTE maps indicate the PTE almost kept same before and after put down the SAM on the device. The result indicates, the work function of the gold is not playing a key role in the PTE response. In total, we measured 12 devices, all the devices show a drop on the work function($0.4 \sim 0.6$ eV) but the PTE map remain the same.

5.4 Conclusion

In this chapter, we discussed the observation of the local variation on the PTE voltage along the nanowire. A variety of possible mechanisms are proposed to cause this effect. Based on the above experiments result, we can rule out that the grain boundaries themselves are not contributing much to this effect, nor do modifications of the work function of gold. The strain distribution along the nanowire is the dominant effect that cause this local variation on the PTE voltage. Therefore, not only the local geometry change can affect the local Seebeck coefficient but also the strain distribution can change the the local Seebeck coefficient. That might give a new approach for fabricate single metal thermocouples or to engineer novel thermoelectric structures.

Chapter 6

Nanogap assisted Raman enhancement on monolayer MoS_2 photothermoeletric effects

A self aligned gold bowtie structure with nanogap is fabricated on top of a CVD grown monolayer MoS_2 flake. With the assistance of the nanogap and the polarization of the incident laser, the Raman signal of monolayer MoS_2 is enhanced and observed with a low intensity incident laser. Moreover, a enhanced photovoltage result from the photothermoelectric response of this nanogap induced local field enhancement combined with the conductivity of MoS_2 provides additional information on the plasmonic property of this device.

6.1 Motivation and background

This chapter will present a study on Raman enhancement of monolayer 2D material MoS_2 and it's photothermoeletric effects. the purpose of this work to combine both optical and electronic measurements on the two dimensional materials(e.g. MoS_2, $MoSe_2$). Two dimensional (2D) semiconductors are drawing much interest as possible candidates for flexible electronics system.[110, 111, 112] MoS_2 (Molybdenum disulfide) is a prototypical 2D semiconducting transition metal dichalcogenide (TMD) and has been most extensively studied.[110, 113, 114, 115, 116] Monolayer MoS_2 is composed of two S layers and one Mo layer arranged in hexagonal lattices. These layers are covalently bonded to one another and form a "trilayer" (TL). Thicker MoS_2 is formed by stacking such TLs through weak van der Waals interaction. Monolayer (1TL) MoS_2

has a direct bandgap whereas thicker MoS_2 has an indirect gap.[110, 113, 114] The studies on the optical properties of MoS_2 have yielded many interesting results.[117, 118, 119] Strong photoluminescence (PL) has been observed for few-layer MoS_2.[116] Whereas 1TL MoS_2 shows a strong PL signal due to the direct bandgap[120, 121], the PL signal due to the indirect bandgap in thicker MoS_2 can be used to estimate the thickness as the peak position depends on the number of layers. In this work, we combined the bias V and the Raman spectroscopy of MoS_2 together to observe the effect of charge carriers on the Raman-active vibrational levels.

6.2 Experimental method

The CVD grown monolayer MoS_2 is obtained from Prof.Ajayan's group. As shown in Fig.6.1, there are several MoS_2 flakes on the SiO_2 wafer. One major advantage of this CVD grown MoS_2 is the size and the number of of the flakes is large which allow us to fabricate several devices on a single wafer. However the trade off is the overall quality of the material. Typical CVD grown materials contains lot defects which will downgrade the quality of the material. In this study, the CVD grown MoS_2 is the best option due to the difficulty and the low success rate of the self align nanogap structure.

The as grown MoS_2 was transferred to a clean new wafer to avoid the potential leakage and the rough surface of the SiO_2 due to the CVD process. Then with the assistance of the cross marks on the wafer, a set of the self aligned(see Chapter 2.3 for detail of this method) gold bowties are fabricated on the MoS_2 flakes as shown in Fig 6.1. The reason for using the self align technique is due to the conductivity of MoS_2, so the electron migration technique cannot readily be applied here. Large gold contact pads are then deposited for connecting to measurement system. As

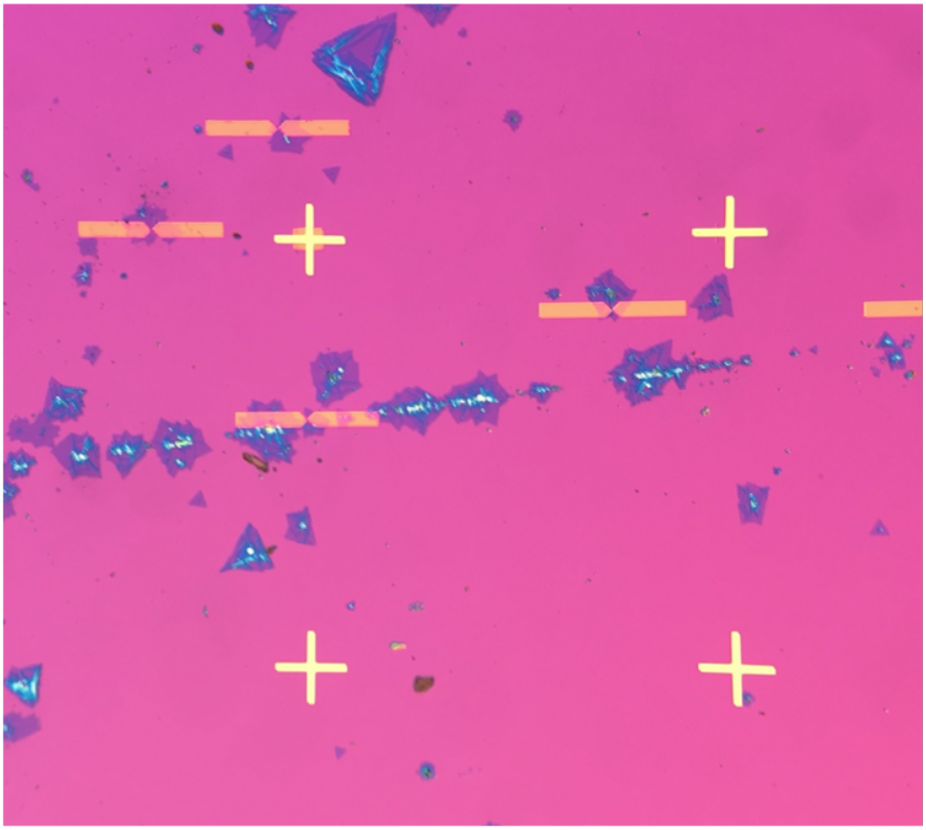

Figure 6.1 : Image of CVD grown MoS_2 on SiO_2 with gold bowtie fabricated via "self-align" method(see 2.3). The purple color triangle like item is the CVD grown MoS_2 typically has a thick core(blue color) in the center and monolyer MoS_2 is grown around the core. Gold bowtie is putted down on the monolayer MoS_2 area.

prepared sample wafer is then bonded with the sample holder socket via wire bonder. The home built Raman spectroscopy system(see Chapter 3.2.2 for details) is used to perform the measurement. As shown in Fig. 6.2, a 785nm continues wave laser is polarized via a half wavelength plate and chopped via a optical chopper(provide reference frequency for lock-in amplifier). Finally the laser is focused via objective on to our device. The position of the laser spot on the sample can be adjusted via a piezo controller to maximize the output signal. The Raman signal is read via our home built Raman spectroscopy and the conductance measurement is done by the

lock-in amplifier.

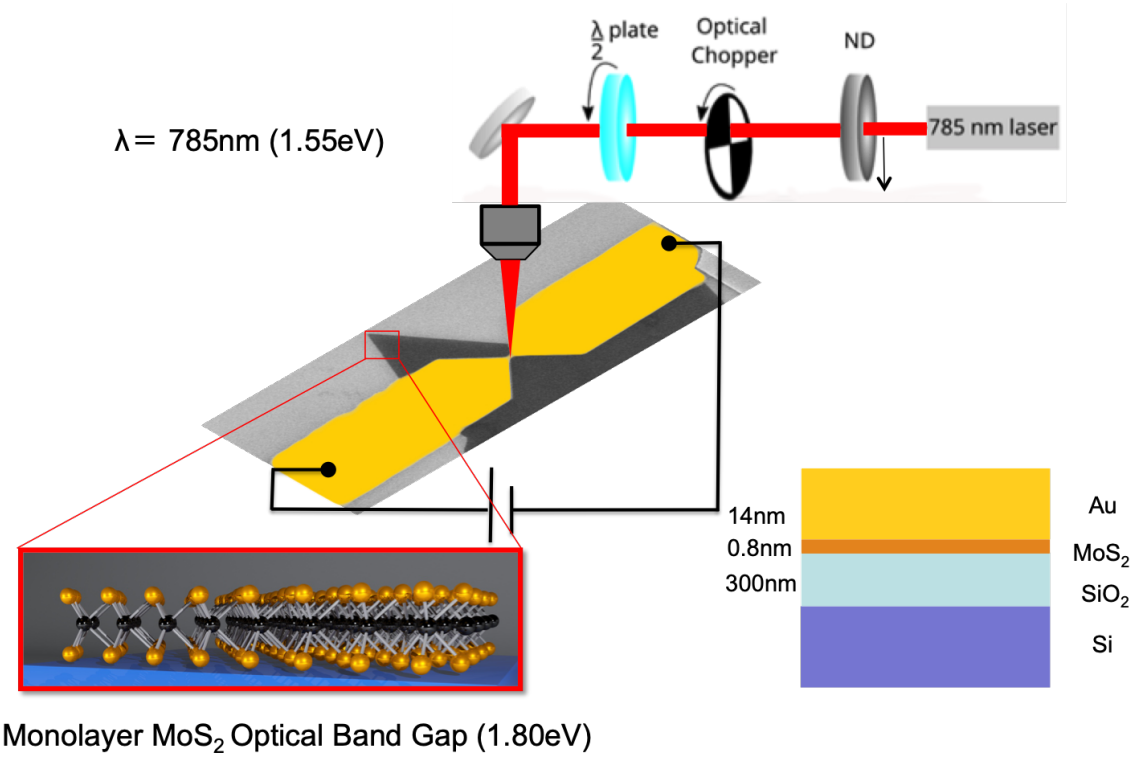

Figure 6.2 : Schematic of the measurement process and the cross section view of the device. A CW 785nm laser passes through a set of mirrors and lenses. The laser is polarized by a half-wave plate and focused by an objective on to our device. The cross section view of the device indicates the thickness of each layer for the sample.

6.3 Raman spectrum of the MoS_2

The Raman Spectrum of MoS_2 at the nano gap area is presented in Fig.6.3. The top SEM images show the detail of the nanogap area. On the top left image, we can see the gold bowtie is on the monolayer MoS_2(the black area in the image) and the zoomed nanogap($5 \sim 10$nm) is shown in the top right image(the length of the nanowire is $\sim$ 800nm and the width is $\sim$ 120 nm). The bottom two spectra are taken with different polarization of the incident laser. It is clear to see that the MoS_2 Raman

peaks only appear when the laser is polarized at transverse direction of the nanowire and are not detectable when laser is polarized at longitudinal direction. The reasons for this phenomena are: 1.the scanned area is very small, most laser is focused on the gold , only a fraction of the laser incident directly on MoS_2 2.The overall intensity of the laser is low($\sim$ 10mW) compare with commercial Raman spectroscopy. As a result(Fig.6.3 bottom right), the overall Raman signal from the nanogap is almost undetectable without any local field enhancement. 3.the field enhancement is highly localized in z axis, means mainly within the gap, but MoS_2 is sitting below the nanogap. 4. the gold "bowtie" on top of the MoS_2 introduce extra strain to the MoS_2 which could weak the overall vibration of the flake.

In the bottom left Raman spectrum, we can see the background of the spectrum is curved, which is due to the doping in the SiO_2 substrate. It is confirmed by using a fresh SiO_2 substrate from the same wafer. The strong peak $\sim$ 520 cm^{-1} represent the silicon line. The peak at 385 cm^{-1} represents the E_2g Mode[122, 123] (in plane stretching model) in MoS_2, and the peak at 410 cm^{-1} indicates the A_1g Mode[122, 123] (out plane stretching model) in MoS_2, respectively.

6.4 Photo current and the photothermoelectric effect

A photo current(I_{photo}) plot for this device as shown in Fig.6.4. This I_{photo} plot shows the I_{photo} measured at different polarization degree of the incident laser. As we discussed in Chapter 2, the resonant transverse plasmon mode of this typical gold "bowtie" structure can be excited by the polarized 785nm laser. The result shows a very strong polarization dependence of the incident laser, the max I_{photo} occurs at the 0/180° which is $\sim$ 5 times at 90/270°. It mainly contributed by the hot electrons generated by the transverse plasmon mode.

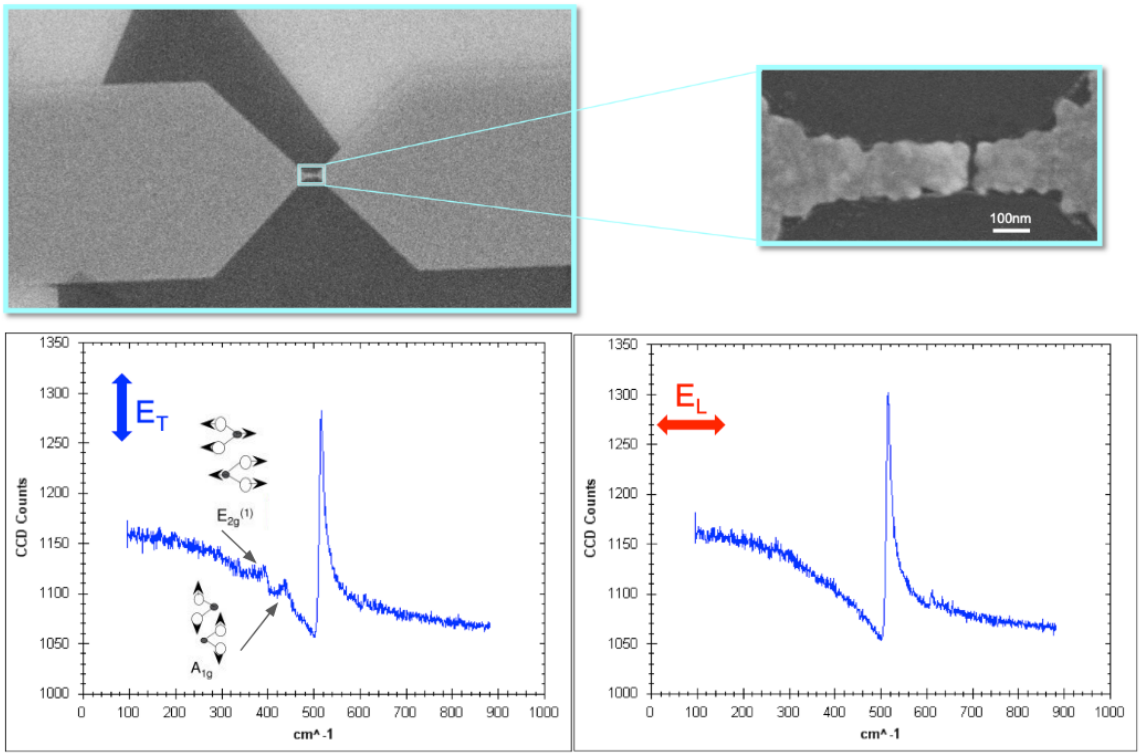

Figure 6.3 : SEM image and Raman spectrum of Monolayer MoS_2 at different polarization degree. Top panels are the SEM images of the MoS_2 "bowtie" device. The bottom panels are Raman spectrum of Monolayer MoS_2 at different polarization degree(left: polarized at transverse direction; right: polarized at longitudinal direction)

A photothermoelectric voltage measurement is also performed on this device, as shown in Fig.6.5. The device with MoS_2(left) has about 2 times max response on the photothermoelectric voltage($\sim$ 5.4mV/mW) compared with the device without MoS_2 ($\sim$ 2.8mV/mW)[124] and about 5 times compared with regular gold pads with MoS_2($\sim$ 1mV/mW)[125]. The result indicates both MoS_2 and hot electrons generated via the excitation of local plasmon mode contribute to the photothermoelectric response.

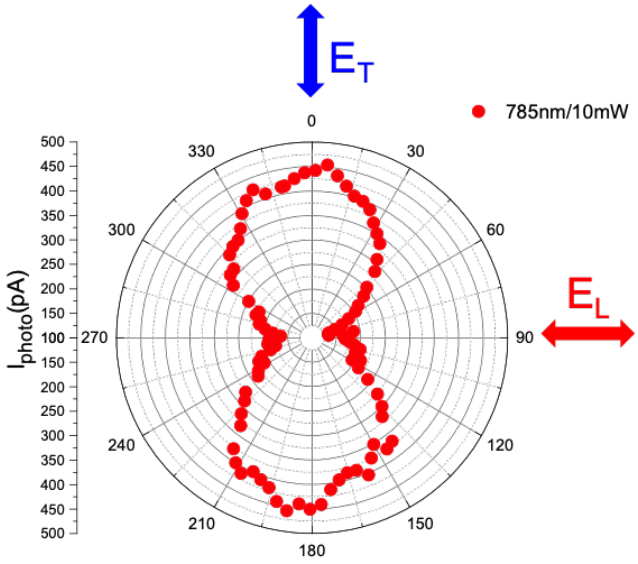

Figure 6.4 : Polar plot of the incident laser polarization dependence of the nanowire photo current (I_{photo}). I_{photo} has the largest magnitude when the laser is in the transverse (180 °) polarization due to the excitation of the resonant transverse plasmonmode.

6.5 Conclusion

Based on the Raman spectrum of the MoS_2/nanogap structure, a enhanced Raman signal of MoS_2 has been observed. However, due to the nature properties of the local field, it is highly localized within the gap. This spatial separation (in z) between the maximum field enhancement at the underlying substrate imply that such nanogap structures are not well-suited to enhanced Raman studies of 2D materials. A photothermoelectric voltage map indicates the MoS_2 will contribute to the total response due to the hot electrons generated from the nangap can travel through the underneath MoS_2 but not with SiO_2.

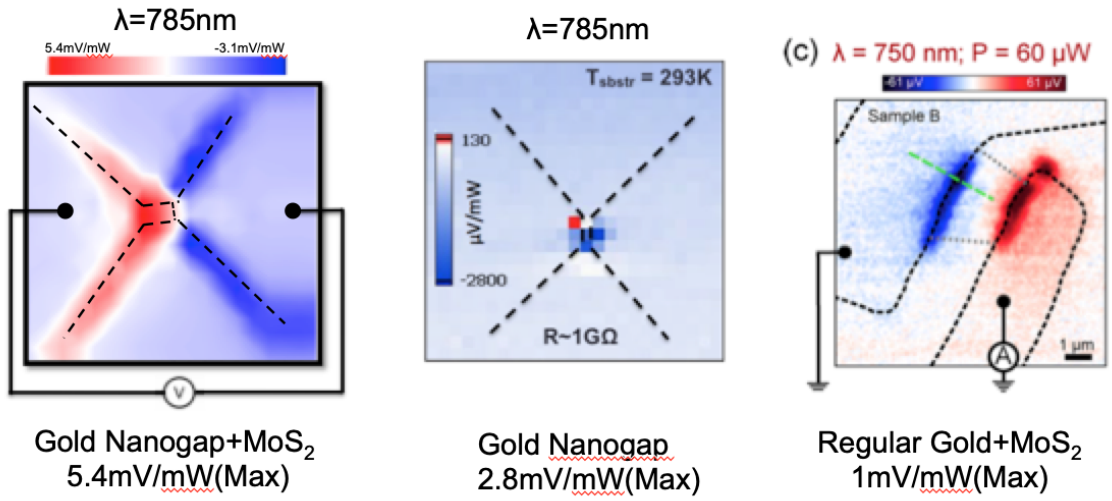

Figure 6.5 : photothermoelectric voltage measurement on three different devices.From left to right, gold bowtie with nanogap with monolayer MoS_2; gold bowtie with nanogap[124]; and regular gold pad with few layer MoS_2[125]

Appendix A

Analysis Code

map_plot&stat_analysis

August 13, 2020

[3]:
```
import matplotlib.pyplot as plt
import pandas as pd
import numpy as np
%matplotlib inline
from matplotlib import cm
from os import listdir
from os.path import isfile, join
```

Now First to remove the headlines in the file

[18]:
```
file = '/Users/xifanwang/Desktop/experiment_data/aft_aneal/1-2_x_0.csv'
with open(file , 'rb') as infile:
    data_in = infile.readlines()
with open (file, 'wb') as outfile:
    outfile.writelines(data_in[14:])
direc = '/Users/xifanwang/Desktop/experiment_data/pte/'
onlyfiles = [f for f in listdir(direc) if isfile(join(direc, f))]
list_new = []
for i in onlyfiles:
    if 'csv' in i:
        list_new.append(i)
list_new = []
for i in onlyfiles:
    if 'csv' in i:
        list_new.append(i)
for i in list_new:
    if '_cut' in i:
        del i
```

Load Data

[11]:
```
after = pd.read_csv('/Users/xifanwang/Desktop/after.csv')
```

[12]:
```
before = pd.read_csv('/Users/xifanwang/Desktop/before.csv')
```

[3]:
```
file = '/Users/xifanwang/Desktop/experiment_data/pte/1-1_x_0_cut.csv'
```

Statistic Analysis

[137]:
```
Mean = pd.DataFrame()
Coefficient_Variation = pd.DataFrame()
```

[138]:
```
Coefficient_Variation['cv_before'] = abs((before*(10**6)).std()/
↪(before*(10**6)).mean())
```

[139]:
```
Coefficient_Variation['cv_after'] = abs((after*(10**6)).std()/(after*(10**6)).
↪mean())
```

[118]:
```
stat['before'] = before.mean()*(10**6)
```

[119]:
```
stat['after'] = after.mean()*(10**6)
```

[134]:
```
ax = stat.plot.hist(bins = 20,alpha = 0.5)
ax.set_xlabel('microvolts')
```

[134]:
```
Text(0.5, 0, 'microvolts')
```

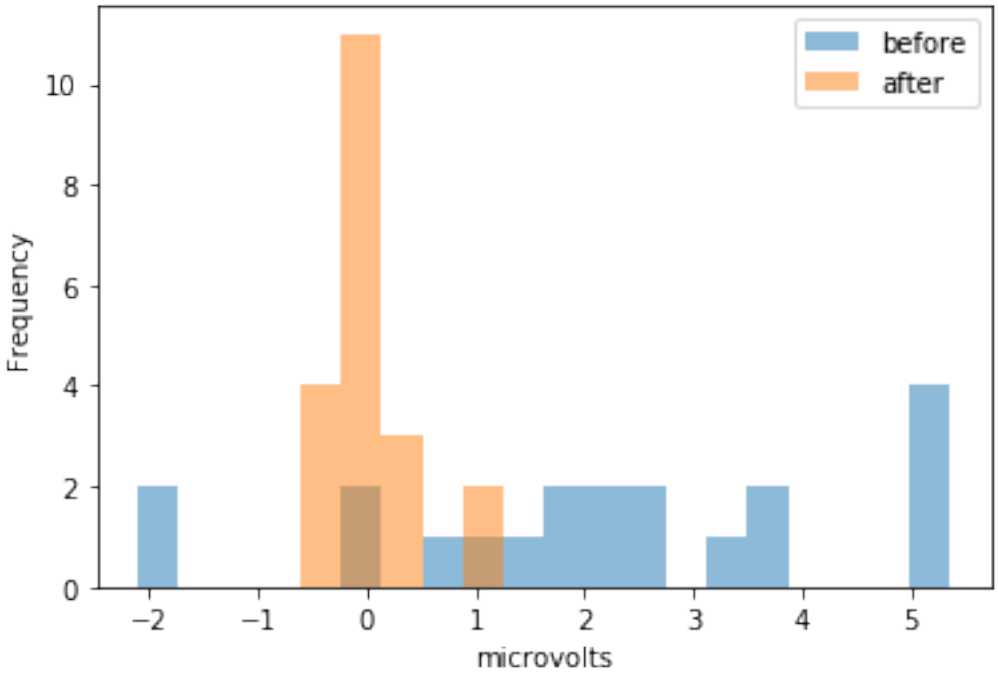

[140]:
```
ax1 = Coefficient_Variation.plot.hist(bins = 20,alpha = 0.5)
ax1.set_xlabel('Coefficient_Variation')
```

[140]:
```
Text(0.5, 0, 'Coefficient_Variation')
```

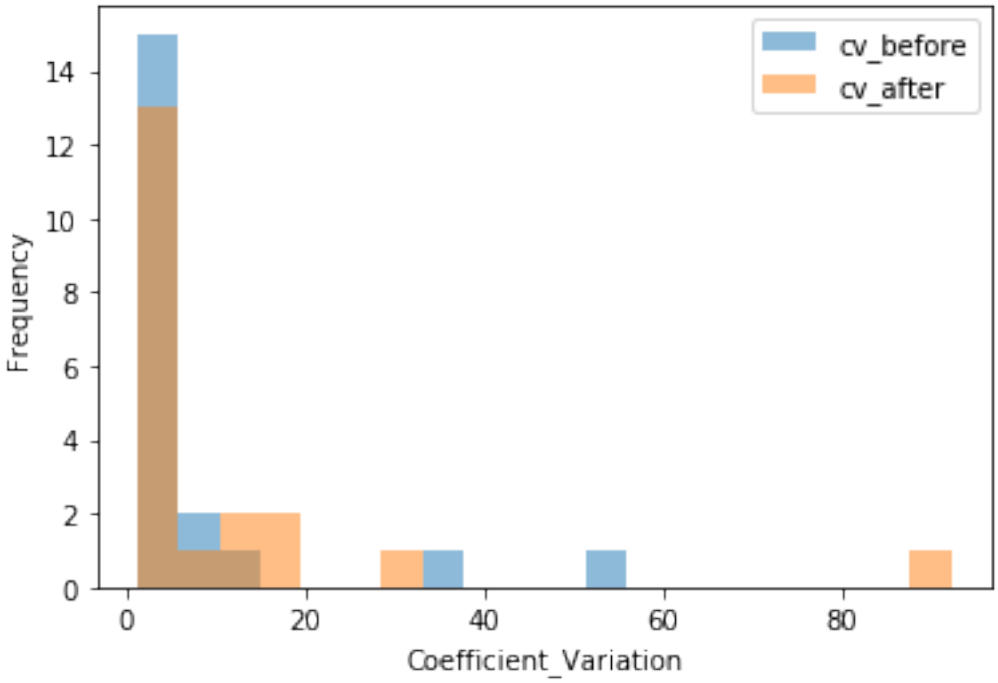

Plot the PTE map

[9]:
```
##check the cut plot statistics

with open(file , 'rb') as infile:
    data_in = infile.readlines()
#be = pd.read_csv('/Users/xifanwang/Desktop/experiment_data/pte/1-2_x_0_cut.
↪csv')
```

[6]:
```
with open (file, 'wb') as outfile:
    outfile.writelines(data_in[4:])
```

[22]:
```
'''normalize via take the max value of the bottom half of the data where there␣
↪is no sam'''
def normalize(df,df1):
    mx1 = max(df['x_v'][201:400])
    mx2 = max(df1['x_v'][201:400])
    return mx1,mx2
```

[39]:
```
def normalize(df,df1):
    mx1 = max(df['x_v'])
    mx2 = max(df1['x_v'])
    return mx1,mx2
```

[40]:
```
#df = pd.read_csv("/Users/xifanwang/Desktop/10222019/1-10_x_1.csv")
#df1 = pd.read_csv('/Users/xifanwang/Desktop/10172019/1-10_x_1.csv')
df = df.drop(['x_raw', 'y_raw',], axis=1)
df1 = df1.drop(['x_raw', 'y_raw',], axis=1)
df['x_v'] = df['x_v']
df1['x_v'] = df1['x_v']
```

[41]:
```
def reformate(df,df1):
    xx = np.ravel(df['x_pixel']); yy = np.ravel(df['y_pixel']) ; zz = np.
 ↪ravel(df['x_v'])
    xx0 = np.ravel(df1['x_pixel']); yy0 = np.ravel(df1['y_pixel']) ; zz0 = np.
 ↪ravel(df1['x_v'])
    xx = np.reshape(xx, (40, 10))
    yy = np.reshape(yy, (40, 10))
    zz = np.reshape(zz, (40, 10))
    zz0 = np.reshape(zz0, (40, 10))
    return zz,zz0
```

[42]:
```
zz, zz0 = reformate(df,df1)
```

[36]:
```
np.sum((zz-zz.mean())**2)/400
```

[36]:
```
2.67505851375e-13
```

[37]:
```
np.sum((zz0-zz0.mean())**2)/400
```

[37]:
```
3.320235357750001e-13
```

[43]:
```
norm = cm.colors.Normalize(vmax=max(abs(zz).max()/2,abs(zz0).max()),␣
 ↪vmin=-max(abs(zz).max()/2,abs(zz0).max()))
#norm = cm.colors.Normalize(vmax=1, vmin=-1)
extent = (0,9,0,39)
cmap = cm.seismic
```

[44]:
```
fig, _axs = plt.subplots(nrows=1, ncols=2)
fig.subplots_adjust(hspace=1)
axs = _axs.flatten()
level= np.arange(-max(abs(zz).max(),abs(zz0).max()),max(abs(zz).max(),abs(zz0).
 ↪max()))
axs[0].imshow(zz, extent=extent, cmap=cmap, norm=norm)
axs[0].set_title("Pre annealing")
axs[1].imshow(zz0, extent=extent, cmap=cmap, norm=norm)
axs[1].set_title("Post annealing")
#im = axs[0].imshow(zz0, extent=extent,cmap=cmap, norm=norm)

fig.colorbar(im, ax=axs[0])
fig.savefig('/Users/xifanwang/Desktop/experiment_data/2-10.png')
```

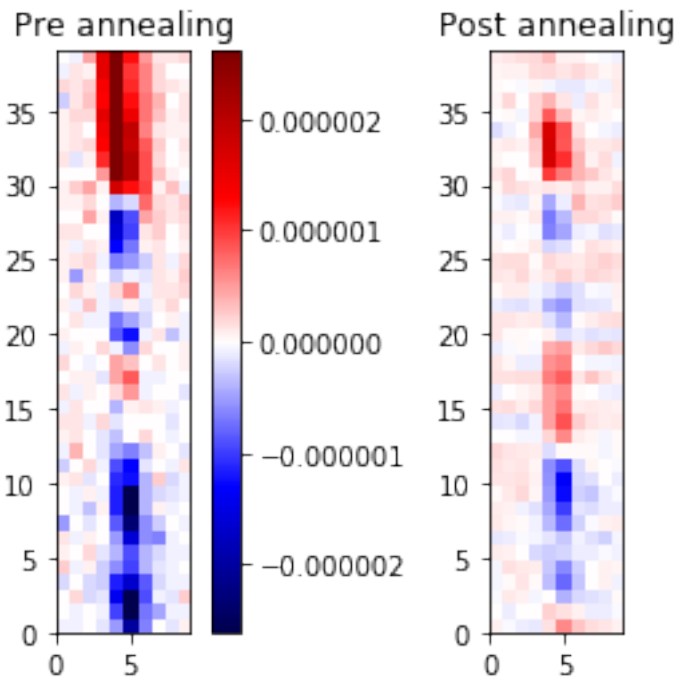
Pre annealing
Post annealing
0.000002
0.000001
0.000000
−0.000001
−0.000002
0
5
10
15
20
25
30
35

[ ]:

Appendix B

Measurement Code

dvdi_measurement

August 14, 2020

[1]:
```
import win32com.client
from tqdm import tqdm
from time import sleep
import time
import numpy as np
import matplotlib.pyplot as plt
from IPython import display
import os
import gc
```

[2]:
```
def read_temp(T_addr,n):
    Labview = win32com.client.Dispatch('Labview.Application')
    VI = Labview.getvireference(T_addr)
    VI._FlagAsMethod("Call")  # Flag "Call" as Method
    call_name, call_para = ['sample_counts'], [n]
    VI.Call(call_name, call_para)
    result=VI.getcontrolvalue('temperature')
    print(result)
    return result
    del VI
```

[3]:
```
def set_heater_range(vi_addr, heater_range = 0):
    Labview = win32com.client.Dispatch('Labview.Application')
    VI = Labview.getvireference(vi_addr)
    VI._FlagAsMethod("Call")  # Flag "Call" as Method
    call_name, call_para = ['Range (0:Off)'], [heater_range]
    VI.Call(call_name, call_para)
    del VI
```

[4]:
```
def set_temp_ramp(vi_addr, temp = 5,ramp=5):
    Labview = win32com.client.Dispatch('Labview.Application')
    VI = Labview.getvireference(vi_addr)
    VI._FlagAsMethod("Call")  # Flag "Call" as Method
    call_name, call_para = ['Setpoint (0.0000)','Ramp Rate (0.0)'], [temp,ramp]
    VI.Call(call_name, call_para)
    del VI
```

[5]:
```
def read_dac_5channel(vi_addr):
    Labview = win32com.client.Dispatch('Labview.Application')
    VI = Labview.getvireference(vi_addr)
    VI._FlagAsMethod("Call")  # Flag "Call" as Method
    VI.Call()
    return [VI.getcontrolvalue(f'CH{i}') for i in range(0,5)]
    del VI
```

[6]:
```
def rigol_sine(vi_addr, amp = 0.002, fre=677, offset=0):
    #amp = [amp,1]
    Labview = win32com.client.Dispatch('Labview.Application')
    VI = Labview.getvireference(vi_addr)
    VI._FlagAsMethod("Call")  # Flag "Call" as Method
    call_name, call_para = ['Amplitude (5.0 Vpp)','Frequency (1000 Hz)','DC␣
 ↪Offset (0 V)'], [amp,fre,offset]
    VI.Call(call_name, call_para)
    del VI
```

[7]:
```
def avg_read_dac_5channel(n):
    r0,r1,r2,r3,r4=0,0,0,0,0
    read_dac_5channel_addr='F:\\Labview code for all instruments\\Dac\\read 5␣
 ↪channel.vi'
    for i in range(n):
        [CH0, CH1, CH2, CH3, CH4]=read_dac_5channel(read_dac_5channel_addr)
        r0 += CH0/n
        r1 += CH1/n
        r2 += CH2/n
        r3 += CH3/n
        r4 += CH4/n
    return [r0,r1,r2,r3,r4]
```

[28]:
```
def read_dac_channel_0(vi_addr):
    Labview = win32com.client.Dispatch('Labview.Application')
    VI = Labview.getvireference(vi_addr)
    VI._FlagAsMethod("Call")  # Flag "Call" as Method
    VI.Call()
    return VI.getcontrolvalue('CH0')
    del VI
```

[29]:
```
def read_dac_channel_1(vi_addr):
    Labview = win32com.client.Dispatch('Labview.Application')
    VI = Labview.getvireference(vi_addr)
    VI._FlagAsMethod("Call")  # Flag "Call" as Method
    VI.Call()
    return VI.getcontrolvalue('CH1')
    del VI
```

[30]:
```
def read_dac_channel_2(vi_addr):
    Labview = win32com.client.Dispatch('Labview.Application')
    VI = Labview.getvireference(vi_addr)
    VI._FlagAsMethod("Call")  # Flag "Call" as Method
    VI.Call()
    return VI.getcontrolvalue('CH2')
    del VI
```

[31]:
```
def read_dac_channel_3(vi_addr):
    Labview = win32com.client.Dispatch('Labview.Application')
    VI = Labview.getvireference(vi_addr)
    VI._FlagAsMethod("Call")  # Flag "Call" as Method
    VI.Call()
    return VI.getcontrolvalue('CH3')
    del VI
```

[32]:
```
def read_dac_channel_4(vi_addr):
    Labview = win32com.client.Dispatch('Labview.Application')
    VI = Labview.getvireference(vi_addr)
    VI._FlagAsMethod("Call")  # Flag "Call" as Method
    VI.Call()
    return VI.getcontrolvalue('CH4')
    del VI
```

[33]:
```
def avg_read_dac_channel_0(n):
    r = 0
    read_dac_channel_addr='F:\\Labview code for all instruments\\Dac\\read␣
 ↪channel 0.vi'
    for i in range(n):
        CH=read_dac_channel_0(read_dac_channel_addr)
        r += CH/n
    return r
```

[34]:
```
def avg_read_dac_channel_1(n):
    r = 0
    read_dac_channel_addr='F:\\Labview code for all instruments\\Dac\\read␣
 ↪channel 1.vi'
    for i in range(n):
        CH=read_dac_channel_1(read_dac_channel_addr)
        r += CH/n
    return r
```

[35]:
```
def avg_read_dac_channel_2(n):
    r = 0
    read_dac_channel_addr='F:\\Labview code for all instruments\\Dac\\read␣
 ↪channel 2.vi'
    for i in range(n):
```

```
        CH=read_dac_channel_2(read_dac_channel_addr)
        r += CH/n
    return r
```

[36]:
```
def avg_read_dac_channel_3(n):
    r = 0
    read_dac_channel_addr='F:\\Labview code for all instruments\\Dac\\read␣
 ↪channel 3.vi'
    for i in range(n):
        CH=read_dac_channel_3(read_dac_channel_addr)
        r += CH/n
    return r
```

[37]:
```
def avg_read_dac_channel_4(n):
    r = 0
    read_dac_channel_addr='F:\\Labview code for all instruments\\Dac\\read␣
 ↪channel 4.vi'
    for i in range(n):
        CH=read_dac_channel_4(read_dac_channel_addr)
        r += CH/n
    return r
```

[10]:
```
rigol_sine(rigol_sine_addr, amp = 0.004, fre=677, offset=0.0)
```

[10]:
```
[CH0, CH1, CH2, CH3, CH4]=read_dac_5channel(read_dac_5channel_addr)
print(CH0)
print(CH1)
print(CH2)
print(CH3)
print(CH4)
```

```
-0.0021732322413095966
6.469323418941172
6.59932455755214
0.00027995649904225944
-0.0016199306481402098
```

[18]:
```
read_dac_channel_0(read_dac_channel_0_addr)
```

[18]:
```
-8.243293998843245e-05
```

[39]:
```
avg_read_dac_channel_4(10)
```

[39]:
```
0.009301553717384 63
```

[61]:
```
read_temp(T_addr,10)
```

```
281.021
```

[61]:
```
281.021
```

[68]:
```
set_heater_range(heater_addr,0)
```

[58]:
```
set_temp_ramp(SetT_addr,290,100)
```

[14]:
```
F=677
applied_Vac=0.004
rigol_sine(rigol_sine_addr, applied_Vac, F, 1.8)

[CH0, CH1, CH2, CH3, CH4]=avg_read_dac_5channel(10)
sr830_V = 50e-6
sr830_I = 50e-6
sr570 = 100e-6
I=CH0*sr570
V=CH4-CH3
Vac = CH1/10*sr830_V
Iac = CH2/10*sr830_I*sr570
dR = Vac/Iac
print(V)
```

```
0.04251120748589722
```

[53]:
```
rigol_sine(rigol_sine_addr, 0.004, 277, 0)
sr830_V = 500e-6
sr830_I = 200e-6
sr570 = 50e-6
CH0=avg_read_dac_channel_0(5)
CH1=avg_read_dac_channel_1(5)
CH2=avg_read_dac_channel_2(5)
CH3=avg_read_dac_channel_3(5)
CH4=avg_read_dac_channel_4(5)
I=CH0*sr570
V=CH4-CH3
Vac = CH1/10*sr830_V
Iac = CH2/10*sr830_I*sr570
dR = Vac/Iac
print(dR)
```

```
9777.12573404275
```

dI/dV read from here

[ ]:
```
i=0
l2=[]
l3=[]
```

```
l4=[]
ln=[]
while i<50:
    CH0=avg_read_dac_channel_0(1)
    sleep(0)
    CH1=avg_read_dac_channel_1(1)
    sleep(0)
    CH2=avg_read_dac_channel_2(1)
    l2.append(CH2)
    sleep(0)
    CH3=avg_read_dac_channel_3(1)
    l3.append(CH3)
    sleep(0)
    CH4=avg_read_dac_channel_4(1)
    l4.append(CH4)
    sleep(0)
    i+=1
    ln.append(i)

plt.figure(1)
plt.scatter(ln, l2, s=40)
plt.autoscale(enable=True, axis='both')

plt.figure(2)
plt.scatter(ln, l3, s=40)
plt.autoscale(enable=True, axis='both')

plt.figure(3)
plt.scatter(ln, l4, s=40)
plt.autoscale(enable=True, axis='both')

display.display(plt.figure(1))
display.display(plt.figure(2))
display.display(plt.figure(3))
```

[ ]:
```
i=0
l2=[]
l3=[]
l4=[]
ln=[]
while i<50:
    CH0=avg_read_dac_channel_0(1)
    sleep(1)
    CH1=avg_read_dac_channel_1(1)
    sleep(1)
    CH2=avg_read_dac_channel_2(1)
    l2.append(CH2)
```

```
    sleep(1)
    CH3=avg_read_dac_channel_3(1)
    l3.append(CH3)
    sleep(1)
    CH4=avg_read_dac_channel_4(1)
    l4.append(CH4)
    sleep(1)
    i+=1
    ln.append(i)

plt.figure(1)
plt.scatter(ln, l2, s=40)
plt.autoscale(enable=True, axis='both')

plt.figure(2)
plt.scatter(ln, l3, s=40)
plt.autoscale(enable=True, axis='both')

plt.figure(3)
plt.scatter(ln, l4, s=40)
plt.autoscale(enable=True, axis='both')

display.display(plt.figure(1))
display.display(plt.figure(2))
display.display(plt.figure(3))
```

[64]:
```
rigol_sine(rigol_sine_addr, 0.004, 277, 0)
sr830_V = 500e-6
sr830_I = 200e-6
sr570 = 50e-6
CH0=avg_read_dac_channel_0(5)
CH1=avg_read_dac_channel_1(5)
CH2=avg_read_dac_channel_2(5)
CH3=avg_read_dac_channel_3(5)
CH4=avg_read_dac_channel_4(5)
I=CH0*sr570
V=CH4-CH3
Vac = CH1/10*sr830_V
Iac = CH2/10*sr830_I*sr570
dR = Vac/Iac
print(dR)
```

```
15664.286179712497
```

[65]:
```
filefolder="F:\\LSCO_didv\\0p12\\4terminal_size2_1"
```

```
sr830_V = 500e-6
sr830_I = 200e-6
sr570 = 50e-6

attenuation = 1

Vinitial=0
Vmaxp= 0.9
Vmaxn=-1.2
Vstep=0.01
F=677
applied_Vac=0.004

V1 = list(np.arange(Vinitial,Vmaxp,Vstep))
V2 = list(np.arange(Vmaxp,Vmaxn,-Vstep))
V3 = list(np.arange(Vmaxn,Vinitial+Vstep,Vstep))

#V = [0.01, 0.02, 0.04] + V1 + V2 + [0.04, 0.02, 0.01]
applied_V = V1 + V2 + V3

set_heater_range(heater_addr,3)
targetT=[5,10,15,20,25,30,35,40,45,50,60,70,100]
for t in targetT:
    set_temp_ramp(SetT_addr,t,0.6)
    while True:
        T=read_temp(T_addr,10)
        if T<t+0.1 and T>t-0.1:
            if t==5:
                sleep(900)
            sleep(900)
            # This one use function generator to change bias

            folder_name = filefolder+'/' + str(t) + "_K_2.dat"
            color = np.random.rand(3,)
            print(folder_name)
            f = open(folder_name, 'w+')
            t0 = time.time()

            kb=1.38e-23
            e=1.6e-19

            figure_i=0
            for applied_v in applied_V:
                #applied_v=0
                #applied_v=float(applied_v)
                rigol_sine(rigol_sine_addr, applied_Vac, F, applied_v)
                sleep(6)
```

```
            CH0=avg_read_dac_channel_0(40)
            sleep(1)
            CH1=avg_read_dac_channel_1(40)
            sleep(1)
            CH2=avg_read_dac_channel_2(40)
            sleep(1)
            CH3=avg_read_dac_channel_3(40)
            sleep(1)
            CH4=avg_read_dac_channel_4(40)
            I=CH0*sr570
            V=CH4-CH3
            Vac = CH1/10*sr830_V
            Iac = CH2/10*sr830_I*sr570
            dR = Vac/Iac
            if figure_i%15==0:

                plt.figure(1)
                plt.scatter([V*1e3], [dR], c=color, s=40)
                plt.xlabel('Voltage(mv) ', fontsize = 16)
                plt.ylabel('dV/dI(ohm)', fontsize = 16)
                plt.autoscale(enable=True, axis='both')

                plt.figure(2)
                plt.scatter([V*1e3], [1000/dR], c=color, s=40)
                plt.xlabel('Voltage(mv) ', fontsize = 16)
                plt.ylabel('dI/dV(mS)', fontsize = 16)
                plt.autoscale(enable=True, axis='both')

                plt.figure(3)
                plt.scatter([V*1e3], [I*1e3], c=color, s=40)
                plt.xlabel('Voltage(mv)', fontsize = 16)
                plt.ylabel('Current(mA)', fontsize = 16)
                plt.autoscale(enable=True, axis='both')

                display.display(plt.figure(1))
                display.display(plt.figure(2))
                display.display(plt.figure(3))

                display.clear_output(wait = True)

            figure_i+=1
            f.write(f'{V}\t{I}\t{Vac}\t{Iac}\t{dR}\n')
            sleep(0.5)
        delta_t = time.time() - t0
        print(f'Measurement cost {delta_t}s.')
        f.close()
        rigol_sine(rigol_sine_addr, 0.004, F, 0)
```

```
            break
        sleep(10)

#set_heater_range(heater_addr,0)
```

```
      ␣
↪-------------------------------------------------------------------------

       KeyboardInterrupt                         Traceback (most recent call␣
↪last)

       <ipython-input-65-c0d5668b5aae> in <module>
        53                 CH1=avg_read_dac_channel_1(40)
        54                 sleep(1)
   ---> 55                 CH2=avg_read_dac_channel_2(40)
        56                 sleep(1)
        57                 CH3=avg_read_dac_channel_3(40)


       <ipython-input-35-7e3fb7c6c0ce> in avg_read_dac_channel_2(n)
          3     read_dac_channel_addr='F:\\LiyangChen\\Labview code for all␣
↪instruments\\Dac\\read channel 2.vi'
          4     for i in range(n):
   ----> 5         CH=read_dac_channel_2(read_dac_channel_addr)
          6         r += CH/n
          7     return r


       <ipython-input-30-4f8097125a77> in read_dac_channel_2(vi_addr)
          3     VI = Labview.getvireference(vi_addr)
          4     VI._FlagAsMethod("Call")  # Flag "Call" as Method
   ----> 5     VI.Call()
          6     return VI.getcontrolvalue('CH2')
          7     del VI


       F:\LiyangChen\Anaconda\lib\site-packages\win32com\client\dynamic.py in␣
↪Call(self, *args)


       KeyboardInterrupt:
```

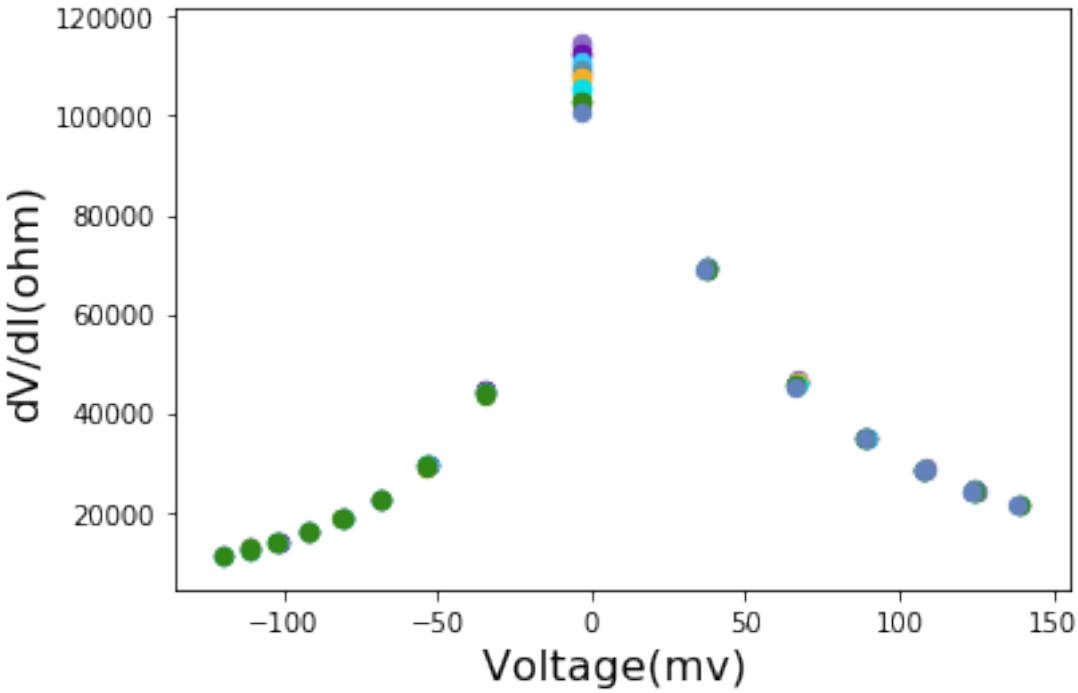
120000
100000
80000
60000
40000
20000
dV/dI(ohm)
−100
−50
0
50
100
150
Voltage(mv)

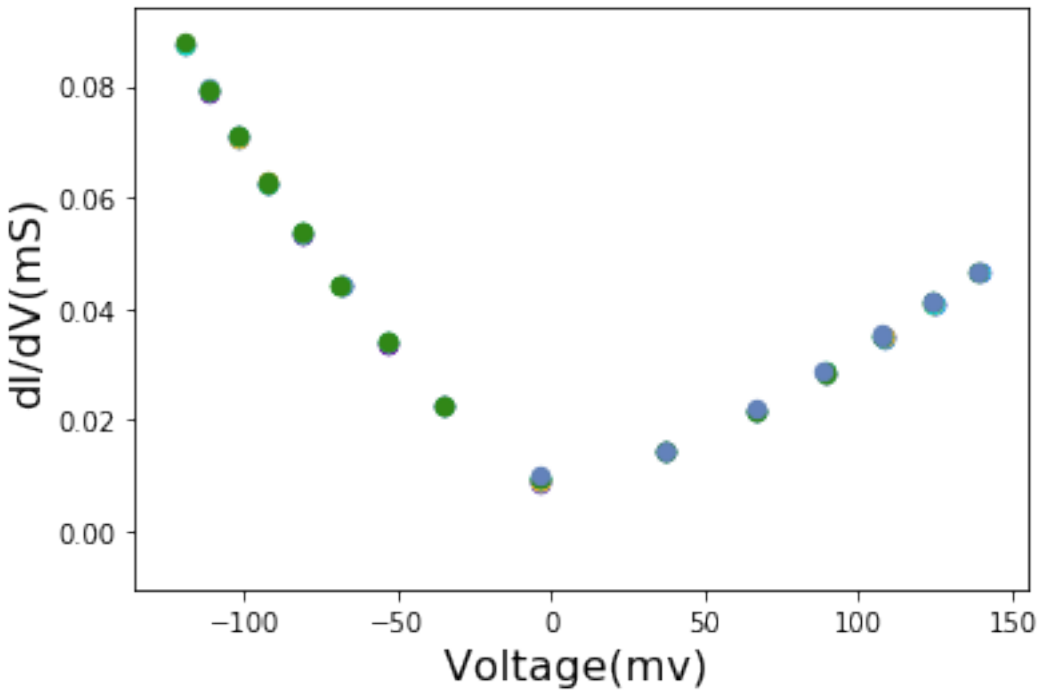
0.08
0.06
0.04
0.02
0.00
dI/dV(mS)
−100
−50
0
50
100
150
Voltage(mv)

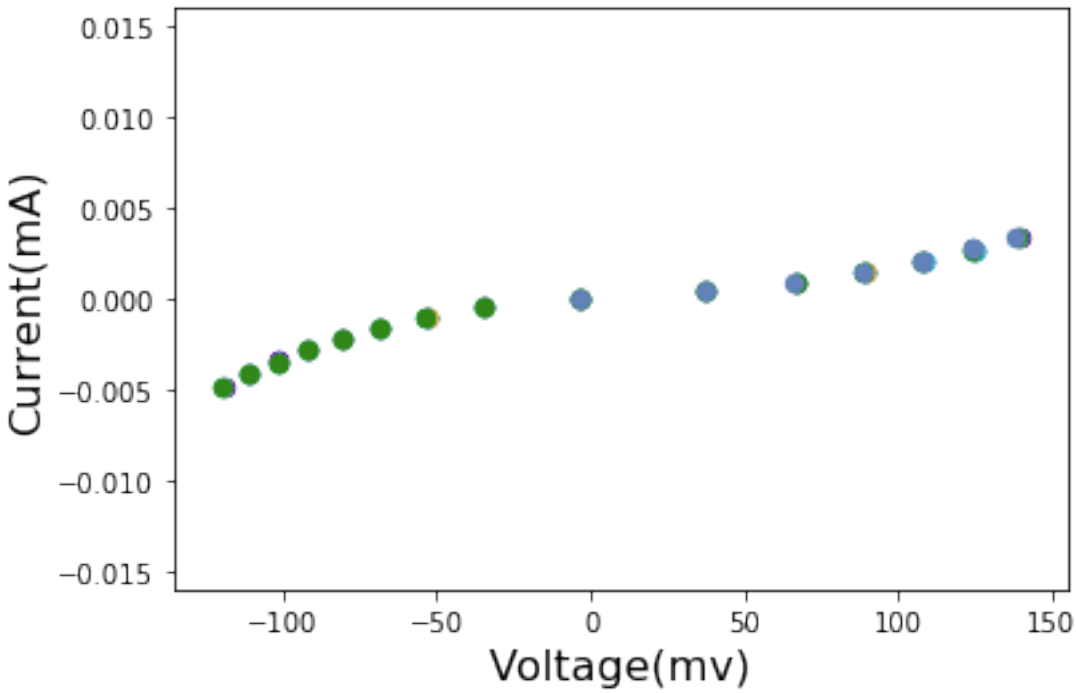

[66]:
```
f.close()
```

[114]:
```
avg_read_dac_5channel(30)
```

[114]:
```
[0.008376925553674397,
 5.20580466602332,
 4.174010459360777,
 0.0002310437649919824,
 0.03700312885359441]
```

[116]:
```
rigol_sine(rigol_sine_addr, amp = 0.004, fre=677, offset=0.0)
```

[67]:
```
filefolder="F:\\_didv\\0p12\\4terminal_size2_1"


sr830_V = 500e-6
sr830_I = 200e-6
sr570 = 50e-6
avg_num=20

attenuation = 1

Vinitial=0
Vmaxp= 0.9
```

```
Vmaxn=-1.2
Vstep=0.01
F=677
applied_Vac=0.004

V1 = list(np.arange(Vinitial,Vmaxp,Vstep))
V2 = list(np.arange(Vmaxp,Vmaxn,-Vstep))
V3 = list(np.arange(Vmaxn,Vinitial+Vstep,Vstep))

#V = [0.01, 0.02, 0.04] + V1 + V2 + [0.04, 0.02, 0.01]
applied_V = V1 + V2 + V3

set_heater_range(heater_addr,3)
targetT=[40,45,50,60,70,100]
for t in targetT:
    set_temp_ramp(SetT_addr,t,0.6)
    while True:
        T=read_temp(T_addr,10)
        if T<t+0.1 and T>t-0.1:
            if t==5:
                sleep(900)
            sleep(900)
            # This one use function generator to change bias

            folder_name = filefolder+'/' + str(t) + "_K_2.dat"
            color = np.random.rand(3,)
            print(folder_name)
            f = open(folder_name, 'w+')
            t0 = time.time()

            kb=1.38e-23
            e=1.6e-19

            figure_i=0
            for applied_v in applied_V:
                #applied_v=0
                #applied_v=float(applied_v)
                rigol_sine(rigol_sine_addr, applied_Vac, F, applied_v)
                sleep(6)
                CH0=avg_read_dac_channel_0(avg_num)
                sleep(1)
                CH1=avg_read_dac_channel_1(avg_num)
                sleep(1)
                CH2=avg_read_dac_channel_2(avg_num)
                sleep(1)
                CH3=avg_read_dac_channel_3(avg_num)
                sleep(1)
```

```
                CH4=avg_read_dac_channel_4(avg_num)
                I=CH0*sr570
                V=CH4-CH3
                Vac = CH1/10*sr830_V
                Iac = CH2/10*sr830_I*sr570
                dR = Vac/Iac
                if figure_i%15==0:

                    plt.figure(1)
                    plt.scatter([V*1e3], [dR], c=color, s=40)
                    plt.xlabel('Voltage(mv) ', fontsize = 16)
                    plt.ylabel('dV/dI(ohm)', fontsize = 16)
                    plt.autoscale(enable=True, axis='both')

                    plt.figure(2)
                    plt.scatter([V*1e3], [1000/dR], c=color, s=40)
                    plt.xlabel('Voltage(mv) ', fontsize = 16)
                    plt.ylabel('dI/dV(mS)', fontsize = 16)
                    plt.autoscale(enable=True, axis='both')

                    plt.figure(3)
                    plt.scatter([V*1e3], [I*1e3], c=color, s=40)
                    plt.xlabel('Voltage(mv)', fontsize = 16)
                    plt.ylabel('Current(mA)', fontsize = 16)
                    plt.autoscale(enable=True, axis='both')

                    display.display(plt.figure(1))
                    display.display(plt.figure(2))
                    display.display(plt.figure(3))

                    display.clear_output(wait = True)

                figure_i+=1
                f.write(f'{V}\t{I}\t{Vac}\t{Iac}\t{dR}\n')
                sleep(0.5)
            delta_t = time.time() - t0
            print(f'Measurement cost {delta_t}s.')
            f.close()
            rigol_sine(rigol_sine_addr, 0.004, F, 0)

            break
        sleep(10)

#set_heater_range(heater_addr,0)
```

```
Measurement cost 13172.68056845665s.
```

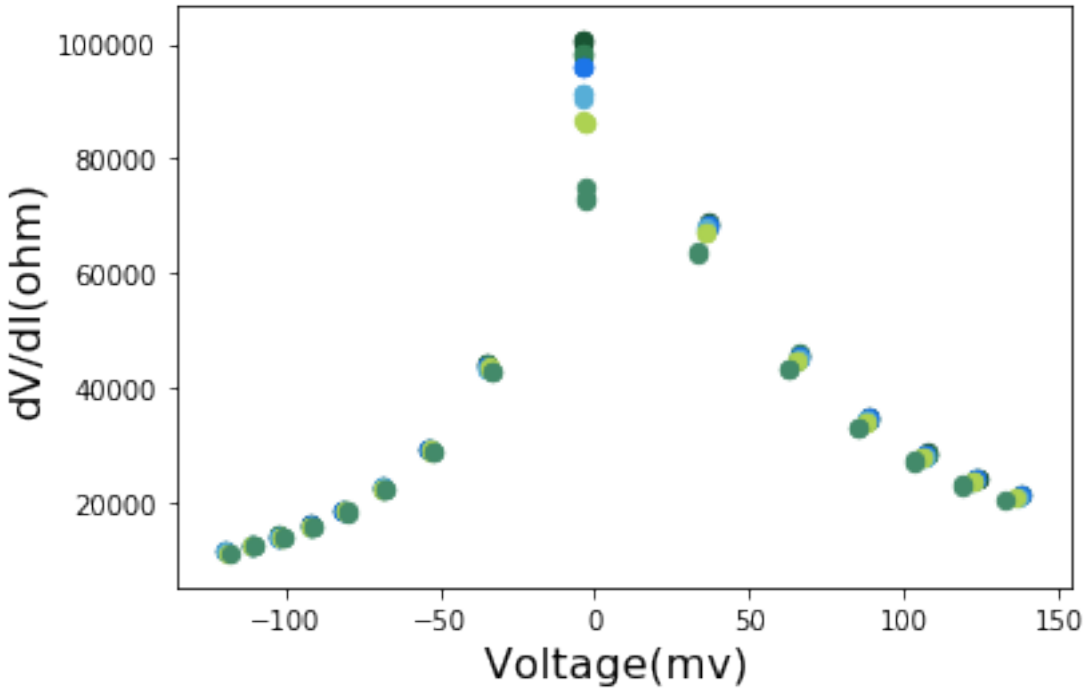
100000
80000
60000
40000
20000
dV/dI(ohm)
−100
−50
0
50
100
150
Voltage(mv)

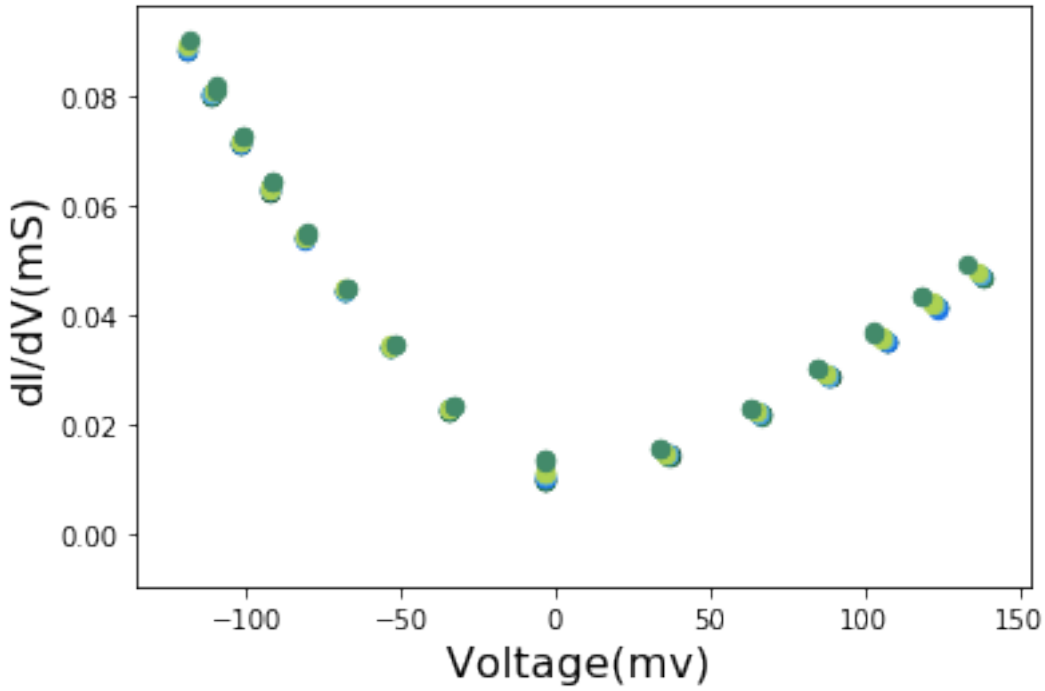
0.08
0.06
0.04
0.02
0.00
dI/dV(mS)
−100
−50
0
50
100
150
Voltage(mv)

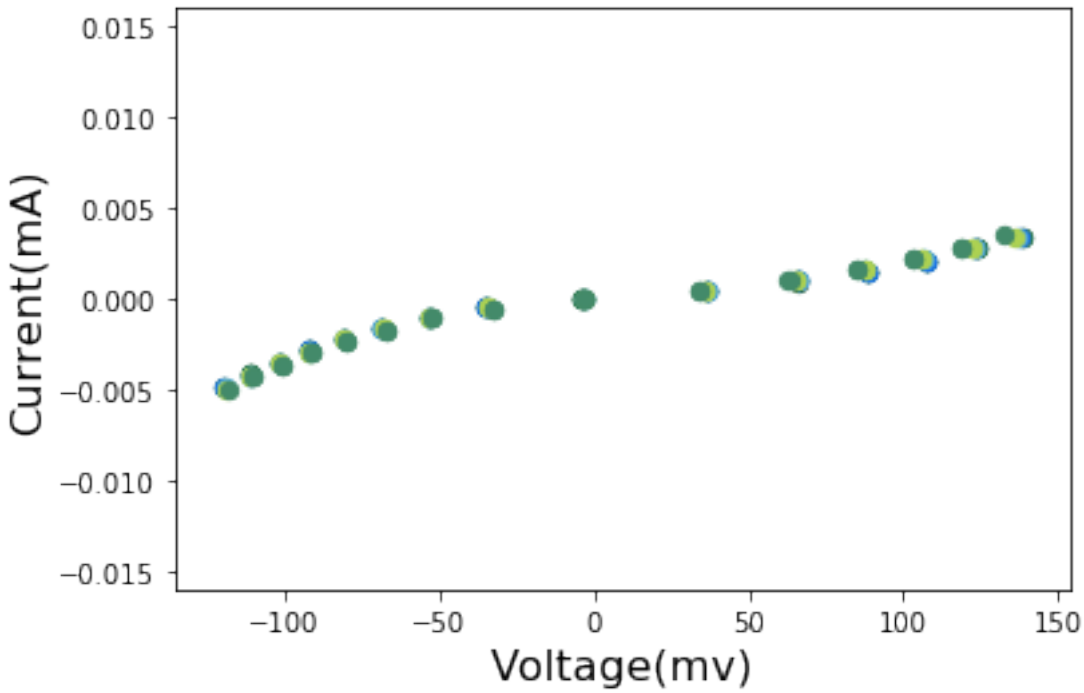

[80]:
```
set_temp_ramp(SetT_addr,5,100)
```

[83]:
```
set_heater_range(heater_addr,0)
set_temp_ramp(SetT_addr,293,0.6)
```

[82]:
```
sr830_V = 1000e-6
sr830_I = 200e-6
sr570 = 50e-6
avg_num=2
CH0=avg_read_dac_channel_0(avg_num)
sleep(1)
CH1=avg_read_dac_channel_1(avg_num)
sleep(1)
CH2=avg_read_dac_channel_2(avg_num)
sleep(1)
CH3=avg_read_dac_channel_3(avg_num)
sleep(1)
CH4=avg_read_dac_channel_4(avg_num)
I=CH0*sr570
V=CH4-CH3
Vac = CH1/10*sr830_V
Iac = CH2/10*sr830_I*sr570
dR = Vac/Iac
print(dR)
```

131416.6815282485

Appendix C

Motor Control Code

Motor_Control

August 13, 2020

[ ]:
```
import sys
import time
import RPi.GPIO as GPIO


GPIO.setmode(GPIO.BCM)


StepPins = [17,22,23,24]


for pin in StepPins:
  print "Setup pins"
  GPIO.setup(pin,GPIO.OUT)
  GPIO.output(pin, False)

# Define advanced sequence
# as shown in manufacturers datasheet
Seq = [[1,0,0,1],
       [1,0,0,0],
       [1,1,0,0],
       [0,1,0,0],
       [0,1,1,0],
       [0,0,1,0],
       [0,0,1,1],
       [0,0,0,1]]

StepCount = len(Seq)
StepDir = 1 # Set to 1 or 2 for clockwise
            # Set to -1 or -2 for anti-clockwise

# Read wait time from command line
if len(sys.argv)&gt;1:
  WaitTime = int(sys.argv[1])/float(1000)
else:
  WaitTime = 10/float(1000)
```

```
# Initialise variables
StepCounter = 0

# Start main loop
while True:

  print StepCounter,
  print Seq[StepCounter]

  for pin in range(0, 4):
    xpin = StepPins[pin]#
    if Seq[StepCounter][pin]!=0:
      print " Enable GPIO %i" %(xpin)
      GPIO.output(xpin, True)
    else:
      GPIO.output(xpin, False)

  StepCounter += StepDir

  # If we reach the end of the sequence
  # start again
  if (StepCounter&gt;=StepCount):
    StepCounter = 0
  if (StepCounter&lt;0):
    StepCounter = StepCount+StepDir

  # Wait before moving on
  time.sleep(WaitTime)
```

Bibliography

[1] Y. Du et al. "Flexible thermoelectric materials and devices". In: *Applied Materials Today* 12 (2018), pp. 366–388. ISSN: 2352-9407. DOI: 10.1016/j.apmt.2018.07.004.

[2] J. R. Szczech, J. M. Higgins, and S. Jin. "Enhancement of the thermoelectric properties in nanoscale and nanostructured materials". In: *Journal of Materials Chemistry* 21.12 (2011), pp. 4037–4055. ISSN: 0959-9428. DOI: 10.1039/c0jm02755c.

[3] P. Zolotavin et al. "Plasmonic Heating in Au Nanowires at Low Temperatures: The Role of Thermal Boundary Resistance". In: *ACS Nano* 10.7 (2016), pp. 6972–6979. ISSN: 1936-0851. DOI: 10.1021/acsnano.6b02911.

[4] Charlotte I. Evans. "Bicrystals and Bowties: Photothermoelectric and plasmonic effects of gold nanoscalestructures". Thesis. 2019. URL: https://natelson.web.rice.edu/theses/cie_thesis.pdf.

[5] S.SUGIHARA. "The measurement of thermoelectricity". In: *Materials for Energy Conversion Devices*. Woodhead Publishing, 2005. Chap. 14, pp. 358–364.

[6] Web Page. 2018. URL: https://www.iceqube.com/technical/thermoelectrics-peltier-effect-described/.

[7] F. J. DiSalvo. "Thermoelectric cooling and power generation". In: *Science* 285.5428 (1999), pp. 703–706. ISSN: 0036-8075. DOI: DOI10.1126/science.285.5428.703.

[8] S. J. Mason, Hojem A., and and Zink B. L. Wesenberg D. J.and Avery A.D. "Determining absolute Seebeck coefficients from relative thermopower measurements of thin films and nanostructures". In: *Journal of Applied Physics* 127.8 (2020). DOI: https://doi.org/10.1063/1.5143447.

[9] A. S. Yalamarthy et al. "Significant Phonon Drag Enables High Power Factor in the AlGaN/GaN Two-Dimensional Electron Gas". In: *Nano Lett* 19.6 (2019), pp. 3770–3776. ISSN: 1530-6992 (Electronic) 1530-6984 (Linking). DOI: 10.1021/acs.nanolett.9b00901.

[10] H. Takahashi et al. "Colossal Seebeck effect enhanced by quasi-ballistic phonons dragging massive electrons in FeSb2". In: *Nat Commun* 7 (2016), p. 12732. ISSN: 2041-1723 (Electronic) 2041-1723 (Linking). DOI: 10.1038/ncomms12732.

[11] J. M. Buhmann and M. Sigrist. "Thermoelectric effect of correlated metals: Band-structure effects and the breakdown of Mott's formula". In: *Physical Review B* 88.11 (2013). ISSN: 2469-9950. DOI: ARTN11512810.1103/PhysRevB.88.115128.

[12] X. W. Lu et al. "Progress of Photodetectors Based on the Photothermoelectric Effect". In: *Advanced Materials* 31.50 (2019). ISSN: 0935-9648.

[13] Web Page. 2006. URL: https://www.electronics-cooling.com/2006/11/the-seebeck-coefficient/.

[14] X. Zhou et al. “Temperature Dependence of Electron-Phonon Interactions in Gold Films Rationalized by Time-Domain Ab lnitio Analysis”. In: *Journal of Physical Chemistry C* 121.32 (2017), pp. 17488–17497. ISSN: 1932-7447. DOI: 10.1021/acs.jpcc.7b05211.

[15] V. G. Karpov and D. A. Parshin. “Heat-Conductivity of Glasses at Temperatures Below the Debye Temperature”. In: *Zhurnal Eksperimentalnoi I Teoreticheskoi Fiziki* 88.6 (1985), pp. 2212–2227. ISSN: 0044-4510.

[16] N. Wendling, J. Chaussy, and J. Mazuer. “Thin Gold Wires as Reference for Thermoelectric-Power Measurements of Small Samples from 1.3-K to 350-K”. In: *Journal of Applied Physics* 73.6 (1993), pp. 2878–2881. ISSN: 0021-8979.

[17] Web Page. 2014. URL: https://en.wikipedia.org/wiki/Seebeck_coefficient#/media/File:Absolute_Seebeck_coefficients_of_various_metals_up_to_high_temperatures.svg.

[18] H. H. Andersen and M. Nielsen. “Thermo-Electricity in Gold at Low Temperatures”. In: *Physics Letters* 6.1 (1963), pp. 17–18.

[19] J. Schleeh et al. “Phonon black-body radiation limit for heat dissipation in electronics”. In: *Nature Materials* 14.2 (2015), pp. 187–192. ISSN: 1476-1122. DOI: 10.1038/Nmat4126. URL: %3CGo%20to%20ISI%3E://WOS:000348600200016.

[20] D. Natelson. *Nanostructures and Nanotechnology*. Nanostructures and Nanotechnology. Cambridge University Press, 2015, p. 630. DOI: 10.1017/Cbo9781139025485. URL: %3CGo%20to%20ISI%3E://WOS:000368711100015.

[21] G. P. Szakmany et al. “Single-Metal Nanoscale Thermocouples”. In: *Ieee Transactions on Nanotechnology* 13.6 (2014), pp. 1234–1239. ISSN: 1536-125x. DOI: 10.1109/Tnano.2014.2358532.

[22] G. Li et al. “Linearly enhanced response of thermopower in cascaded array of dual-stripe single-metal thermocouples”. In: *Applied Physics Letters* 110.20 (2017). ISSN: 0003-6951. DOI: Artn20350510.1063/1.4983719.

[23] P. Zolotavin, C. I. Evans, and D. Natelson. “Substantial local variation of the Seebeck coefficient in gold nanowires”. In: *Nanoscale* 9.26 (2017), pp. 9160–9166. ISSN: 2040-3364. DOI: 10.1039/c7nr02678a.

[24] W. Dai et al. “Giant photothermoelectric effect in silicon nanoribbon photodetectors”. In: *Light Sci Appl* 9 (2020), p. 120. ISSN: 2047-7538 (Electronic) 2047-7538 (Linking). DOI: 10.1038/s41377-020-00364-x.

[25] J. Gosciniak, M. Rasras, and J. B. Khurgin. “Ultrafast Plasmonic Graphene Photodetector Based on the Channel Photothermoelectric Effect”. In: *Acs Photonics* 7.2 (2020), pp. 488–498. ISSN: 2330-4022. URL: %3CGo%20to%20ISI%3E://WOS:000515214200022.

[26] D. Wu et al. “Plasmon-Enhanced Photothermoelectric Conversion in Chemical Vapor Deposited Graphene p-n Junctions”. In: *Journal of the American Chemical Society* 135.30 (2013), pp. 10926–10929. ISSN: 0002-7863. URL: %3CGo%20to%20ISI%3E://WOS:000322752900012.

[27] A. B. Dubois. “Plasma Oscillations and Electron - Elecron Interactions in 2D Electron Systems”. In: *International Conference on Theoretical Physics Dubna-Nano 2010* 248 (2010). ISSN: 1742-6588. DOI: Artn01205610.1088/1742-6596/248/1/012056. URL: %3CGo%20to%20ISI%3E://WOS:000291887600056.

[28] M. A. Stroscio et al. “Acoustic phonon quantization in buried waveguides and resonators”. In: *Journal of Physics-Condensed Matter* 8.13 (1996), pp. 2143–2151. ISSN: 0953-8984. URL: %3CGo%20to%20ISI%3E://WOS:A1996UD88400006.

[29] S. I. Bozhevolnyi et al. “Waveguiding in surface plasmon polariton band gap structures”. In: *Physical Review Letters* 86.14 (2001), pp. 3008–3011. ISSN: 0031-9007. DOI: DOI10.1103/PhysRevLett.86.3008. URL: %3CGo%20to%20ISI%3E://WOS:000167866300024.

[30] N. Del Fatti et al. “Nonequilibrium electron dynamics in noble metals”. In: *Physical Review B* 61.24 (2000), pp. 16956–16966. ISSN: 2469-9950. DOI: DOI10.1103/PhysRevB.61.16956. URL: %3CGo%20to%20ISI%3E://WOS:000088008400085.

[31] Nicolas Large. “Resonant Raman-Brillouin scattering in semiconductor and metallic nanostructures : from nano-acoustics to acousto-plasmonics”. In: 2011.

[32] K. S. Lee and M. A. El-Sayed. “Gold and silver nanoparticles in sensing and imaging: Sensitivity of plasmon response to size, shape, and metal composition”. In: *Journal of Physical Chemistry B* 110.39 (2006), pp. 19220–19225. ISSN: 1520-6106. URL: %3CGo%20to%20ISI%3E://WOS:000240825900023.

[33] W. A. Jacak. “Plasmons in Finite Spherical Electrolyte Systems: RPA Effective Jellium Model for Ionic Plasma Excitations”. In: *Plasmonics* 11 (2016), pp. 637–651. ISSN: 1557-1955 (Print) 1557-1955 (Linking). DOI: 10.1007/s11468-015-0064-6. URL: https://www.ncbi.nlm.nih.gov/pubmed/27069439.

[34] R. Matloob et al. “Electromagnetic-Field Quantization in Absorbing Dielectrics”. In: *Physical Review A* 52.6 (1995), pp. 4823–4838. ISSN: 1050-2947. DOI: DOI10.1103/PhysRevA.52.4823. URL: %3CGo%20to%20ISI%3E://WOS:A1995TK65200064.

[35] J. M. Sanz et al. “UV Plasmonic Behavior of Various Metal Nanoparticles in the Near- and Far-Field Regimes: Geometry and Substrate Effects”. In: *Journal of Physical Chemistry C* 117.38 (2013), pp. 19606–19615. ISSN: 1932-

7447. DOI: 10.1021/jp405773p. URL: %3CGo%20to%20ISI%3E://WOS:000330162500041.

[36] M. G. Blaber, M. D. Arnold, and M. J. Ford. "Search for the Ideal Plasmonic Nanoshell: The Effects of Surface Scattering and Alternatives to Gold and Silver". In: *Journal of Physical Chemistry C* 113.8 (2009), pp. 3041–3045. ISSN: 1932-7447. DOI: 10.1021/jp810808h. URL: %3CGo%20to%20ISI%3E://WOS:000263529300002.

[37] E. J. Zeman and G. C. Schatz. "An Accurate Electromagnetic Theory Study of Surface Enhancement Factors for Ag, Au, Cu, Li, Na, Al, Ga, in, Zn, and Cd". In: *Journal of Physical Chemistry* 91.3 (1987), pp. 634–643. ISSN: 0022-3654. DOI: DOI10.1021/j100287a028. URL: %3CGo%20to%20ISI%3E://WOS:A1987F847900028.

[38] W. L. Barnes. "Surface plasmon-polariton length scales: a route to sub-wavelength optics". In: *Journal of Optics a-Pure and Applied Optics* 8.4 (2006), S87–S93. ISSN: 1464-4258. DOI: 10.1088/1464-4258/8/4/S06. URL: %3CGo%20to%20ISI%3E://WOS:000237812800007.

[39] P. Berini and I. De Leon. "Surface plasmon-polariton amplifiers and lasers". In: *Nature Photonics* 6.1 (2012), pp. 16–24. ISSN: 1749-4885. DOI: 10.1038/nphoton.2011.285. URL: %3CGo%20to%20ISI%3E://WOS:000298416200010.

[40] Ankun Yang et al. "Coherent Light Sources at the Nanoscale". In: *Annual Review of Physical Chemistry* 68 (June 2017). DOI: 10.1146/annurev-physchem-052516-050730.

[41] C. Hamon et al. "Hierarchical Self-Assembly of Gold Nanoparticles into Patterned Plasmonic Nanostructures". In: *Acs Nano* 8.10 (2014), pp. 10694–10703.

ISSN: 1936-0851. DOI: 10.1021/nn504407z. URL: %3CGo%20to%20ISI%3E://WOS:000343952600106.

[42] M. Eguchi et al. "Simple Reductant Concentration-Dependent Shape Control of Polyhedral Gold Nanoparticles and Their Plasmonic Properties". In: *Langmuir* 28.24 (2012), pp. 9021–9026. ISSN: 0743-7463. DOI: 10.1021/la3002114. URL: %3CGo%20to%20ISI%3E://WOS:000305320700026.

[43] J. M. Slocik, A. O. Govorov, and R. R. Naik. "Plasmonic Circular Dichroism of Peptide-Functionalized Gold Nanoparticles". In: *Nano Letters* 11.2 (2011), pp. 701–705. ISSN: 1530-6984. DOI: 10.1021/nl1038242. URL: %3CGo%20to%20ISI%3E://WOS:000287049100066.

[44] D. K. Lim et al. "Enhanced Photothermal Effect of Plasmonic Nanoparticles Coated with Reduced Graphene Oxide". In: *Nano Letters* 13.9 (2013), pp. 4075–4079. ISSN: 1530-6984. DOI: 10.1021/nl4014315. URL: %3CGo%20to%20ISI%3E://WOS:000330158900017.

[45] J. B. Lassiter et al. "Fano Resonances in Plasmonic Nanoclusters: Geometrical and Chemical Tunability". In: *Nano Letters* 10.8 (2010), pp. 3184–3189. ISSN: 1530-6984. DOI: 10.1021/nl102108u. URL: %3CGo%20to%20ISI%3E://WOS:000280728900076.

[46] F. Tam, C. Moran, and N. J. Halas. "Geometrical parameters controlling sensitivity of nanoshell plasmon resonances to changes in dielectric environment". In: *Journal of Physical Chemistry B* 108.45 (2004), pp. 17290–17294. ISSN: 1520-6106. DOI: 10.1021/jp048499x. URL: %3CGo%20to%20ISI%3E://WOS:000224993900006.

[47] J. Zuloaga, E. Prodan, and P. Nordlander. "Quantum Description of the Plasmon Resonances of a Nanoparticle Dimer". In: *Nano Letters* 9.2 (2009), pp. 887–891. ISSN: 1530-6984. DOI: 10.1021/nl803811g. URL: %3CGo%20to%20ISI%3E://WOS:000263298700066.

[48] N. Kazemi-Zanjani, S. Vedraine, and F. Lagugne-Labarthet. "Localized enhancement of electric field in tip-enhanced Raman spectroscopy using radially and linearly polarized light". In: *Optics Express* 21.21 (2013), pp. 25271–25276. ISSN: 1094-4087. DOI: 10.1364/Oe.21.025271. URL: %3CGo%20to%20ISI%3E://WOS:000326085600081.

[49] E. X. Jin and X. Xu. "Plasmonic effects in near-field optical transmission enhancement through a single bowtie-shaped aperture". In: *Applied Physics B-Lasers and Optics* 84.1-2 (2006), pp. 3–9. ISSN: 0946-2171. DOI: 10.1007/s00340-006-2237-7. URL: %3CGo%20to%20ISI%3E://WOS:000238828700002.

[50] K. Kneipp. "Raman spectroscopy of single molecules using the help of gold and silver nanoparticles." In: *Abstracts of Papers of the American Chemical Society* 225 (2003), U447–U447. ISSN: 0065-7727. URL: %3CGo%20to%20ISI%3E://WOS:000187918002269.

[51] K. Kneipp et al. "Single molecule Raman spectroscopy using silver and gold nanoparticles". In: *Indian Journal of Physics and Proceedings of the Indian Association for the Cultivation of Science-Part B* 77b.1 (2003), pp. 39–47. URL: %3CGo%20to%20ISI%3E://WOS:000186059000007.

[52] C. M. Ruan, W. Wang, and B. H. Gu. "Single-molecule detection of thionine on aggregated gold nanoparticles by surface enhanced Raman scattering". In:

Journal of Raman Spectroscopy 38.5 (2007), pp. 568–573. ISSN: 0377-0486. URL: %3CGo%20to%20ISI%3E://WOS:000246168800012.

[53] Kaaya Ismail. "Fabrication and characterisation of SERS substrates through photo-deposition of Gold Nanoparticles". PhD thesis. Aug. 2015. DOI: 10.13140/RG.2.1.4401.0963.

[54] D. C. Harris and M. D. Bertolucci. *Symmetry and spectroscopy: an introduction to vibrational and electronic spectroscopy*. New York: Dover Publications, 1989.

[55] R. A. Alvarez-Puebla. "Effects of the Excitation Wavelength on the SERS Spectrum". In: *Journal of Physical Chemistry Letters* 3.7 (2012), pp. 857–866. ISSN: 1948-7185. DOI: 10.1021/jz201625j. URL: %3CGo%20to%20ISI%3E://WOS:000302336800012.

[56] Web Page. URL: http://halas.rice.edu/conversions.

[57] Y. S. Yamamoto, Y. Ozaki, and T. Itoh. "Recent progress and frontiers in the electromagnetic mechanism of surface-enhanced Raman scattering". In: *Journal of Photochemistry and Photobiology C-Photochemistry Reviews* 21 (2014), pp. 81–104. ISSN: 1389-5567. URL: %3CGo%20to%20ISI%3E://WOS:000346887100006.

[58] Mohammad Hossain and Yukihiro Ozaki. "Surface-enhanced Raman scattering: Facts and inline trends". In: *Current Science* 97 (July 2009).

[59] D. R. Ward et al. "Optical rectification and field enhancement in a plasmonic nanogap". In: *Nature Nanotechnology* 5.10 (2010), pp. 732–736. ISSN: 1748-3387. DOI: 10.1038/nnano.2010.176. URL: %3CGo%20to%20ISI%3E://WOS:000282578000012.

[60] D. R. Ward et al. “Electromigrated nanoscale gaps for surface-enhanced Raman spectroscopy”. In: *Nano Letters* 7.5 (2007), pp. 1396–1400. ISSN: 1530-6984. DOI: 10.1021/nl070625w. URL: %3CGo%20to%20ISI%3E://WOS:000246313000050.

[61] D. R. Ward et al. “Simultaneous measurements of electronic conduction and Raman response in molecular junctions”. In: *Nano Letters* 8.3 (2008), pp. 919–924. ISSN: 1530-6984. DOI: 10.1021/nl073346h. URL: %3CGo%20to%20ISI%3E://WOS:000253947400028.

[62] D. R. Ward et al. “Electronic and optical properties of electromigrated molecular junctions”. In: *Journal of Physics-Condensed Matter* 20.37 (2008). ISSN: 0953-8984. DOI: Artn37411810.1088/0953-8984/20/37/374118. URL: %3CGo%20to%20ISI%3E://WOS:000258734700020.

[63] Y. J. Li et al. “Interplay of Bias-Driven Charging and the Vibrational Stark Effect in Molecular Junctions”. In: *Nano Letters* 16.2 (2016), pp. 1104–1109. ISSN: 1530-6984. DOI: 10.1021/acs.nanolett.5b04340. URL: %3CGo%20to%20ISI%3E://WOS:000370215200043.

[64] Y. Li et al. “Voltage tuning of vibrational mode energies in single-molecule junctions”. In: *Proceedings of the National Academy of Sciences of the United States of America* 111.4 (2014), pp. 1282–1287. ISSN: 0027-8424. DOI: 10.1073/pnas.1320210111. URL: %3CGo%20to%20ISI%3E://WOS:000330231100029.

[65] D. Natelson, Y. J. Li, and P. Zolotavin. “Nanogap plasmonic structures for Raman studies of single molecules and heating”. In: *Abstracts of Papers of the American Chemical Society* 249 (2015). ISSN: 0065-7727. URL: %3CGo%20to%20ISI%3E://WOS:000411183303537.

[66] J. B. Herzog et al. “Dark Plasmons in Hot Spot Generation and Polarization in Interelectrode Nanoscale Junctions”. In: *Nano Letters* 13.3 (2013), pp. 1359–1364. ISSN: 1530-6984. DOI: 10.1021/nl400363d. URL: %3CGo%20to%20ISI%3E://WOS:000316243800078.

[67] J. B. Herzog, M. W. Knight, and D. Natelson. “Thermoplasmonics: Quantifying Plasmonic Heating in Single Nanowires”. In: *Nano Letters* 14.2 (2014), pp. 499–503. ISSN: 1530-6984. URL: %3CGo%20to%20ISI%3E://WOS:000331343900016.

[68] J. B. Herzog, M. W. Knight, and D. Natelson. “Thermoplasmonics: Quantifying Plasmonic Heating in Single Nanowires”. In: *Nano Letters* 14.2 (2014), pp. 499–503. ISSN: 1530-6984. URL: %3CGo%20to%20ISI%3E://WOS:000331343900016.

[69] S. J. Bauman et al. “Fabrication of Sub-Lithography-Limited Structures via Nanomasking Technique for Plasmonic Enhancement Applications”. In: *Ieee Transactions on Nanotechnology* 14.5 (2015), pp. 790–793. ISSN: 1536-125x. DOI: 10.1109/Tnano.2015.2457235. URL: %3CGo%20to%20ISI%3E://WOS:000364504200002.

[70] H. Park et al. “Fabrication of metallic electrodes with nanometer separation by electromigration”. In: *Applied Physics Letters* 75.2 (1999), pp. 301–303. ISSN: 0003-6951. URL: %3CGo%20to%20ISI%3E://WOS:000081265200051.

[71] R. S. Sorbello. “Microscopic driving forces for electromigration”. In: *Advanced Metallization for Future Ulsi* 427 (1996), pp. 73–81. ISSN: 0886-7860. DOI: Doi10.1557/Proc-427-73. URL: %3CGo%20to%20ISI%3E://WOS:A1996BG72C00009.

[72] “Electromigration Driving Force”. In: (). URL: https://www.iue.tuwien.ac.at/phd/rovitto/node35.html.

[73] P. Zolotavin, C. I. Evans, and D. Natelson. "Substantial local variation of the Seebeck coefficient in gold nanowires". In: *Nanoscale* 9.26 (2017), pp. 9160–9166. ISSN: 2040-3364. URL: %3CGo%20to%20ISI%3E://WOS:000411293800031.

[74] Web Page. 2018. URL: https://www.rrutc.msm.cam.ac.uk/outreach/articles/the-scanning-electron-microscope.

[75] T. Betancourt and L. Brannon-Peppas. "Micro- and nanofabrication methods in nanotechnological medical and pharmaceutical devices". In: *International Journal of Nanomedicine* 1.4 (2006), pp. 483–495. ISSN: 1178-2013. URL: %3CGo%20to%20ISI%3E://WOS:000252048400011.

[76] Panpan Zhou. "Shot Noise Measurements in Strongly Correlated Materials". Thesis. 2019. URL: https://natelson.web.rice.edu/theses/zhou_thesis.pdf.

[77] F. R. Newbold and N. R. Amundson. "Model for Evaporation of a Multicomponent Droplet". In: *Aiche Journal* 19.1 (1973), pp. 22–30. ISSN: 0001-1541. DOI: DOI10.1002/aic.690190105. URL: %3CGo%20to%20ISI%3E://WOS:A197305084000004.

[78] Web Page. 2012. URL: https://en.wikipedia.org/wiki/Electron-beam_physical_vapor_deposition.

[79] Web Page. 2020. URL: http://www.integratedhybridassembly.com/plasma-cleaning/.

[80] Y. Y. Long, J. Twiefel, and J. Wallaschek. "A review on the mechanisms of ultrasonic wedge-wedge bonding". In: *Journal of Materials Processing Technology* 245 (2017), pp. 241–258. ISSN: 0924-0136. DOI: 10.1016/j.jmatprotec.2017.02.012.

[81] P. J. Wang et al. "The SERS study of graphene deposited by gold nanoparticles with 785 nm excitation". In: *Chemical Physics Letters* 556 (2013), pp. 146–150. ISSN: 0009-2614. DOI: 10.1016/j.cplett.2012.11.018. URL: %3CGo%20to%20ISI%3E://WOS:000313644100029.

[82] D.W. Snoke. *Solid state physics : essential concepts*. San Francisco: Addison-Wesley, 2009.

[83] M. G. Helander et al. "Pitfalls in measuring work function using photoelectron spectroscopy". In: *Applied Surface Science* 256.8 (2010), pp. 2602–2605. ISSN: 0169-4332. DOI: 10.1016/j.apsusc.2009.11.002. URL: %3CGo%20to%20ISI%3E://WOS:000273670700051.

[84] P. A. F. Garrillo et al. "Calibrated work function mapping by Kelvin probe force microscopy". In: *Review of Scientific Instruments* 89.4 (2018). ISSN: 0034-6748. DOI: Artn04370210.1063/1.5007619. URL: %3CGo%20to%20ISI%3E://WOS:000431139400025.

[85] Web Page. URL: https://parksystems.com/park-spm-modes/93-dielectric-piezoelectric/232-kelvin-probe-force-microscopy-kpfm.

[86] M. Nonnenmacher, M. P. Oboyle, and H. K. Wickramasinghe. "Kelvin Probe Force Microscopy". In: *Applied Physics Letters* 58.25 (1991), pp. 2921–2923. ISSN: 0003-6951. DOI: Doi10.1063/1.105227.

[87] A. Krozer and M. Rodahl. "X-ray photoemission spectroscopy study of UV/ozone oxidation of Au under ultrahigh vacuum conditions". In: *Journal of Vacuum Science Technology a-Vacuum Surfaces and Films* 15.3 (1997), pp. 1704–1709. ISSN: 0734-2101. DOI: Doi10.1116/1.580924. URL: %3CGo%20to%20ISI%3E://WOS:A1997XE73200107.

[88] H. C. Tsai et al. “Instability of gold oxide Au2O3”. In: *Surface Science* 537.1-3 (2003), pp. L447–L450. ISSN: 0039-6028. DOI: 10.1016/S0039-6028(03)00640-X. URL: %3CGo%20to%20ISI%3E://WOS:000183850600006.

[89] M. Tchaplyguine et al. “Gold Oxide Nanoparticles with Variable Gold Oxidation State”. In: *Journal of Physical Chemistry C* 119.16 (2015), pp. 8937–8943. ISSN: 1932-7447. DOI: 10.1021/acs.jpcc.5b00811. URL: %3CGo%20to%20ISI%3E://WOS:000353603500059.

[90] S. Rentenberger et al. “UV/ozone treated Au for air-stable, low hole injection barrier electrodes in organic electronics”. In: *Journal of Applied Physics* 100.5 (2006). ISSN: 0021-8979. DOI: Artn05370110.1063/1.2336345. URL: %3CGo%20to%20ISI%3E://WOS:000240602500056.

[91] F. Machalett et al. “Direct patterning of gold oxide thin films by focused ion-beam irradiation”. In: *Applied Physics a-Materials Science Processing* 71.3 (2000), pp. 331–335. ISSN: 0947-8396. DOI: DOI10.1007/s003390000598. URL: %3CGo%20to%20ISI%3E://WOS:000089207700017.

[92] B. Steinhauser et al. “Localized-Plasmon Voltammetry to Detect pH Dependent Gold Oxidation”. In: *Journal of Physical Chemistry C* 122.8 (2018), pp. 4565–4571. ISSN: 1932-7447. DOI: 10.1021/acs.jpcc.7b11355. URL: %3CGo%20to%20ISI%3E://WOS:000426802500051.

[93] X. D. Xu et al. “Photo-Thermoelectric Effect at a Graphene Interface Junction”. In: *Nano Letters* 10.2 (2010), pp. 562–566. ISSN: 1530-6984. DOI: 10.1021/nl903451y. URL: %3CGo%20to%20ISI%3E://WOS:000274338800035.

[94] S. F. Shi et al. “Plasmon Resonance in Individual Nanogap Electrodes Studied Using Graphene Nanoconstrictions as Photodetectors”. In: *Nano Letters*

11.4 (2011), pp. 1814–1818. ISSN: 1530-6984. DOI: 10.1021/nl200522t. URL: %3CGo%20to%20ISI%3E://WOS:000289341500075.

[95] N. F. Mott and H. Jones. *The Theory of the Properties of Metals and Alloys*. Dover Publications, 1958.

[96] H. X. Liu, W. Q. Sun, and S. Y. Xu. "An Extremely Simple Thermocouple Made of a Single Layer of Metal". In: *Advanced Materials* 24.24 (2012), pp. 3275–3279. ISSN: 0935-9648. DOI: 10.1002/adma.201200644. URL: %3CGo%20to%20ISI%3E://WOS:000305450500018.

[97] Y. L. Liu et al. "Controllable Localized Surface Plasmonic Resonance Phenomena in Reduced Gold Oxide Films". In: *Chemistry of Materials* 26.5 (2014), pp. 1799–1806. ISSN: 0897-4756. DOI: 10.1021/cm403227w. URL: %3CGo%20to%20ISI%3E://WOS:000332913400007.

[98] W. B. Hou and S. B. Cronin. "A Review of Surface Plasmon Resonance-Enhanced Photocatalysis". In: *Advanced Functional Materials* 23.13 (2013), pp. 1612–1619. ISSN: 1616-301x. DOI: 10.1002/adfm.201202148. URL: %3CGo%20to%20ISI%3E://WOS:000317019100002.

[99] M. L. Brongersma, N. J. Halas, and P. Nordlander. "Plasmon-induced hot carrier science and technology". In: *Nature Nanotechnology* 10.1 (2015), pp. 25–34. ISSN: 1748-3387. DOI: 10.1038/Nnano.2014.311. URL: %3CGo%20to%20ISI%3E://WOS:000347405800015.

[100] X. X. Huang, N. Hansen, and N. Tsuji. "Hardening by annealing and softening by deformation in nanostructured metals". In: *Science* 312.5771 (2006), pp. 249–251. ISSN: 0036-8075. DOI: 10.1126/science.1124268. URL: %3CGo%20to%20ISI%3E://WOS:000236765300043.

[101] Lucia Gan et al. “High-Throughput Growth of Microscale Gold Bicrystals for Single-Grain-Boundary Studies”. In: *Advanced Materials* 31 (June 2019), p. 1902189. DOI: 10.1002/adma.201902189.

[102] J. K. A. Amuzu. “The Effect of Tensile-Stress on the Thermoelectric Emf in Copper, Gold, and Silver”. In: *Physica Status Solidi a-Applied Research* 63.1 (1981), K7–K10. ISSN: 0031-8965. URL: %3CGo%20to%20ISI%3E://WOS:A1981LD71200050.

[103] J. R. Drabble and R. D. Groves. “The Effect of Strain on the Seebeck Coefficient of N-Type Germanium”. In: *Journal of Physics and Chemistry of Solids* 12.3-4 (1960), pp. 285–294. ISSN: 0022-3697. URL: %3CGo%20to%20ISI%3E://WOS:A1960WH86300008.

[104] A. Fursina et al. “Nanogaps with very large aspect ratios for electrical measurements”. In: *Applied Physics Letters* 92.11 (2008). ISSN: 0003-6951. URL: %3CGo%20to%20ISI%3E://WOS:000254292400078.

[105] I. H. Campbell et al. “Controlling Schottky energy barriers in organic electronic devices using self-assembled monolayers”. In: *Physical Review B* 54.20 (1996), pp. 14321–14324. ISSN: 0163-1829. DOI: DOI10.1103/PhysRevB.54.R14321. URL: %3CGo%20to%20ISI%3E://WOS:A1996VX71700026.

[106] B. H. Hamadani et al. “Controlling charge injection in organic field-effect transistors using self-assembled monolayers”. In: *Nano Letters* 6.6 (2006), pp. 1303–1306. ISSN: 1530-6984. DOI: 10.1021/nl060731i. URL: %3CGo%20to%20ISI%3E://WOS:000238258300043.

[107] B. de Boer et al. “Tuning of metal work functions with self-assembled monolayers”. In: *Advanced Materials* 17.5 (2005), pp. 621–+. ISSN: 0935-9648. DOI: 10.1002/adma.200401216. URL: %3CGo%20to%20ISI%3E://WOS:000227756600028.

[108] R. W. Zehner et al. “Tuning the work function of gold with self-assembled monolayers derived from X-[C6H4-C C-](n)C6H4-SH (n = 0, 1, 2; X = H, F, CH3, CF3, and OCH3)”. In: *Langmuir* 15.4 (1999), pp. 1121–1127. ISSN: 0743-7463. DOI: DOI10.1021/la981114f. URL: %3CGo%20to%20ISI%3E://WOS:000078682400036.

[109] C. D. Zangmeister et al. “Energy-level alignment and work function shifts for thiol-bound monolayers of conjugated molecules self-assembled on Ag, Cu, Au, and Pt”. In: *Chemical Physics Letters* 442.4-6 (2007), pp. 390–393. ISSN: 0009-2614. DOI: 10.1016/j.cplett.2007.06.012. URL: %3CGo%20to%20ISI%3E://WOS:000248382300042.

[110] X. Zhang et al. “Two-dimensional MoS2-enabled flexible rectenna for Wi-Fi-band wireless energy harvesting”. In: *Nature* 566.7744 (2019), pp. 368–+. ISSN: 0028-0836. DOI: 10.1038/s41586-019-0892-1. URL: %3CGo%20to%20ISI%3E://WOS:000459119200044.

[111] A. B. Kaul. “Two-dimensional layered materials: Structure, properties, and prospects for device applications”. In: *Journal of Materials Research* 29.3 (2014), pp. 348–361. ISSN: 0884-2914. DOI: 10.1557/jmr.2014.6. URL: %3CGo%20to%20ISI%3E://WOS:000331962700005.

[112] G. Fiori et al. “Electronics based on two-dimensional materials”. In: *Nature Nanotechnology* 9.10 (2014), pp. 768–779. ISSN: 1748-3387. DOI: 10.1038/Nnano.2014.207. URL: %3CGo%20to%20ISI%3E://WOS:000343617200017.

[113] R. Peng et al. “In-Plane Heterojunctions Enable Multiphasic Two-Dimensional (2D) MoS2 Nanosheets As Efficient Photocatalysts for Hydrogen Evolution from Water Reduction”. In: *Acs Catalysis* 6.10 (2016), pp. 6723–6729. ISSN: 2155-5435. URL: %3CGo%20to%20ISI%3E://WOS:000385057900051.

[114] F. Purcell-Milton et al. “Induction of Chirality in Two-Dimensional Nanomaterials: Chiral 2D MoS2 Nanostructures”. In: *Acs Nano* 12.2 (2018), pp. 954–964. ISSN: 1936-0851. URL: %3CGo%20to%20ISI%3E://WOS:000426615600006.

[115] L. L. Yu et al. “Graphene/MoS2 Hybrid Technology for Large-Scale Two-Dimensional Electronics”. In: *Nano Letters* 14.6 (2014), pp. 3055–3063. ISSN: 1530-6984. URL: %3CGo%20to%20ISI%3E://WOS:000337337100014.

[116] Y. C. Wang et al. “Electrochemical Control of Photoluminescence in Two-Dimensional MoS2 Nanoflakes”. In: *Acs Nano* 7.11 (2013), pp. 10083–10093. ISSN: 1936-0851. URL: %3CGo%20to%20ISI%3E://WOS:000327752200056.

[117] C. Y. Yim et al. “Investigation of the optical properties of MoS2 thin films using spectroscopic ellipsometry”. In: *Applied Physics Letters* 104.10 (2014). ISSN: 0003-6951. DOI: Artn10311410.1063/1.4868108. URL: %3CGo%20to%20ISI%3E://WOS:000333082800071.

[118] A. Molina-Sanchez, K. Hummer, and L. Wirtz. “Vibrational and optical properties of MoS2: From monolayer to bulk”. In: *Surface Science Reports* 70.4 (2015), pp. 554–586. ISSN: 0167-5729. DOI: 10.1016/j.surfrep.2015.10.001. URL: %3CGo%20to%20ISI%3E://WOS:000366949500002.

[119] J. Klein et al. “Impact of substrate induced band tail states on the electronic and optical properties of MoS2”. In: *Applied Physics Letters* 115.26 (2019).

ISSN: 0003-6951. DOI: Artn26160310.1063/1.5131270. URL: %3CGo%20to%20ISI%3E://WOS:000505613600019.

[120] N. Scheuschner et al. "Photoluminescence of freestanding single- and few-layer MoS2". In: *Physical Review B* 89.12 (2014). ISSN: 2469-9950. DOI: ARTN12540610.1103/PhysRevB.89.125406. URL: %3CGo%20to%20ISI%3E://WOS:000332456000006.

[121] M. Buscema et al. "The effect of the substrate on the Raman and photoluminescence emission of single-layer MoS2". In: *Nano Research* 7.4 (2014), pp. 561–571. ISSN: 1998-0124. DOI: 10.1007/s12274-014-0424-0. URL: %3CGo%20to%20ISI%3E://WOS:000339891100013.

[122] G. Plechinger et al. "Raman spectroscopy of the interlayer shear mode in few-layer MoS2 flakes". In: *Applied Physics Letters* 101.10 (2012). ISSN: 0003-6951. DOI: Artn10190610.1063/1.4751266. URL: %3CGo%20to%20ISI%3E://WOS:000309072800019.

[123] F. Bozheyev, D. Valiev, and R. Nemkayeva. "Pulsed cathodoluminescence and Raman spectra of MoS2 nanocrystals at different excitation electron energy densities and laser wavelengths". In: *Journal of Luminescence* 188 (2017), pp. 529–532. ISSN: 0022-2313. DOI: 10.1016/j.jlumin.2017.05.001. URL: %3CGo%20to%20ISI%3E://WOS:000404308400078.

[124] P. Zolotavin, C. Evans, and D. Natelson. "Photothermoelectric Effects and Large Photovoltages in Plasmonic Au Nanowires with Nanogaps". In: *Journal of Physical Chemistry Letters* 8.8 (2017), pp. 1739–1744. ISSN: 1948-7185. URL: %3CGo%20to%20ISI%3E://WOS:000400042200006.

[125] Michele Buscema et al. "Large and Tunable Photothermoelectric Effect in Single-Layer MoS2". In: *Nano letters* 13 (Jan. 2013). DOI: 10.1021/nl303321g.